POLITECNICO DI TORINO

Department of Energy Engineering

Master of Science in Energy and Nuclear Engineering

Master Thesis

Thermofluid-dynamics in pool heat exchangers

Supervisor:

Prof. Cristina BERTANI

Co-supervisors:

Dr. Andrea BERSANO

Dr. Nicolò FALCONE

Author:

Francesco PETRALLA

A.Y. 2018/19

CONTENTS

Contents 2
1. State of art 11
1.1 Natural circulation and passive safety systems 11
1.1.1 Passive Residual Heat Removal (PRHR) system example: AP1000 11
1.1.2 Isolation Condensers System (ICS) example: AHWR 13
1.2 Recent studies 14
1.2.1 Experimental studies 15
1.2.2 Numerical simulations 34
1.3 Conclusions on the state of art 71
2. Heat exchange 75
2.1 Pool boiling 75
2.1.1 The boiling curve (imposed heat flux) 75
2.1.2 Pool boiling correlation 79
2.1.3 Parametric effects on pool boiling 83
2.2 Condensation 84
2.2.1 Laminar film condensation on vertical surface 84
2.2.2 Turbulent film condensation 87
2.2.3 Phenomena affecting condensation 88
3. Preliminary analysis of the system 89
3.1 System description 89
3.2 Heat transfer in the pool 91
3.2.1 Model's description and correlation 91
3.3 Script's description 94
3.3.1 Inner wall temperature 94
3.3.2 Outer wall temperature 94
3.3.3 Water properties and dimensionless parameter 94

3.3.4 Heat transfer coefficient 95
3.3.5 Average power and average heat flux 96
3.3.6 Void fraction..... **Errore. Il segnalibro non è definito.**
3.3.7 Saturation time 97
3.4 Script's results 99
3.4.1 Outer wall temperature 99
3.4.2 Dimensionless parameters and heat transfer coefficient 104
3.4.3 Heat transfer coefficient 108
3.4.4 Natural convection heat transfer validation..... 110
3.4.5 Average power and average heat flux 113
3.4.6 Void fraction..... **Errore. Il segnalibro non è definito.**
3.4.7 Saturation time 116
4. Conclusions 120
5. References 122

List of figure

FIG. 1.1. SCHEMATIC REPRESENTATION OF AP1000 PRHR SYSTEM. (GE, TIAN, QIU, & SU, 2018) 12

FIG. 1.2. TOP VIEW OF A AP1000 IRWST (LU, ET AL., 2016) 13

FIG. 1.3. SCHEMATIC VIEW OF ICS AND GDWP OF AHWR (VERMA, NAYAK, VIKAS, & VASE, 2013)... 14

FIG. 1.4. DISPLACEMENT OF SOME OF THE CAPTURING WINDOWS (LU, ET AL., 2016). 16

FIG. 1.5. THERMOCOUPLES LOCATION INSIDE THE EXPERIMENTAL IRWST AND WITHIN THE PRHR HX BUNDLE (LU, ET AL., 2016). 16

FIG. 1.6. TEMPERATURE EVOLUTION RESPECT TO TIME ALONG (A) LINE 3 AND (B) LINE 5. (C) TEMPERATURE PROFILE ALONG LINE 3 FOR DIFFERENT TIME STEPS. (LU, ET AL., 2016). 17

FIG. 1.7. (A) EXPERIMENTAL TEST FACILITY (B) INTERNAL STRUCTURE TEST FACILITY ILLUSTRATION (TIAN, CHEN, WANG, CUI, & CHENG, 2018). 19

FIG. 1.8. HEAT TRANSFER COEFFICIENT'S EVOLUTION RESPECT TO TIME (T_{IN}=160 °C), FOR DIFFERENT VALUES OF H/D RATIO (TIAN, CHEN, WANG, CUI, & CHENG, 2018) 20

FIG. 1.9. EVOLUTION RESPECT TO TIME OF: BULK LIQUID TEMPERATURE, OUTER SURFACE TEMPERATURE AND HEAT TRANSFER COEFFICIENT AT DIFFERENT HEIGHT: (A) TOP REGION H/D=72.5 (B) BOTTOM REGION H/D=2.5 (TIAN, CHEN, WANG, CUI, & CHENG, 2018). 22

FIG. 1.10. POOL TEMPERATURE EVOLUTION ALONG LINE 2 RESPECT TO TIME AT DIFFERENT HEIGHT AND FOR DIFFERENT CONFIGURATION: UNCONFINED (BLACK LINES) AND CONFINED SPACE (RED LINES). (TIAN, CHEN, WANG, CUI, & CHENG, 2018). 23

FIG. 1.11. $H_{CONFINED}/H_{UN\text{-}CONFINED}$ VARIATION RESPECT TO HEIGHT-DIAMETER RATIO FOR DIFFERENT PRIMARY FLUID TEMPERATURES. (TIAN, CHEN, WANG, CUI, & CHENG, 2018)). 24

FIG. 1.12. SKETCH OF THE EXPERIMENTAL APPARATUS (GANGULI, SATHE, PANDIT, JOSHI, & VIJAYAN, 2010). 25

FIG. 1.13. SKETCH OF THE TEST FACILITY (TAO, GU, XIONG, JIANG, & XIE, 2018). 27

FIG. 1.14. BUNDLE SECTION AND THERMOCOUPLES POSITION (TAO, GU, XIONG, JIANG, & XIE, 2018). 29

FIG. 1.15. COMPARISON OF PRIMARY AND SECONDARY FLUID TEMPERATURE AND OUTER WALL TEMPERATURE PROFILES FROM EXPERIMENTS AND NUMERICAL SIMULATIONS. (TAO, GU, XIONG, JIANG, & XIE, 2018). 30

FIG. 1.16. NORMALIZED LOCAL HEAT FLUX PROFILE (TAO, GU, XIONG, JIANG, & XIE, 2018). 31

FIG. 1.17. DISTRIBUTION OF THE HEAT TRANSFER COEFFICIENT ALONG THE TUBE (TAO, GU, XIONG, JIANG, & XIE, 2018). 32

FIG. 1.18. WATER TEMPERATURE DISTRIBUTION INSIDE THE IRWST AFTER 2000 S (GE, TIAN, QIU, & SU, 2018)..... 34

FIG. 1.19.THERMAL STRATIFICATION BUILD UP IN: (A) IRWST REGIONS NEAR THE PRHR HX, (B) IRWST BULK REGION (GE, TIAN, QIU, & SU, 2018). 35

FIG. 1.20. LOCAL HEAT FLUX PROFILE (GE, TIAN, QIU, & SU, 2018)..... 36

FIG. 1.21. HEAT TRANSFER COEFFICIENT ALONG THE HEAT TRANSFER TUBES (GE, TIAN, QIU, & SU, 2018)..... 37

FIG. 1.22. TIME DEPENDENT TEMPERATURE EVOLUTION AT DIFFERENT HEIGHT OF THE POOL WITHOUT SHROUDS (VERMA, NAYAK, VIKAS, & VASE, 2013). 38

FIG. 1.23. ONE SECTOR OF GDWP WITH A CONCEPT OF SEVEN SHROUDS. (A) TOP VIEW. (B) CROSS SECTION (VERMA, NAYAK, VIKAS, & VASE, 2013). 39

FIG. 1.24. TEMPERATURE AT THE ISOLATION CONDENSER INLET AND OUTLET SECTIONS FOR (A) FIVE SHROUDS AND (B) SEVEN SHROUDS CONFIGURATION (VERMA, NAYAK, VIKAS, & VASE, 2013)..... 40

FIG. 1.25. MASS FLOWRATE AT THE INLET AND OUTLET OF THE ISOLATION CONDENSER'S SECTION AND IN THE OUTERMOST SHROUD FOR (A)FIVE SHROUDS AND (B) SEVEN SHROUDS CONFIGURATION (VERMA, NAYAK, VIKAS, & VASE, 2013).. 40

FIG. 1.26. TIME DEPENDENT BEHAVIOR OF TEMPERATURE AT THE ISOLATION CONDENSER'S SECTION FOR THREE SHROUDS CONFIGURATION (VERMA, NAYAK, VIKAS, & VASE, 2013)..... 41

FIG. 1.27. COMPARISON OF AVERAGE TEMPERATURE OF LAST DOWNWARD FLOW SHROUD (VERMA, NAYAK, VIKAS, & VASE, 2013)..... 42

FIG. 1.28. MASS FLOW RATE FOR THREE SHROUDS CONFIGURATION (VERMA, NAYAK, VIKAS, & VASE, 2013). 43

FIG. 1.29. SKETCH OF SINGLE-SHROUD CONFIGURATION. R IS THE SHROUD WALL'S HEIGHT AND H IS THE WATER LEVEL. (KUMAR (B), GROVER, VIJAYAN, & KANNAN, 2017)..... 44

FIG. 1.30. TIME DEPENDENT TEMPERATURE AT THE OUTLET SECTION OF THE IC (A) FOR 10 DAYS AND (B) FOR FIRST 6.5 WITH FIXED R CONFIGURATION EQUAL TO R1 AND DIFFERENT SS CONFIGURATIONS; (C) FOR 10 DAYS AND (D) FOR FIRST 6.5 FOR FIXED SS CONFIGURATION EQUAL TO SS4 AND DIFFERENT R CONFIGURATIONS (KUMAR (B), GROVER, VIJAYAN, & KANNAN, 2017). 45

FIG. 1.31. SKETCH OF SINGLE-SHROUD CONFIGURATION. L IS THE SHROUD'S HEIGHT AND H IS THE WATER LEVEL. (KUMAR (B), GROVER, VIJAYAN, & KANNAN, 2017). 46

FIG. 1.32. TIME DEPENDENT TEMPERATURE AT THE OUTLET SECTION OF THE IC FOR DIFFERENT FLOW AREA VALUES FOR FIXED VALUES OF WATER LEVEL-TO-HEIGHT RATIO: (A)L1, (B)L2, (C)L3, (D)L4 AND (E)L5 FOR THREE SHROUDS CONFIGURATION. (KUMAR (B), GROVER, VIJAYAN, & KANNAN, 2017) 48

FIG. 1.33. POOL TEMPERATURE VARIATION AT THE IC SECTION FOR DIFFERENT THERMAL CONDUCTIVITIES ASSUMING L3,TS3 THREE-SHROUDS CONFIGURATION(KUMAR (B), GROVER, VIJAYAN, & KANNAN, 2017). 49

FIG. 1.34. EFFECT OF LEAKAGE WITH 4 LEAKAGE POINT EQUALLY DISTRIBUTED THROUGH THE MIDDLE SHROUD ON TEMPERATURE AT IC OUTLET ON POOL SIDE FOR TS3L3 CONFIGURATION (KUMAR, GROVER, VIJAYAN, & KANNAN, 2017). 50

FIG. 1.35. (A) DOMAIN OF THE VERTICAL SECTION OF THE TUBE, (B) THE COMPUTATIONAL REGION (TIAN, ZHANG, WANG, CUI, & CHENG, 2017). 54

FIG. 1.36. NUMERICAL MODEL (TIAN, ZHANG, WANG, CUI, & CHENG, 2017) 55

FIG. 1.37. HEAT FLUX AS A FUNCTION OF THE EXCESS OF TEMPERATURE FOR ALL THE CONSIDERED CORRELATION (TIAN, ZHANG, WANG, CUI, & CHENG, 2017) 57

FIG. 1.38. PHYSICAL FIELDS AT (A) LOWER PART, (B) MIDDLE PART, (C) UPPER PART OF THE VERTICAL TUBE IN THE LONGITUDINAL DIRECTION (TIAN, ZHANG, WANG, CUI, & CHENG, 2017) 59

FIG. 1.39. AXIAL, INNER WALL AND OUTER WALL TEMPERATURE DISTRIBUTION IN THE VERTICAL SECTION OF THE TUBE (TIAN, ZHANG, WANG, CUI, & CHENG, 2017). 60

FIG. 1.40. VOID FRACTION AND VELOCITY FIELD AT (A) Z_1 AND (B) Z_2.(TIAN, ZHANG, WANG, CUI, & CHENG, 2017). 61

FIG. 1.41. TIME DEPENDENT HEAT FLUX FOR DIFFERENT SECTIONS OF THE TUBE (TIAN, ZHANG, WANG, CUI, & CHENG, 2017). 62

FIG. 1.42 HEAT TRANSFER TUBE DISCRETIZATION (TAO, GU, XIONG, JIANG, & XIE, 2018). 63

FIG. 1.43. FLOWCHART OF THE SOLUTION ALGORITHM. EQ(9) REFERS TO ROHSENOW CORRELATION, EQ(14) REFERS TO BERGLES-ROHSENOW CORRELATION. (TAO, GU, XIONG, JIANG, & XIE, 2018). 64

FIG. 1.44. ENERGY VARIATION RESPECT TO TIME. . CFD — (1) E_F, (2) E_Q , (3) E_E AND (4) $E_{TOT.}$ EXPERIMENTAL (TRIANGLE) E_F, (RHOMBUS) E_Q, (SQUARE) E_E AND (CIRCLE) E_{TOT}. (ARIJIT, ET AL., 2010) 70

FIG. 2.1. SCHEMATIC OF THE NUKIYAMA EXPERIMENTAL SYSTEM (POWER CONTROL HEATING CONFIGURATION) (INCROPERA, DEWITT, BERGMAN, & LAVINE, 2011). 76

FIG. 2.2. BOILING CURVE FOR POOL BOILING OF WATER AT ATMOSPHERIC PRESSURE (THOMPSON, 2013) 77

FIG. 2.3. POOL BOILING REGIMES: A SCHEMATIC REPRESENTATION(COLLIER & THOME, 1994) 79

FIG. 2.4. SCHEMATIC REPRESENTATION OF CONDENSATION MODES ON A VERTICAL SURFACE: (A) FILM-WISE, (B)DROP-WISE (KHAN, TAHIR, BALOCH, & KOÇ, 2019) 84

FIG. 2.5. FORCE BALANCE IN THE LIQUID FILM CONTROL VOLUME. LIQUID IS MOVING DOWNWARD (WHALLEY, 1987) 85

FIG. 3.1. TOP VIEW AND SECTION OF THE SYSTEM (TANK AND TUBE CONFIGURATION) 89

FIG. 3.2 TANK FRONT VIEW. 90

FIG. 3.3. EQUIVALENT THERMAL CIRCUIT (IMPOSED TEMPERATURE CONFIGURATION) 92

FIG. 3.4.ALGORITHM ADOPTED TO EVALUATE THE HEAT TRANSFER CHARACTERISTICS DURING THE FREE CONVECTION STAGE 98

FIG. 3.5. ALGORITHM ADOPTED TO EVALUATE THE HEAT TRANSFER CHARACTERISTICS DURING THE SATURATED POOL BOILING STAGE 99

FIG. 3.6. OUTER WALL TEMPERATURE AS A FUNCTION OF THE IMPOSED POOL TEMPERATURE ... 100

FIG. 3.7. TOTAL THERMAL RESISTANCE VARIATION AS A FUNCTION OF THE AVERAGE HEAT FLUX 101

FIG. 3.8. OUTER WALL TEMPERATURE AS A FUNCTION OF THE IMPOSED HEAT FLUX. 102

FIG. 3.9. DIFFERENCE OF TEMPERATURE THOUGH THE PIPE WALL AS A FUNCTION OF THE POOL TEMPERATURE 103

FIG. 3.10. DIFFERENCE OF TEMPERATURE THOUGH THE PIPE WALL AS A FUNCTION OF THE EXCHANGED AVERAGE HEAT FLUX 104

FIG. 3.11. GLOBAL GRASHOF AND PRANDTL NUMBER AS FUNCTIONS OF POOL TEMPERATURE ... 105

FIG. 3.12. GLOBAL GRASHOF AND PRANDTL NUMBER AS FUNCTIONS OF THE HEAT FLUX 106

FIG. 3.13. GLOBAL NUSSELT AND GLOBAL RAYLEIGH NUMBER AS FUNCTIONS OF THE EXCHANGED HEAT FLUX 107

FIG. 3.14. GLOBAL NUSSELT AND GLOBAL RAYLEIGH NUMBER AS FUNCTIONS OF THE POOL TEMPERATURE 108

FIG. 3.15. AVERAGE HEAT TRANSFER COEFFICIENT AT DIFFERENT AVERAGE HEAT FLUXES. 109

FIG. 3.16. AVERAGE HEAT FLUXES AT DIFFERENT POOL TEMPERATURES 110

FIG. 3.17. HEAT TRANSFER COEFFICIENT MAP 111

FIG. 3.18. HEAT TRANSFER COEFFICIENT COMPARISON BETWEEN THE VALUES OBTAINED BY THE CORRELATION (3.15) AND THE ONES OBTAINED BY THE HEAT TRANSFER COEFFICIENT DEFINITION (3.28) AS FUNCTIONS OF THE AVERAGE HEAT FLUX 112

FIG. 3.19. HEAT TRANSFER COEFFICIENT COMPARISON BETWEEN THE VALUES OBTAINED BY THE CORRELATIONS (EQ.3.15) AND THE ONES OBTAINED BY THE HEAT TRANSFER COEFFICIENT (3.28) DEFINITION AS FUNCTIONS OF THE POOL TEMPERATURE 113

FIG. 3.20. AVERAGE THERMAL POWER AS A FUNCTION OF POOL TEMPERATURE 114

FIG. 3.21. AVERAGE HEAT FLUX AS A FUNCTION OF POOL TEMPERATURE 115

FIG. 3.22. ESTIMATION OF THE HEAT FLUX LOOKING AT THE OUTLET TITLE 116

FIG. 3.23. POWER EVOLUTION RESPECT TO TIME. IMPOSED TEMPERATURE CONFIGURATION. 117

FIG. 3.24. TEMPERATURE EVOLUTION RESPECT TO TIME. IMPOSED TEMPERATURE CONFIGURATION. 118

FIG. 3.25. TEMPERATURE EVOLUTION RESPECT TO TIME. IMPOSED HEAT FLUX CONFIGURATION. 119

List of tables

TABLE 1.1. GEOMETRICAL AND OPERATING PARAMETERS FOR PROTOTYPE (AP1000 PRHR HX) AND CONSIDERED SCALED SYSTEM. (LU, ET AL., 2016)..... 15

TABLE 1.2. PRIMARY LOOP OPERATING PARAMETERS (TAO, GU, XIONG, JIANG, & XIE, 2018). 27

TABLE 1.3. . WATER LEVEL-TO-HEIGHT RATIO FOR SINGLE SHROUD CONFIGURATION (KUMAR (B), GROVER, VIJAYAN, & KANNAN, 2017)..... 44

TABLE 1.4 WATER LEVEL-TO-HEIGHT RATIO FOR THREE-SHROUD CONFIGURATION (KUMAR (B), GROVER, VIJAYAN, & KANNAN, 2017)..... 46

TABLE 1.5. TIME REQUIRED TO REACH SATURATION CONDITIONS INSIDE THE POOL FOR DIFFERENT THREE-SHROUDS CONFIGURATIONS (KUMAR (B), GROVER, VIJAYAN, & KANNAN, 2017). 47

TABLE 1.6. BOUNDARY CONDITIONS (TIAN, ZHANG, WANG, CUI, & CHENG, 2017). 55

TABLE 1.7. NUMERICAL RESULTS COMPARED WITH CORLETTI ET AL. CORRELATION. (TIAN, ZHANG, WANG, CUI, & CHENG, 2017)..... 58

TABLE 1.8. ENERGY BALANCE IN THE GLASS TANK (GANGULI, SATHE, PANDIT, JOSHI, & VIJAYAN, 2010)..... 69

TABLE 2.1 VALUES OF $C_{S,F}$ AND N COEFFICIENTS FOR SOME COMBINATIONS OF FLUID-SURFACE'S MATERIAL (INCROPERA, DEWITT, BERGMAN, & LAVINE, 2011) 80

TABLE 3.1. MAIN OPERATING PARAMETERS..... 90

Introduction

Pool heat exchangers are a class of heat transfer devices where the heat source releases thermal power to a heat sink represented by a stagnant liquid in a relatively large containment: the pool. Pools are typically characterized by very high thermal capacity, for this reason they are filled by subcooled water. Depending on the characteristics of the heat source and on the pool thermodynamic conditions, different phenomena can be involved during the heat transfer process. Of course, different systems configurations (heat source and pool) are characterized by different heat transfer mechanism. For example, a pool heat exchanger can be obtained by using as heat source a steam mass flowrate released in a tank filled by subcooled water that directly condenses the vapor. In this case the heat transfer mechanism is direct condensation by which the latent heat of vaporization of the steam is released to the subcooled liquid, increasing its temperature. In general, the increase of pool temperature leads to natural circulation phenomena and thermal stratification (established by temperature and density gradients).

Pool heat exchangers are particularly interesting because, if saturation conditions can be reached in the heat sink, pool boiling phenomena may occur. Depending on thermofluid-dynamic conditions of the fluids involved in the process, different pool boiling regimes can be observed. For industrial application where high thermal power need to be released, pool heat exchangers represent a suitable solution, in particular if the established heat transfer mechanism is the nucleate pool boiling. Nucleate pool boiling is the most efficient heat transfer mechanism for heat exchangers immersed in a large pool of stagnant water. As a matter of fact, nucleate pool boiling allows to exchange very high thermal fluxes with relatively small difference of temperature between the source and the heat sink. Industrial pool boiling heat exchangers that take advantage of nucleate boiling are typically made by a heat exchanger (single tube or, more commonly, tube bundle) immersed in a very large pool filled by stagnant subcooled water at the atmospheric pressure.

Pool heat exchangers are also employed in order to remove the decay heat from the core of a nuclear reactor during normal operating conditions (e.g. Gen-IV reactors like Small Modular Reactor or Simplified BWR) and after a Station Blackout (SBO), when external power is not available (e.g. Gen-III+ reactors like AP600 or AP1000 or AHWR). In this case the decay heat is removed from the core by using typical industrial configuration of pool heat exchangers, in order to cool down primary fluid up to 72 hours with no outer intervention and assuring plant's safety.

During the last years, many studies were performed with the purpose of investigating in more detail phenomena that characterize pool heat exchangers typically adopted by Gen.-III+ nuclear fission plants. In particular, the most important phenomena under investigation were: thermal stratification, due to a non uniform temperature distribution inside the pool, and two-phase heat transfer mechanism, occurring when stratified secondary fluid reaches saturation conditions.

Analyzing some of the most important studies focused on the heat transfer mechanisms occurring in pool heat exchanger, one of the most important observed criticalities concerns the lack of experimental data available about pool heat exchangers, in particular during the two-phase heat transfer. For this reason the goal of this work is to characterize, from a thermofluid-dynamic point of view, a small pool heat exchanger system that will be further investigated through experimental measurements.

1.1 NATURAL CIRCULATION AND PASSIVE SAFETY SYSTEMS

Passive safety systems are employed to perform safety functions without the need for active power sources. In principle, any physical barrier against the release of fission product is a passive safety system. Very important is the passive removal of decay heat from the core. It can be accomplished by systems operating on natural circulations are an other example of passive safety systems, since they are capable to cool down the reactor's core without requiring any external power source or moving mechanical parts.

Large water pools, characterized by a huge heat capacity, are employed as heat sinks. Natural circulation systems, if they are properly designed, can cool down the core of a nuclear power plant in case of prolonged SBO with no intervention from operators up to 72 h. They are typically used by Gen. III+ reactors. At the moment, as regards thermal water reactors, there are mainly two different kind of systems adopted to passively remove the decay heat from the core: Passive Residual Heat Removal Heat Exchangers (PRHR HX) immerged in the In-containment Refueling Water Storage Tank (IRWST) and Isolation Condensers (ICs) immerged in the Gravity Driven Water Pool (GDWP), respectively employed in Advanced Passive pressurized water reactors (e.g. AP1000, AP600, CAP1400) and advanced reactors type such as European Pressurized Reactor (EPR) or the Indian Advanced Heavy Water Reactor (AHWR), which is a pressure tube type BWR.

The above-mentioned systems are designed to provide enough cooling to the core for a period of three days (grace period), assuring fuel integrity and avoiding structural damages.

1.1.1 *Passive Residual Heat Removal (PRHR) system example: AP1000*

The AP1000 is a Gen.-III+ fission nuclear reactor produced by Toshiba-Westinghouse Electric Company. Its safety systems are based on passive safety. A sketch of the system is reported in Fig. 1.1.

During a SBO, the Passive Core Cooling System (PCCS) guarantees the decay heat removal thanks to the PRHR HX and IWRST. The safety loop is isolated from the Reactor Cooling System (RCS), during normal operating conditions, by valves that are normally closed. When the PCCS is activated, the mixture of steam and water coming from the hot leg of the reactor vessel flows inside the PRHR HX. PRHR HX employed in the AP1000 is a C-shape tube bundle (689 tubes) heat exchanger. It is vertically immerged in the IWRST, which is placed above the reactor vessel. The IRWST (Fig. 1.2) is an irregular shape pool at atmospheric pressure, containing cold borated water, which is the heat sink. The pool is characterized by a big mass inventory. As a matter of fact it is

long about 36 m and the water level is 8 m. Primary fluid, flowing inside the PRHR HX, releases thermal power to the cold water inside the IWRST (secondary fluid). The lower horizontal section of the heat exchanger is connected to the outlet plenum of the Steam Generator (SG). The outlet plenum is connected to the cold leg of the RCS, which guarantees the recirculation of the primary coolant. The IRWST is also used as suppression pool for the release of steam produced in the core during some incidental scenarios (e.g. transients) through the Automatic Depressurization System (ADS). The pool is also employed during refueling operations.

The heat removal process inside the pool is characterized by a first stage dominated by natural circulation. After that, thermal stratification occurs and the second stage is characterized by pool boiling. Even though boiling phenomena occur in the IRWST, water level can be considered constant because of the presence of metal plates in the containment building that, exchanging heat power with the external environment, are capable to condensate the produced steam. In this way water returns in the IRWST as droplets.

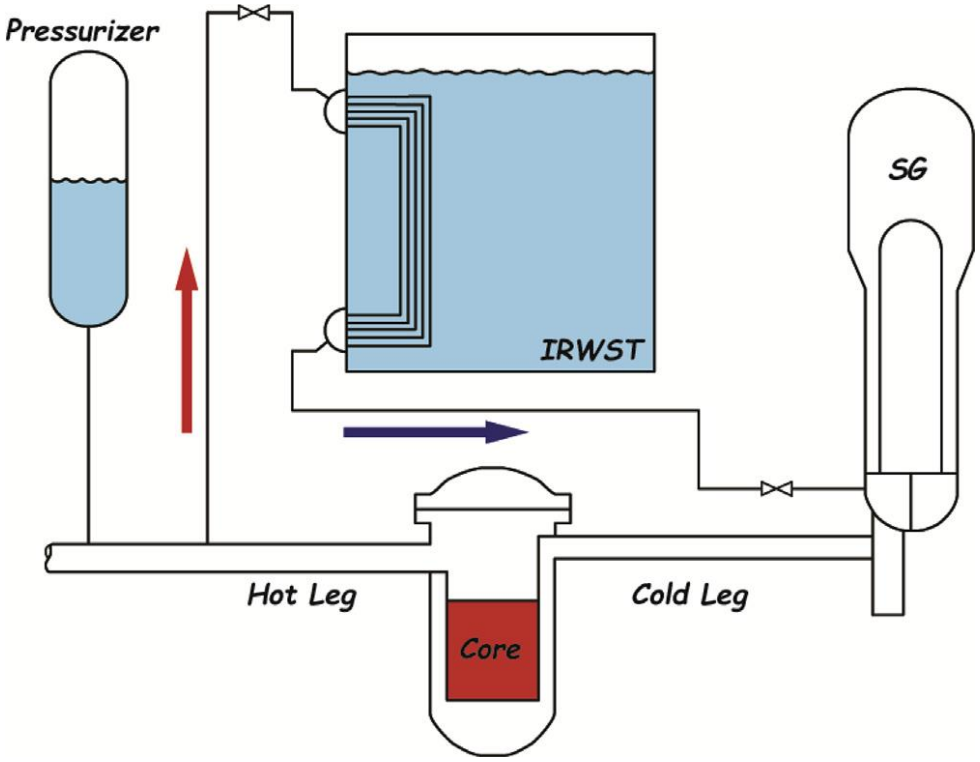

Fig. 1.1. Schematic representation of AP1000 PRHR system. (Ge, Tian, Qiu, & Su, 2018)

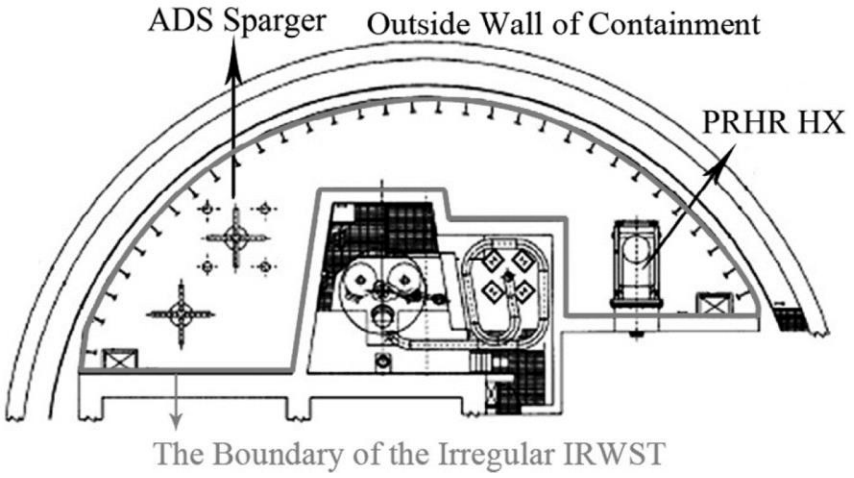

Fig. 1.2. Top view of a AP1000 IRWST (Lu, et al., 2016)

1.1.2 *Isolation Condensers System (ICS) example: AHWR*

The ICS includes a set of immersed condensers located in an elevated water pool, the GDWP, which holds a huge inventory (8000 m^3) of water kept on the top of the steam drums of the reactor. A sketch of the system is reported in Fig. 1.3.

IC's top header are directly connected to the steam line. Primary fluid passes through the tube bundle where it condenses thanks to the heat exchange with the heat sink. On the pool side, natural convection heat transfer mechanism is established. The GDWP is divided into eight interconnected compartments filled with water and one IC is submerged in each compartment of the pool. The condensed primary coolant flows inside the condensate return line and reaches the steam drums. The condensate return line is equipped with a set of active and passive vales. Their opening depends on the pressure on the steam drum. Typically, the operating pressure in the return line connecting the ICs and the steam drum is 70 bar. The passive valve starts to operate when the pressure in the line is 76.5 bar and it is fully open when the pressure reaches 79.5 bar. On the other hand, the active valve can be opened by an operator, but for safety reasons it opens automatically when the pressure is 80 bar, thanks to a high-pressure signal. In this way the recirculation of primary water is guaranteed.

A well-designed passive safety system provides cooling for a period of 3 days (grace period) in order to guarantee the safety of the plant and structures integrity.

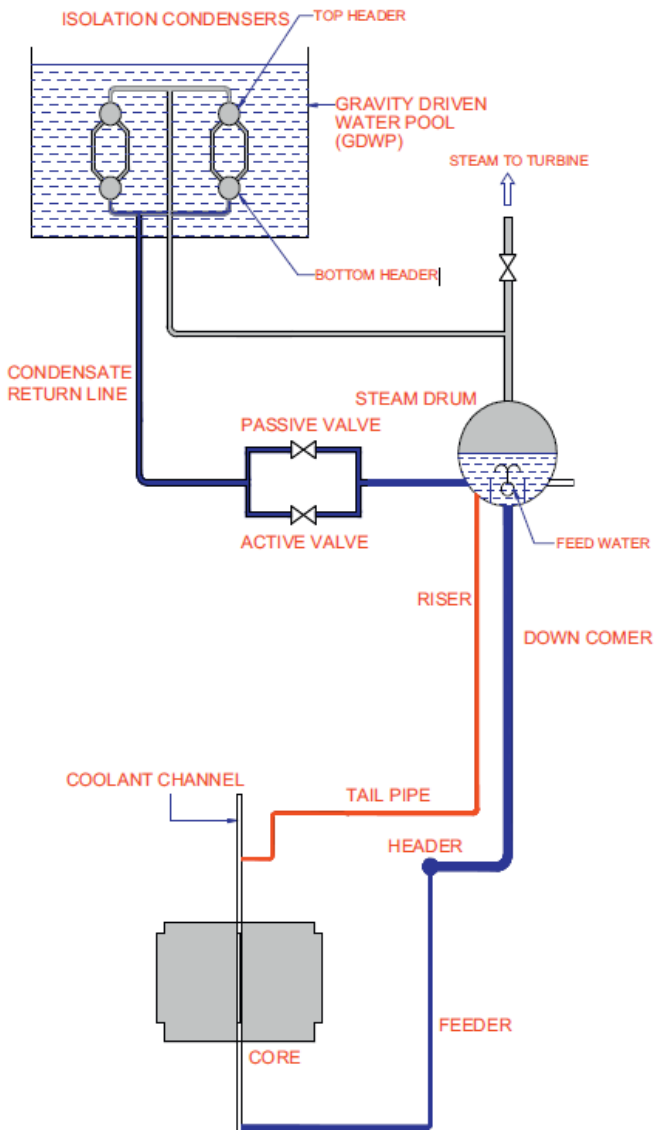

Fig. 1.3. Schematic view of ICs and GDWP of AHWR (Verma, Nayak, Vikas, & Vase, 2013).

1.2 RECENT STUDIES

In the recent years, a lot of studies are performed in the field of the heat removal by natural circulation trying to better understand the time behavior of the most important parameters involved during the process (e.g. heat transfer coefficient, heat flux, temperature and velocity fields). In order to collect and analyze experimental data, most of these studies are conducted on scaled facilities, due to the big size of above-mentioned systems. CFD and numerical simulations have also been performed, providing in most cases coherent results with the extrapolations made by scaled experiments. Empirical and numerical studies are reported respectively in sections 1.2.1 and 1.2.2, with particular attention to problems and phenomena emerged during the studies.

1.2.1 *Experimental studies*

In this section a focus on the experimental studies published in the last years is presented. Due to the big dimensions of the systems, the experimental investigations were performed on smaller test facilities.

For example, Lu et al. (2016) examined the heat exchange in a scaled system. The scaled PRHR HX is made by 12 C-shaped rods. Rods are symmetrically arranged and they are electrically heated. The IRWST measures 3.75 m in the lateral direction and it is 1.5 m wide and 2.5 m high. Water level inside the tank is equal to 2.2 m. Wall thickness equal to 8 mm of 304 stainless steel. The IRWST was insulated by 50 mm of aluminum silicate wool on the sidewalls. The PRHR HX is placed on one side of the IRWST. The power released by the heat exchanger is reduced to 176 kW. All the other key parameters are listed in Table 1.1, where a comparison with the original prototype is also given.

Table 1.1. Geometrical and operating parameters for prototype (AP1000 PRHR HX) and considered scaled system. (Lu, et al., 2016)

Items	**Prototype parameters**	**Scaled model parameters**	**Ratios**
Length of IRWST in lateral direction	About 36 m	3.75 m	1/9.6
Water level inside the IRWST	8 m (water level)	2.2 m	1/3.64
Initial water temperature	48.9 °C	48.9 °C	1/1
PRHR HX tubes number	689	12	1/57.4
Outside diameter of heat transfer tube	19 mm	19 mm	1/1
Pitch	38 mm	38 mm	1/1
Heat power	5.89×10^7 W	About 176 kW	1/334.7

For the measurements, more than 150 calibrated thermocouples (T-type with stainless steel sheathed) are used to evaluate temperatures in different regions such as bulk fluid region, regions within the tube bundle and on the outer surface of some tubes. Monitoring lines are shown in Fig. 1.6. Also PIV technique is used for qualitative evaluation of the fluid path during the thermal stratification process thanks to visualization windows (21 in total). Fig. 1.5 shows the disposition of the considered spots for the PIV analysis and a qualitative representation of the water streamlines due to natural convection inside the IRWST.

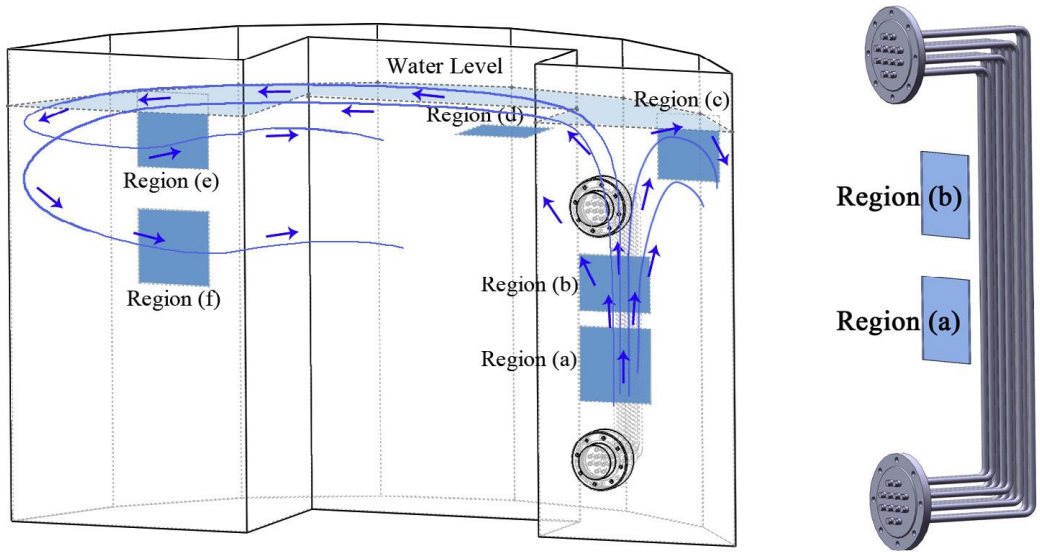

Fig. 1.4. Displacement of some of the capturing windows (Lu, et al., 2016).

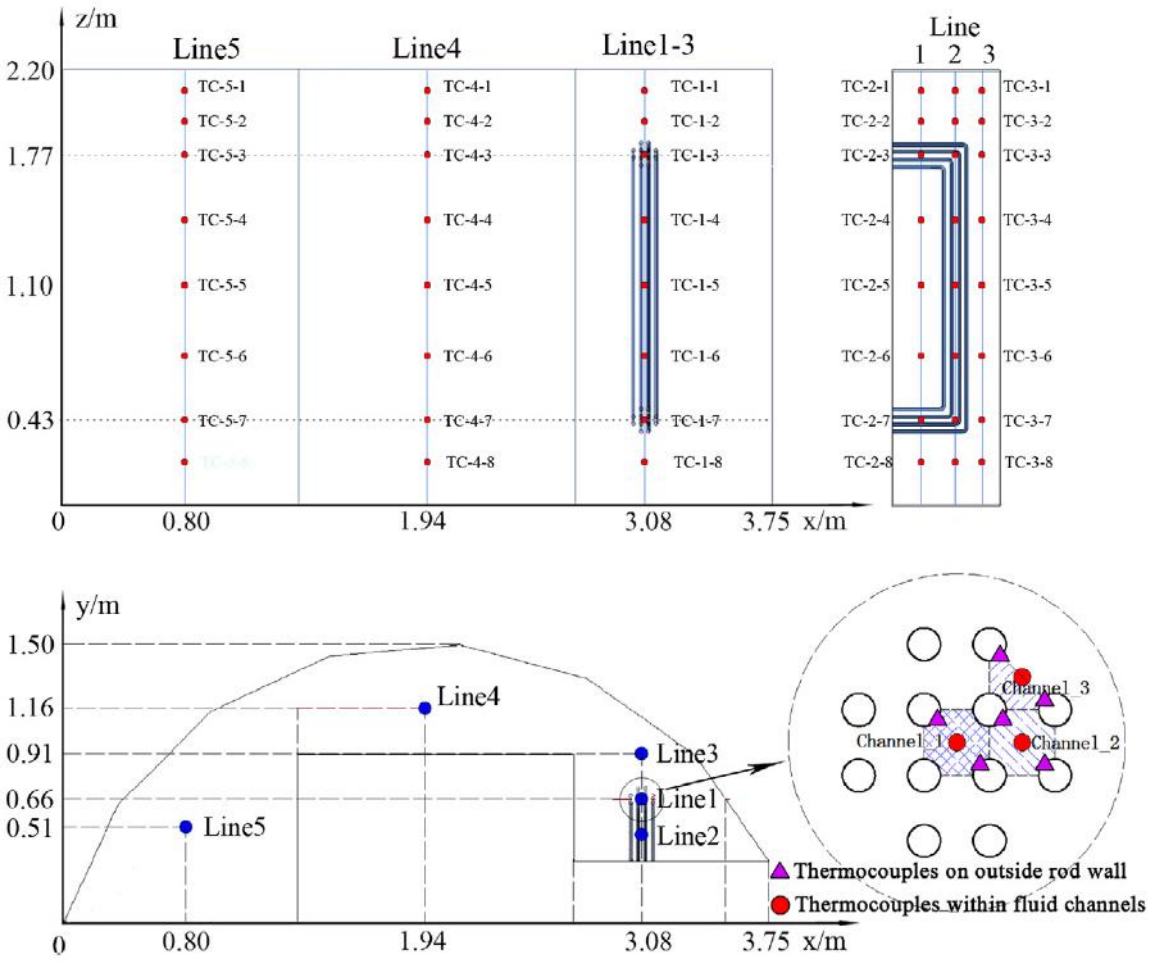

Fig. 1.5. Thermocouples location inside the experimental IRWST and within the PRHR HX bundle (Lu, et al., 2016).

The temperature evolution during the experimental procedure along line 3 (adjacent to the PRHR HX) and line 5 (far from the PRHR HX) is represented in Fig. 1.6 (a) and (b). Fig 1.6 (c) shows the thermal stratification along the line 3. Temperatures in Fig. 1.6 are normalized as follows (eq. 1.1):

$$T_{normalized} = \frac{T - T_0}{T_{max} - T_0} = \frac{T - 48.9\,°C}{100°C - 48.9°C} \qquad (eq.\,1.1)$$

The initial temperature of water (T_0), equal to 48.9 °C, is set as the origin point. Water saturation temperature (100 °C) is set as the maximum reference value. When the pool reaches the saturation temperature, the normalized temperature value is equal to 1. Fig 1.6 (a) and 1.7 (b) show that temperature increases with almost a constant rate for the most of the experiment.

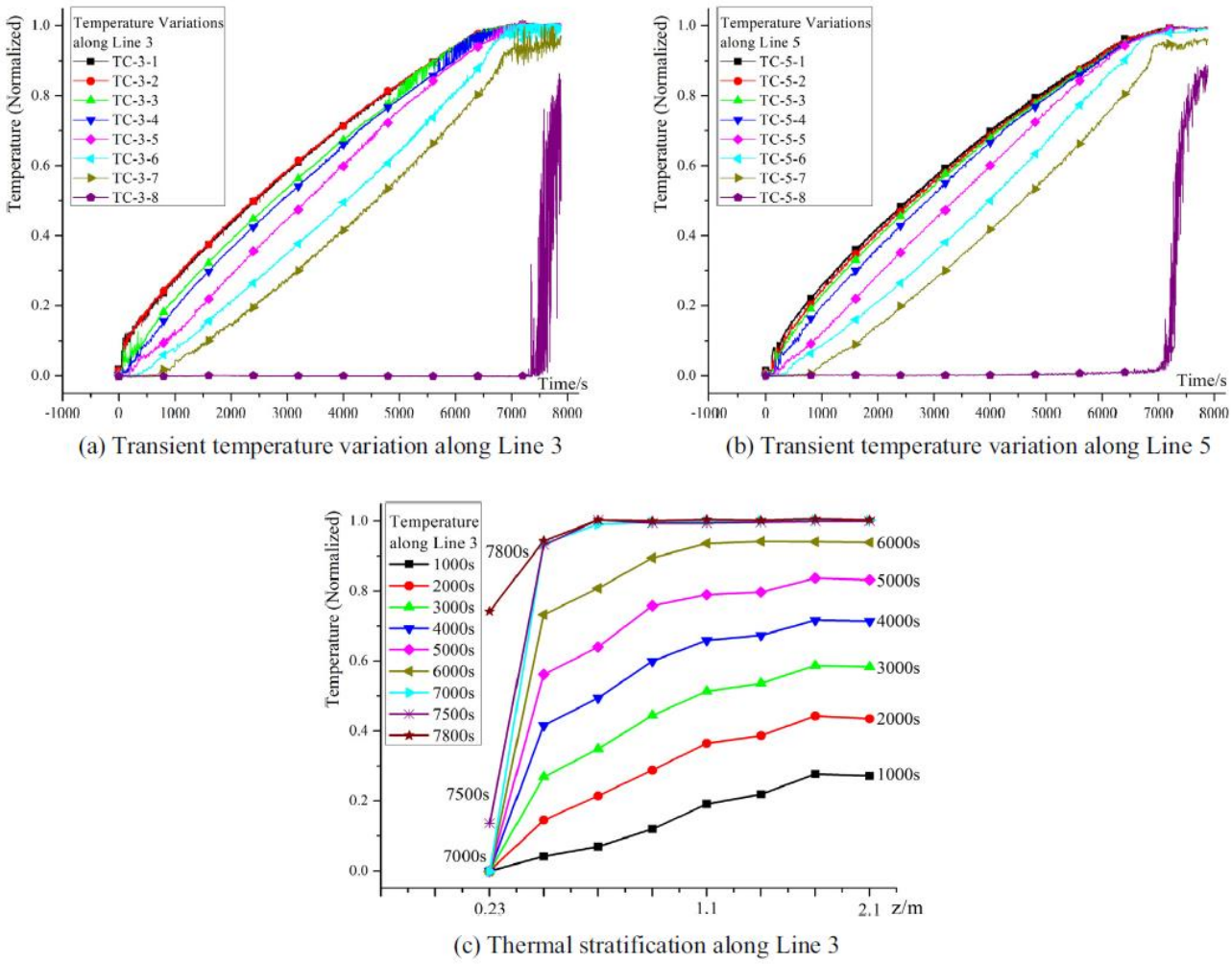

Fig. 1.6. Temperature evolution respect to time along (a) line 3 and (b) line 5. (c) Temperature profile along line 3 for different time steps. (Lu, et al., 2016).

It's easy to recognize thermal stratification since the lover thermocouple in each line (TC-3-8 and TC-5-8) shows a constant temperature equal to 48.9 °C for more than 6500 s, which suggests that the lower region of the pool is thermally inactive, since the water below the lower horizontal section of the heat exchanger does not contributes to the heat transfer process. The highest values of temperature are detected near the upper bend (TC-3-2) of the tube bundle. After about 7000 s, the temperature in the regions below the upper bend increases with remarkable fluctuations, due to intense mixing between cold and hot fluid. It suggests that a "thermal interface" is established. During the first stage of the heat transfer process, water is heated by the heat exchanger. Hotter and lighter fluid flows up thanks to the buoyancy force. On the other hand, in the lower regions, water is colder and heavier and it does not participate to the heat exchange. Thermal stratification is established and heat transfer, from the upper and hotter region to the lower one, occurs thanks to thermal conductivity between layers of fluid at different temperature. Progressively, the upper fluid reaches the saturation condition, being heated by the PRHR HX. Simultaneously, the "thermal interface" propagates to the lower layers until it reaches the bottom of the tank. When the "thermal interface" reaches the inactive region of the pool, intense mixing phenomena occur and thermal stratification is suppressed, since the pool reaches the saturation temperature.

Fig. 1.6 (c) shows the temperature gradient along line 3. The axis of abscissa shows the height of the pool, starting from the bottom. For each time step showed in Fig. 1.6 (c), pool temperature detected along line 3 is displayed. The first value is detected at z=0.23 m, which is the location of the lower thermocouple. Along this line, the fluid is heated up, passing through the bundle of the PRHR HX. Under the effect of the buoyancy force, the hot water reaches the pool surface. There, the hot fluid floats on the pool surface and moves in the radial direction, reaching the walls of the IRWST, as shown in Fig. 1.4. In this way, hotter fluid accumulates in the higher regions of the tank, the "thermal interface" builds up and thermal stratification becomes dominant inside the pool.

From this experimental work some consideration can be extrapolated: inside the pool, lifting forces generated by density and temperature gradients affect the velocity distribution. During this process, the position of "thermal interface" plays an important role as regards the instauration of thermal stratification. When the "thermal interface" reaches the bottom of the pool, considerable temperature fluctuations are detected because of the mixing phenomena between hot and cold water. Mixing suppresses thermal stratification and, as the heating process goes on, the temperature inside the pool reaches the saturation value.

Other experimental investigations are carried out on systems that aren't strictly employed in the nuclear field, but that show significant results in the topic of natural circulation and heat exchange in water pools.

Tian et al. (2018) studied the heat transfer mechanism of pool boiling on a vertical tube in different configurations: confined and unconfined space and with different heat fluxes. The experimental apparatus is shown in Fig. 1.7.

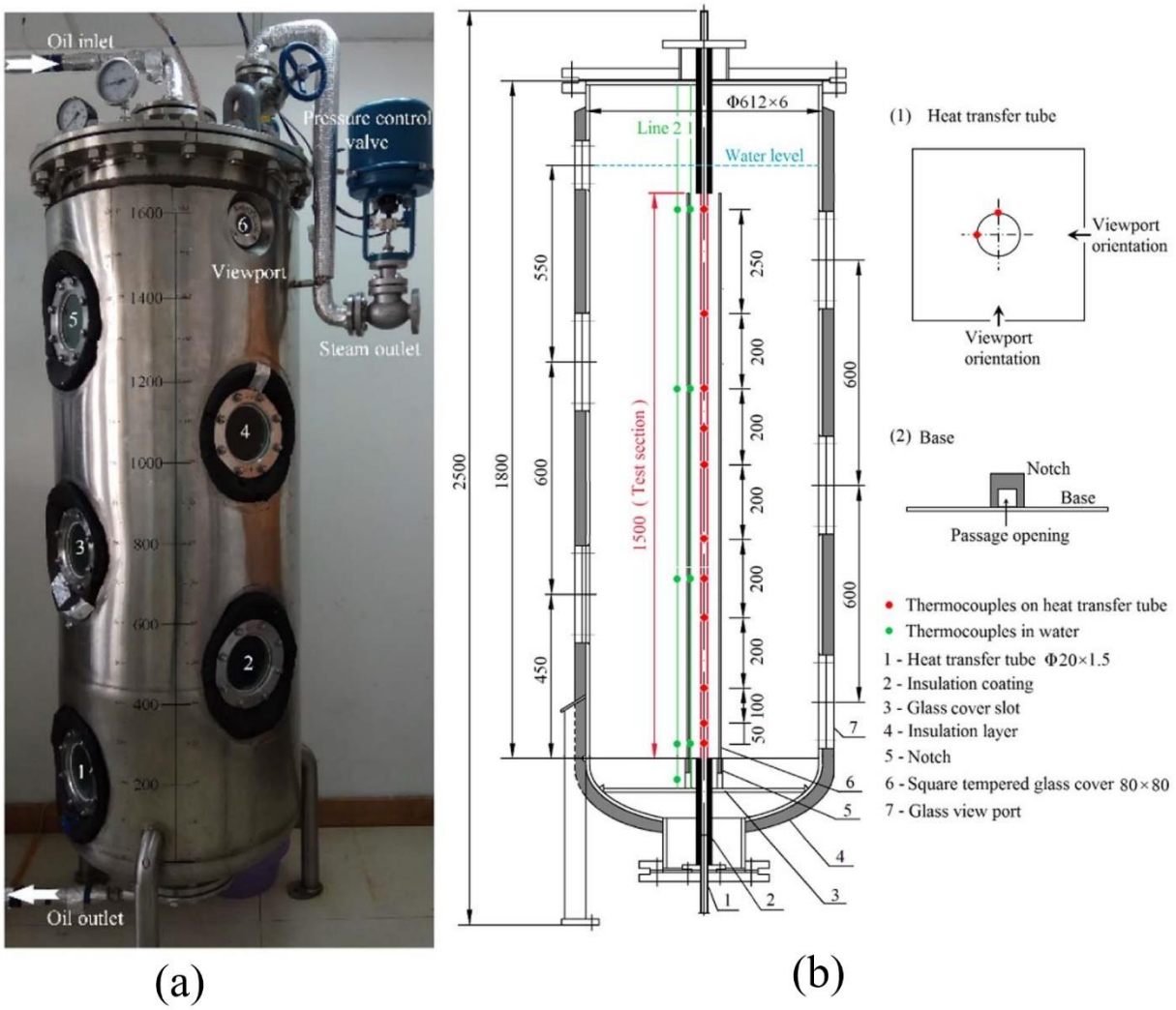

Fig. 1.7. (a) Experimental test facility (b) Internal structure test facility illustration (Tian, Chen, Wang, Cui, & Cheng, 2018).

The experimental apparatus is made by a water tank, a vertical tube in which a heat transfer fluid (oil) flows, a copper condensing coil placed in the upper region to reduce the water evaporation inside the pool and a pressure control valve capable to regulate the pressure inside the tank. The stainless steel tank's diameter is equal to 612 mm with a thickness of 6 mm. It is insulated by 50 mm of Aluminum silicate wool and 6 ports are placed on the lateral surface of the tank to observe the water level. The vertical tube is characterized by: outer diameter of 20 mm and length of 1500 mm (H/D=75) with 22 thermocouples distributed as shown in Fig. 1.7 (b). Near the tube, pool temperature is measured using two monitoring lines (green lines in Fig. 1.7 (b)), respectively

placed at 40 mm and 80 mm from the axis. The tank is filled by deionized water which is heated by oil flowing inside the tube.

The experimental procedure is divided in two steps: during the first one the pool boiling phenomena in a confined space around the tube is observed, then the confinement is removed and the heat exchange in the unconfined space is studied and results are compared. The confinement is made by a squared glass shell with cross section 80 mm x 80 mm.

The process of heat transfer in the confined space is characterized by complex mass and energy transport phenomena. The heat transfer mechanisms involved during the experiments are basically three: natural convection, subcooled and saturated boiling. This can be easily seen in Fig. 1.8. During the natural convection, the heat transfer coefficient grows as the experiment goes on. Four different height from the bottom are taken in to account: 1450 mm (H/D=72.5), 1000 mm (H/D=50), 500 mm (H/D=25), 50 mm (H/D=2.5).

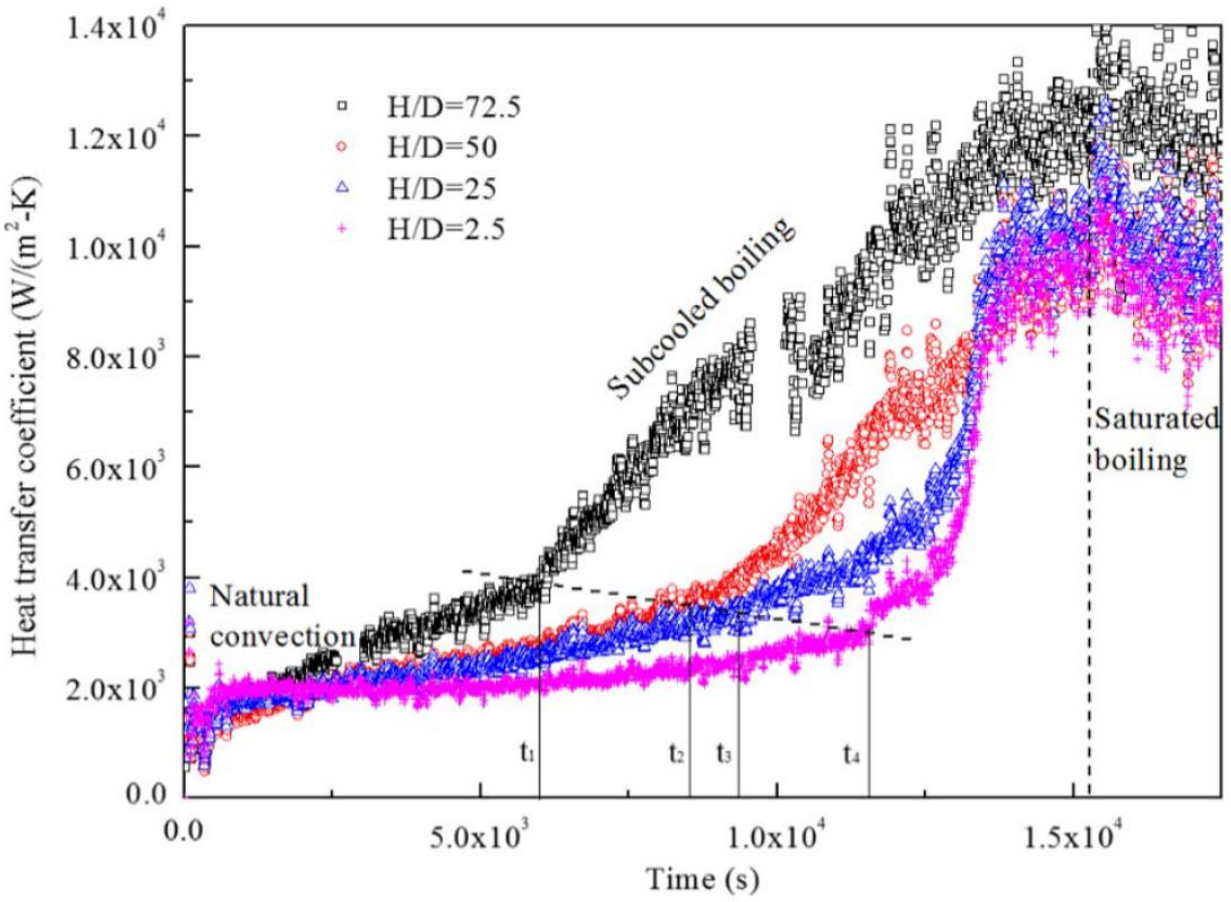

Fig. 1.8. Heat transfer coefficient's evolution respect to time (T_{in}=160 °C), for different values of H/D ratio (Tian, Chen, Wang, Cui, & Cheng, 2018)

Approaching to the bottom of the tank (H/D=2.5), natural convection lasts longer because of the thermal stratification. As the time goes on, the contribution of the boiling becomes dominant in the heat removal process. When the upper part of the tube outer surface approaches saturation boiling, the heat transfer coefficient suddenly increases along the pipe and both the upper and the lower region of the pool reach saturation conditions approximately at the same time. During the saturated boiling the average value of the heat transfer coefficient is almost constant, but its profile is characterized by large fluctuations (see Fig. 1.8).

The time behavior of tube outer surface temperature and bulk temperature at different height (H/D=72.5 and H/D=2.5) are shown in Fig. 1.9. When subcooled boiling is reached, an outer wall temperature decrease is detected (point A and B in Fig. 1.9) because of the increasing value of the of the local heat transfer coefficient. Local heat transfer coefficient variation is due to the bubble nucleation. As a matter of fact, when subcooled boiling starts, most of the bubbles remains attached on the outer surface of the tube, where they can condense on the wall or depart from it. When bubbles detach during the first stage of subcooled boiling, the quickly condense in the bulk region because bulk liquid is subcooled. When the bulk temperature increases, bubbles can easily nucleate on the wall's surface and when depart from it they don't condense. When bulk boiling occurs, significant void fraction is detected. The appearance of steam in the bulk region affects the heat transfer coefficient which is characterized by fluctuations.

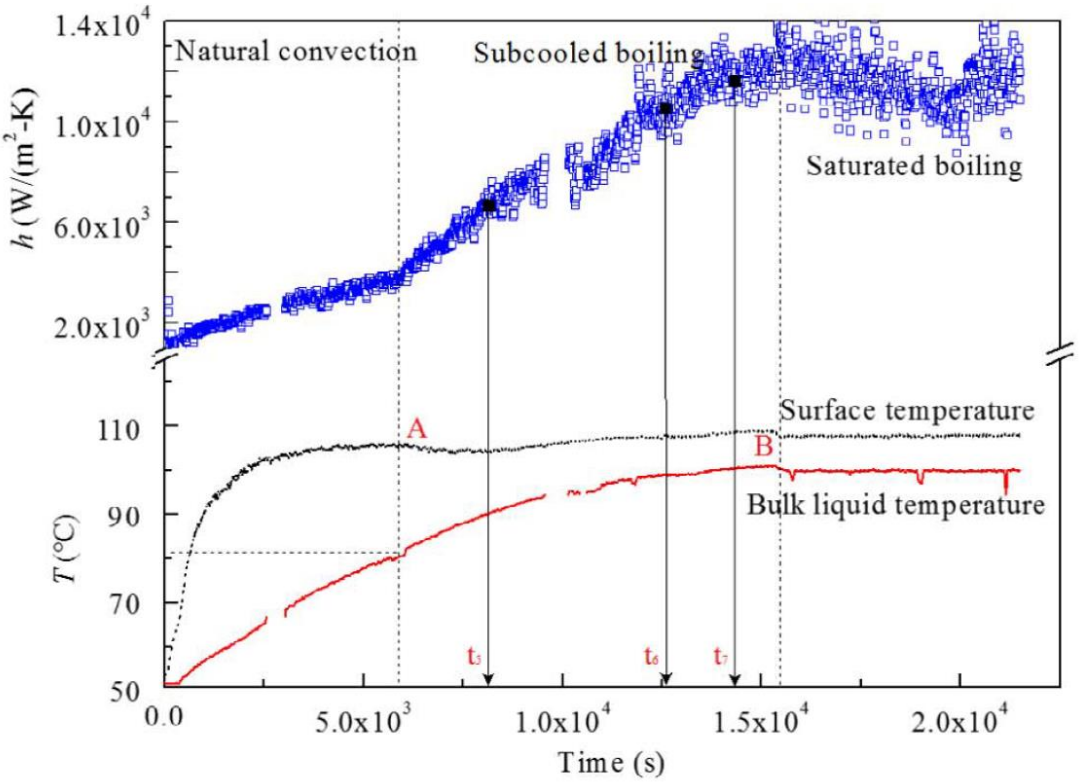

(a) H/D=72.5

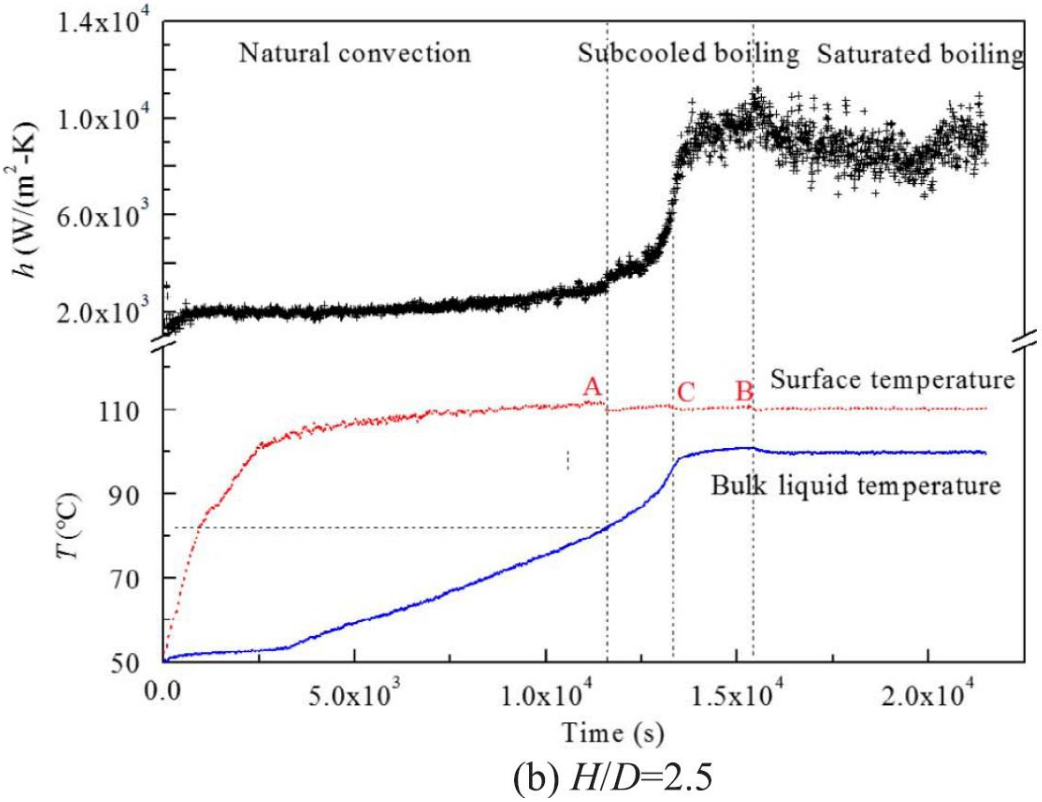

Fig. 1.9. Evolution respect to time of: bulk liquid temperature, outer surface temperature and heat transfer coefficient at different height: (a) top region H/D=72.5 (b) bottom region H/D=2.5 (Tian, Chen, Wang, Cui, & Cheng, 2018).

A comparison between the pool temperature in confined and unconfined configuration is shown in Fig. 1.10. In the case of unconfined space (black lines in Fig. 1.10), significant thermal stratification is observed at the bottom of the pool (H/D=2.5). On the other hand, the stratification is suppressed in the case of confined space (red lines in Fig. 1.10). The main reason of this result is due to the enhancement of longitudinal convection inside the glass cover. During the heat transfer process in the unconfined space, convection in the radial direction reduces the contribution of the longitudinal convection, so that the longitudinal convection between the lower and the upper region of the pool is weak in the regions far from the tube surface. As the longitudinal convection is reduced, thermal stratification is established. The confined space practically removes the horizontal flow of the water which is forced to move longitudinally suppressing thermal stratification. In this way the fluid in the lower region takes part to the heat transfer mechanism. On the other hand, when boiling heat transfer mechanism becomes dominant, convection's contribution becomes insignificant, and the effect of the confinement is weakened.

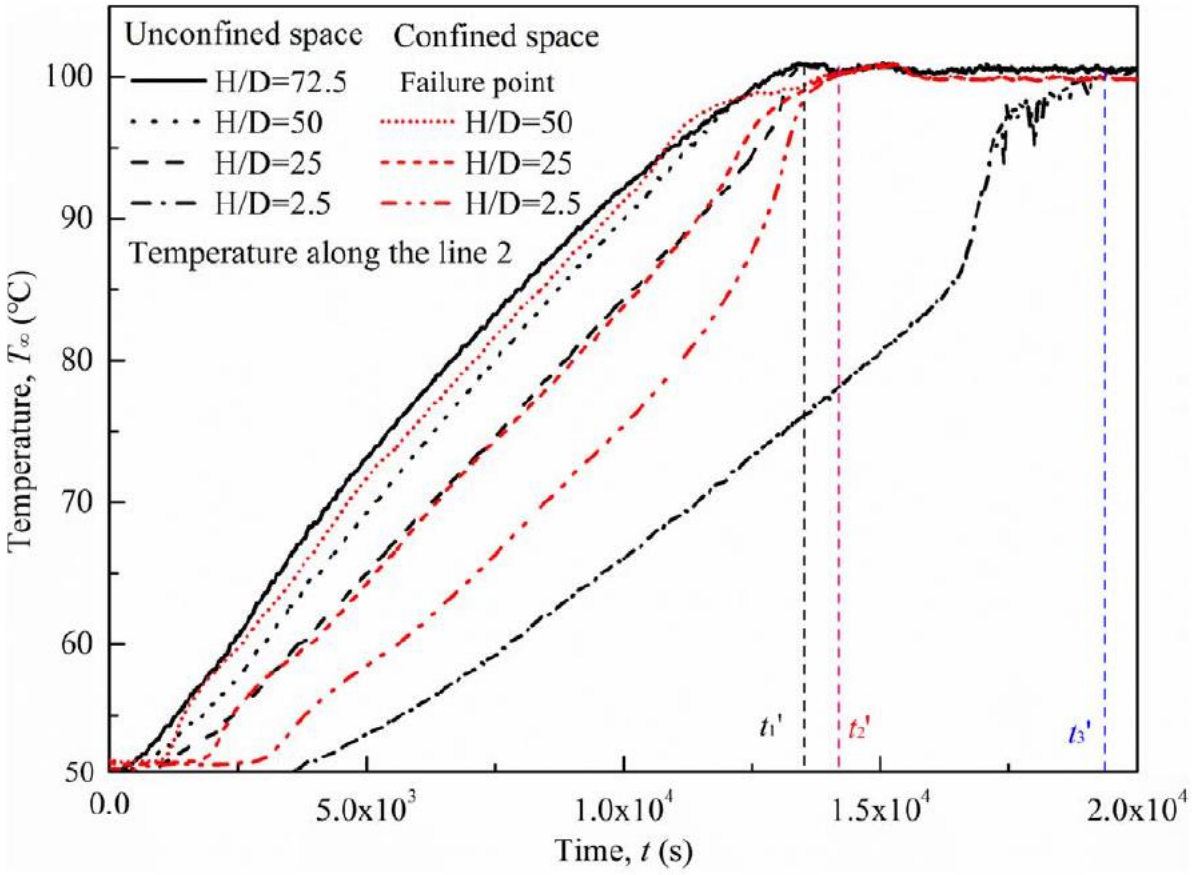

Fig. 1.10. Pool temperature evolution along line 2 respect to time at different height and for different configuration: unconfined (black lines) and confined space (red lines). (Tian, Chen, Wang, Cui, & Cheng, 2018).

In Fig. 1.11 is shown the ratio $\frac{h_{confined}}{h_{unconfined}}$, between the heat transfer coefficient in the confined and unconfined space for different values of the H/D ratio. During the saturated boiling this ratio is higher than one (heat transfer coefficient in confined space higher than the one in the unconfined space), which highlights the role of both boiling and convection in this stage. However, for higher heat fluxes (achieved increasing the oil temperature), the difference between the two configuration becomes smaller than the one observed for low heat flux (T_{in}<140 °C) because of the effect of boiling, that becomes dominant. Furthermore, for low heat flux, the enhancement of the heat transfer is more remarkable in the lower half of the tube (H/D<50) than in the upper region. Another interesting aspect is that for T_{in}=165 °C, the heat transfer mechanism is more efficient than the one at T_{in}=160. The increase of the vapor fraction to the surface drastically reduces the heat transfer coefficient in the unconfined space.

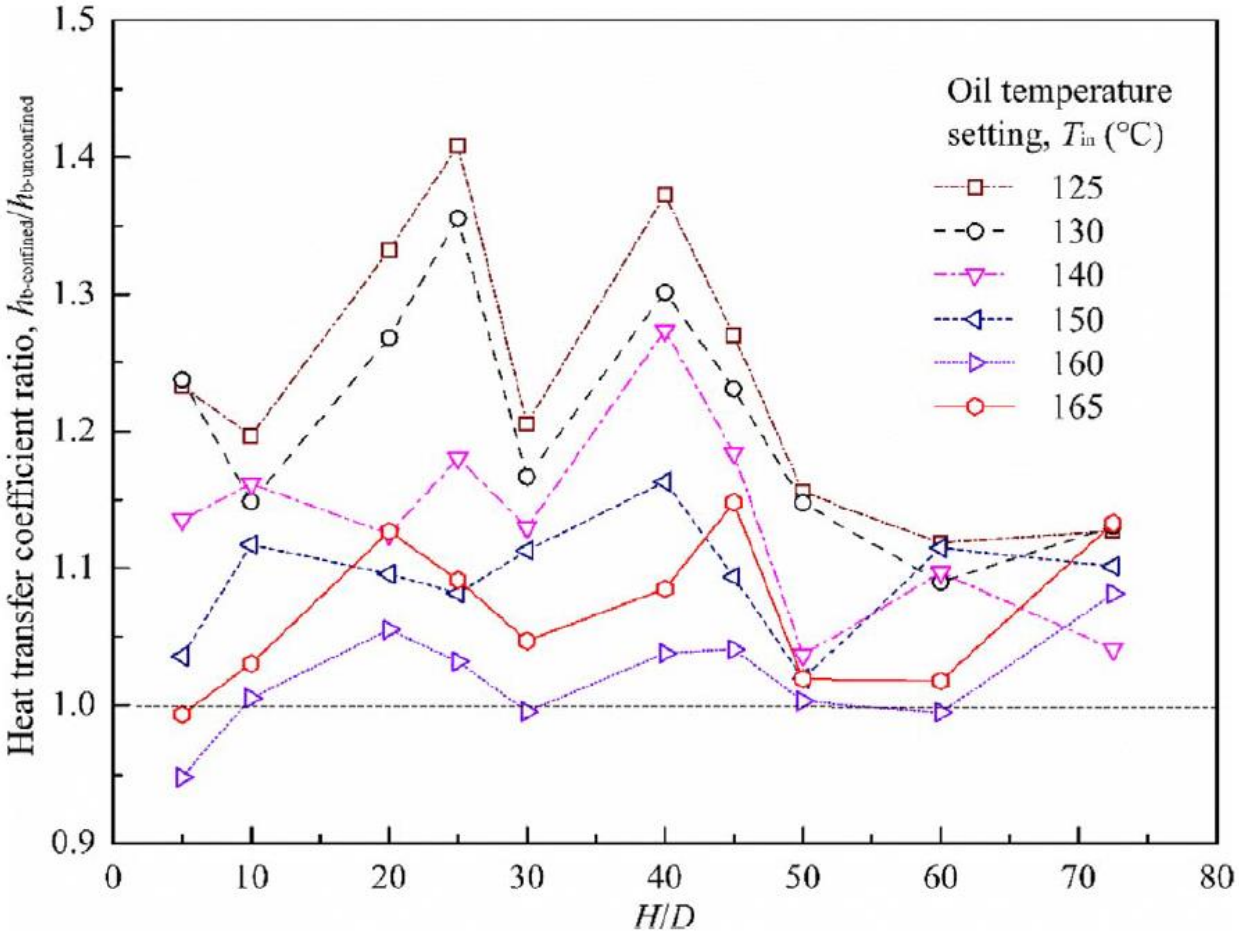

Fig. 1.11. $h_{confined}/h_{un\text{-}confined}$ variation respect to height-diameter ratio for different primary fluid temperatures. (Tian, Chen, Wang, Cui, & Cheng, 2018)).

In conclusion, the confined configuration is characterized by convective boiling, differently unconfined configuration is ruled by pool boiling. The natural convection is improved, in particular in bottom layers, by the effect of a more homogeneous boiling in the square confinement and longitudinal motion is amplified to the detriment of the radial one.

Experimental measurements focused on pool boiling and thermal stratification considering different set-up were carried out also by Ganguli, et al., in 2010. The goal of this work is to reduce as much as possible thermal stratification taking into account a wide range of system's configuration (different heat fluxes, geometries, time and spatial scales). In order to achieve this result, a boiling model was developed in order to investigate subcooled pool boiling heat transfer using a CFD code. Then the numerical results were compared with experimental measurements in order to validate the boiling model.

A schematic representation of the experimental system is shown below, in Fig. 1.12.

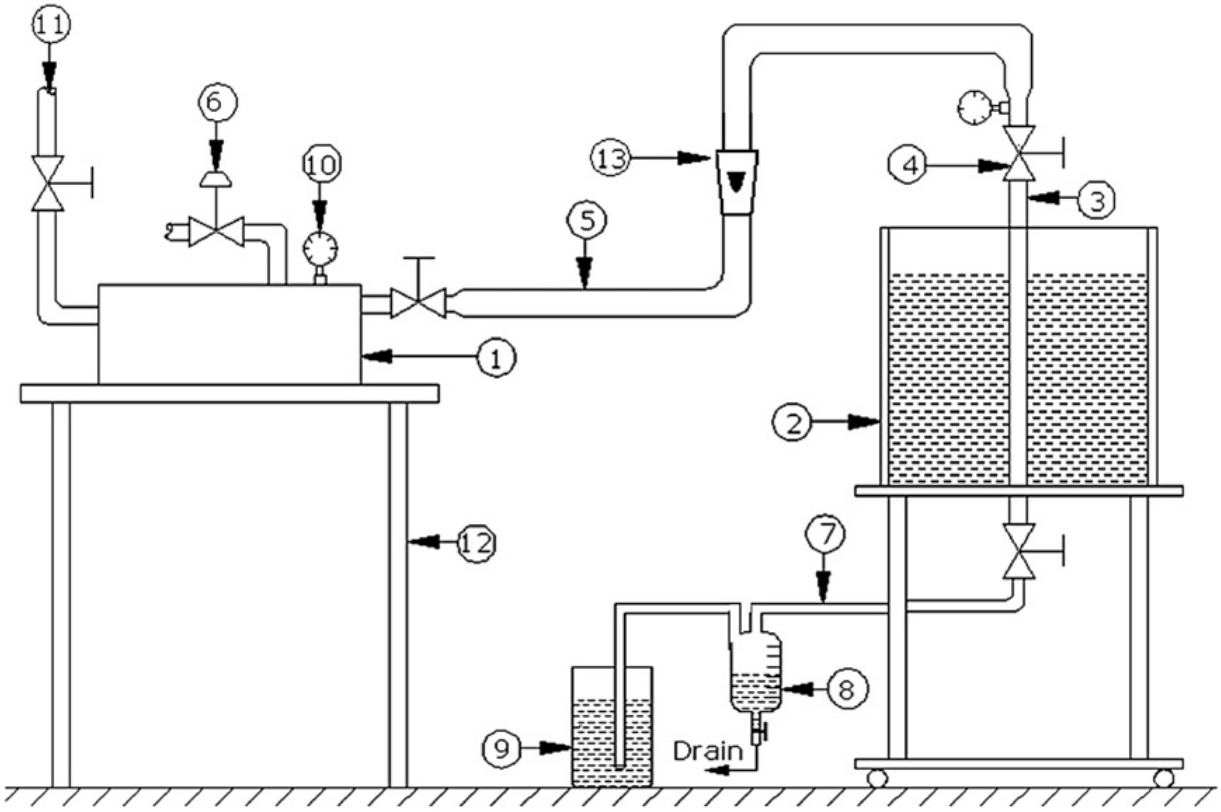

Fig. 1.12. Sketch of the experimental apparatus (Ganguli, Sathe, Pandit, Joshi, & Vijayan, 2010).

It consists of:

1. Electrically heated boiler with a maximum power of 6 kW, which produces steam flowing in the test pipe (maximum flowrate of 5 kg/h).
2. Cylindrical glass tank (inner diameter equal to 300mm, height equal to 450mm and thickness equal to 6mm) laterally insulated by a glass wool layer.
3. Test steel pipe (inner diameter equal to 20mm).
4. Testing tube and pressure detector. Pressure drops amount up to 15% when hot fluid, coming from boiler, reaches the glass tank.
5. Insulated flexible rubber hose for steam (outer diameter equal to 25mm). It helps to reduce as much as possible the heat losses.
6. Safety valve.
7. Drain tube in Teflon (inner diameter equal to 10mm) containing condensate and uncondensed steam. The two-phase mixture flows in the gravity separator in order to isolate water from steam.
8. Condensate collection vessel.
9. Vessel containing water which directly condenses the uncondensed steam.
10. Pressure gauge.

11. Water supply.
12. Stand.
13. Rotameter.

The experimental procedure is the following one: the glass vessel is filled with degassed water. Inside the electrical heater (1), water coming from the water supply (11) evaporates and becomes steam. Steam flows inside the test pipe (3) where dissipates heats to the pool water in the tank. The two-phase mixture passes through the drain tube (7) and reaches the condensate collection vessel (8) which separates by gravity the condensed steam. The uncondensed steam is discharged in a vessel containing water (9) that directly condenses the steam. There, the mass of water is monitored during the experimental procedure. The difference between the weight of the vessel at start and at the end of the experiment gives the mass of steam which did not condense during the heat exchange with the pool water. The directly condensed steam inside the vessel (9) produces an increase of temperature. The difference of temperature inside this vessel between the start and the end of the experiment is detected. Then, the heat input to the pool is obtained by subtracting from the total heat input (heat released by the electrical heater) the enthalpy of uncondensed steam. The uncondensed flowrate is obtained as the difference between the steam flowrate coming from the heater and the condensate flowrate collected by drain vessel (8).

The goal of this work is to provide a numerical method capable to predict the heat flux exchanged during the pool boiling, distinguishing the share of the different heat transfer mechanisms involved. As concerns temperature measurements, eight ungrounded K-type thermocouples (Chromel-Alumel, stainless steel sheathed, diameter equal to 3mm) are employed to evaluate the mean temperatures variation respect to time.

The experimental study was characterized by an increasing amount of input energy and by the subsequent evolution of the system in time, from 50 up to 200 s. During this time interval, subcooled boiling is observed on the outer heated surface. During the subcooled boiling, bulk water temperature is lower than the saturation one, but fluid in contact with the heated surface starts boiling and some small bubbles are formed in nucleation sites. During the subcooled boiling regime, bubbles can grow and when they reach a certain critical size (depending on different factors such as surface tension, hydrodynamics of the fluid and so on) bubbles can detach from the wall. When bubbles move through bulk fluid, they condense releasing latent heat. Experimental measurements are compared with numerical simulation, further described in section 1.2.2.

The heat transfer mechanisms occurring in a scaled passive residual heat exchanger (PRHR HX) is experimentally investigated by Tao et al. (2018) considering different thermofluid-dynamics of pressure (from 5 MPa to 15 MPa) and mass flux (from 95 $kg/m^2/s$ to 320 $kg/m^2/s$).

The test facility was built at the Shanghai Jiao Tong University and its schematic is shown in Fig.1.13. It is made by the main loop, cooling loop, purification loop and instrumentation and control system.

In the main loop, plunger pumps, able to increase the pressure up to 16 MPa, move the water from the storage tank to the regenerator. Passing through the regenerator, water receives heat from the primary fluid coming from the PRHR HX. After the regenerator, water flows inside the pre-heater, where it is heated up by Joule effect in order to reach the required temperature at the inlet section of the heat exchanger. When passes through the test section, water is cooled by the heat transfer involving the pool water in the tank. When the heat-transfer fluid exits from the PRHR HX, it is delivered to the hot side of the regenerator and then is mixed with cold water. Successively it passes through the other heat exchanger where it is cooled down and then it is discharged in the deionized water tank. Some of the most important operating parameters are shown in Table 1.3.

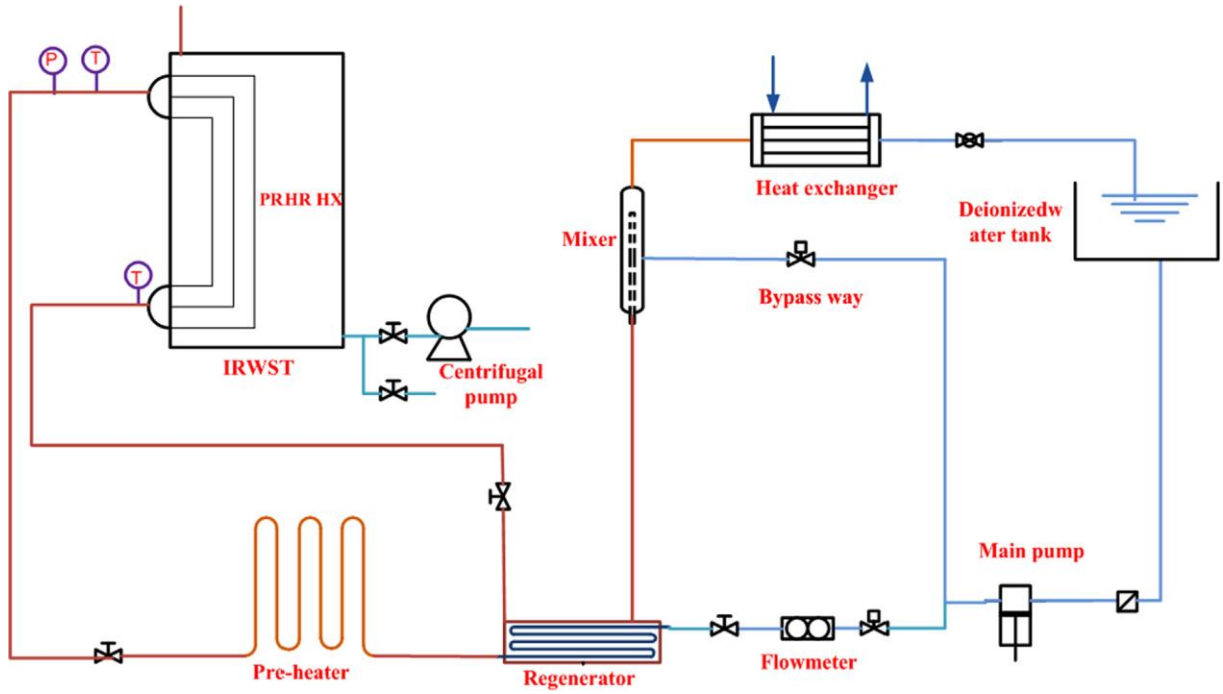

Fig. 1.13. Sketch of the test facility (Tao, Gu, Xiong, Jiang, & Xie, 2018).

Table 1.2. Primary loop operating parameters (Tao, Gu, Xiong, Jiang, & Xie, 2018).

Parameter	Pressure	Temperature	Flow rate	Heating power
UM	MPa	°C	kg/s	kW
Value	16	350	2.8	900

The test section is made by two parts: PRHR tank and PRHR HX. The first one simulates the IRWST (length equal to 1.5 m, width equal to 3 m and height equal to 6 m) and it is filled with distilled and de-ionized water at atmospheric pressure. The PRHR HX is made by a bundle of 42 symmetrically arranged C-shape rods, placed at the pool's center. Tube's diameter and pitch between tubes in the bundle are the same of an AP1000 PRHR HX (see Table 1.1). The tank outer surface is insulated by aluminum silicate wool.

One of the most critical parameters that need to be analyzed is the heat removal rate shown below, in eq. 1.2:

$$Q = W(h_{in} - h_{out}) \qquad (eq.\,1.2)$$

Where W is the mass flowrate and h is the fluid specific enthalpy. The average heat flux is defined in eq. 1.3:

$$q_{ave} = \frac{Q}{A} \qquad (eq.\,1.3)$$

Where A is the total heat transfer surface [m^2].

The water flowrate is measured by a turbine flowmeter (error < 0.5%). Its measuring range is 1.5 – 15 m^3/h. The pressure at the inlet section of the PRHR is detected by a Yokogawa EJA-150A capacitance-type pressure transducer (error < 0.1%). The water temperature is measured at the inlet and outlet sections of the C-shape tubes by two ungrounded N-type thermocouples with a sheath outer diameter equal to 0.5 mm (error < 1 °C). Almost 70 thermocouples of the same type are placed on the PRHR HX walls or between tube bundle so that local heat transfer characteristics inside the system can be evaluated. An example of thermocouples displacement is reported in Fig. 1.14.

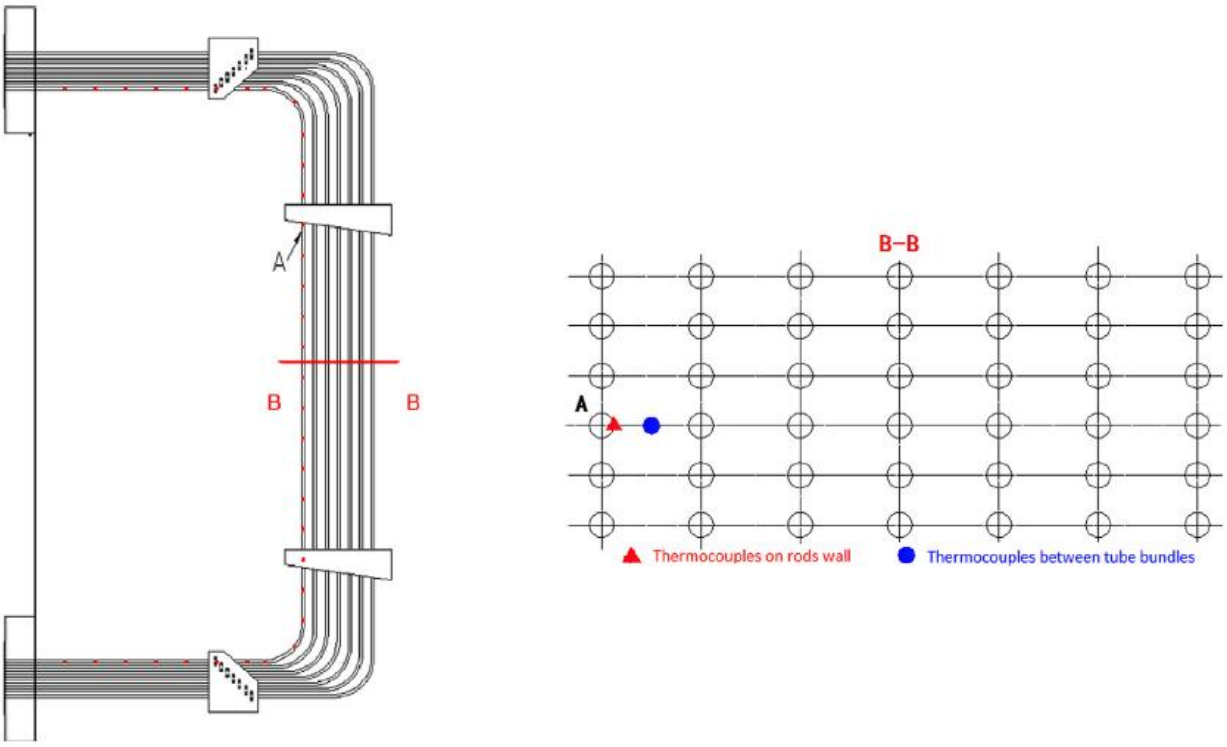

Fig. 1.14. Bundle section and thermocouples position (Tao, Gu, Xiong, Jiang, & Xie, 2018).

The heat transfer between hot primary water and pool water can be separated into three stages: convection from the hot primary water to the inner tube surface, conduction through the wall from and convection from the outer surface of the pipe to the secondary water.

In order to analyze the heat flux distribution along the tubes' length, a mathematical model, based on correlations, is developed and it is shown in section 1.2.2.

During the experimental phase, different inlet conditions were studied. The representative case chosen to describe the behavior of the system is characterized by: inlet pressure equal to 5.2 MPa, mass flux equal to 320 kg/m^2/s. At the beginning of the experiments, the temperature of the water inside the heat exchanger and inside the tank is the ambient temperature. The inlet temperature of the PRHR HX gradually rises and when it reaches 150 °C, it remains constant thanks to the pre-heater. Inlet pressure and inlet flowrate are adjusted by the monitoring and control system.

Calculated and experimental steady state temperature profile are compared in Fig. 1.16. The computed values of fluid temperature inside the pool is slightly higher than the ones obtained by experimental procedures, which means that the heat transfer rate is underestimated (almost 4% lower than the measured one). Wall temperature has a oscillating behavior. From the calculated profile it seems to be quite constant, with few degrees of variance respect to the inlet value. Actually, from the experimental data, a more complex behavior is shown. It is probably due to the

local properties that can change easily during the two-phase flow, characteristic of the PRHR HX higher region. As a matter of fact, in the lower region the detected wall temperature seems to be more uniform.

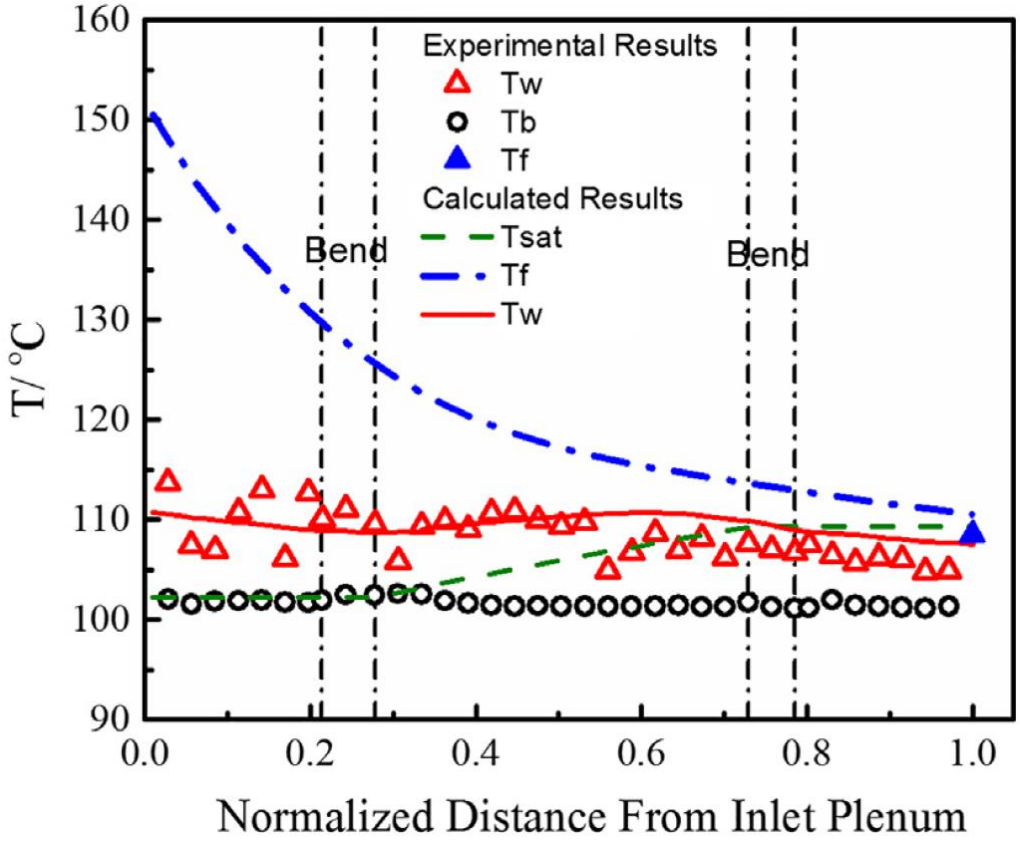

Fig. 1.15. Comparison of primary and secondary fluid temperature and outer wall temperature profiles from experiments and numerical simulations. (Tao, Gu, Xiong, Jiang, & Xie, 2018).

Normalized local heat flux (local heat flux/average heat flux) along the tube A can be displayed in Fig. 1.16. Local heat flux is computed by the numerical model that will be discussed in section 1.2.2, average heat flux was extrapolated by experimental procedures. When distance from the inlet plenum increases, the local heat flux becomes lower. It starts from a value which is 3.6 times higher than the average one, but at the outlet plenum the exchanged local heat flux is only a fourth of q_{ave}. From the calculation another important information can be extrapolated: almost 67% of the total thermal power is delivered in the upper horizontal section. About 27% is exchanged in the vertical section and almost the remaining 6% is exchanged with the lower horizontal section.

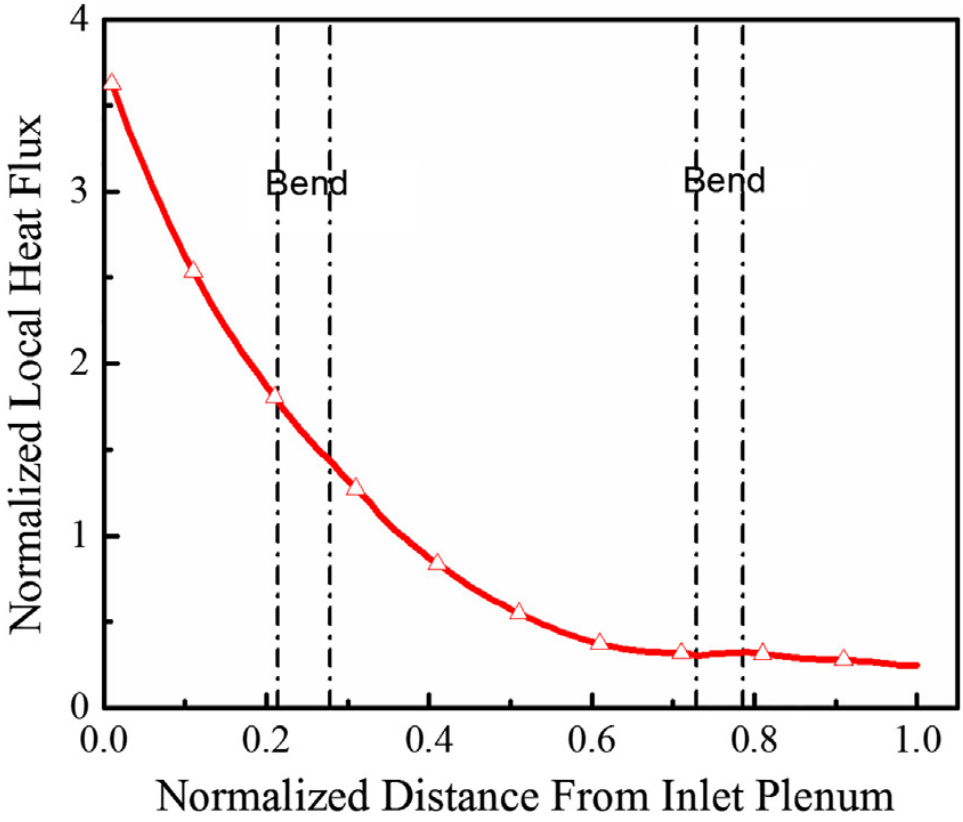

Fig. 1.16. Normalized local heat flux profile (Tao, Gu, Xiong, Jiang, & Xie, 2018).

The non-homogeneous distribution of the heat flux is strictly related to the variation of the local outer heat transfer coefficient along the PRHR HX. Its profile is shown in Fig. 1.17. In the pipe's upper horizontal section, the outer heat transfer coefficient changes between 10.6 kW/m^2/K and 6.6 kW/m^2/K. The heat transfer mechanism is enhanced by the saturated boiling. As ma matter of fact, after the upper bend, where the heat transfer mechanism changes, the heat transfer coefficient starts to decrease in the subcooled boiling regime. When it happens, the heat flux reaches its average value (approximately at the 40% of the total tube length) and the outer heat transfer coefficient is almost equal to 3.5 kW/m^2/K. From this point the heat flux drastically drops until it reaches the lower horizontal section where natural convection is the domaining heat transfer mechanism and the heat transfer coefficient is only ~ 1.0 kW/m^2/K. As a matter of fact, most of the total thermal power is released by the upper horizontal section of the tube and only for a small fraction of the upper vertical section.

The heat flux also depends on the temperature difference, and in the upper region this value is higher than in any other section. This because the fluid temperature decreases quickly thanks to the higher heat flux exchanged, affecting negatively also the inner heat transfer coefficient (increasing value of viscosity which leads to a reduction of *Re*). As a matter of fact, it changes from 3.8

kW/m^2/K to 3.2 kW/m^2/K. Another important aspect that can be useful to explain the behavior of the wall temperature (Fig. 1.15) is that during the saturated boiling (from 0 to 33% of the tube length), the wall temperature decreases, because of the improvement of the heat transfer. After that, the subcooled boiling occurs and, being a less efficient heat transfer mechanism, wall temperature becomes slightly higher, resulting in a lower temperature difference between primary and secondary fluid.

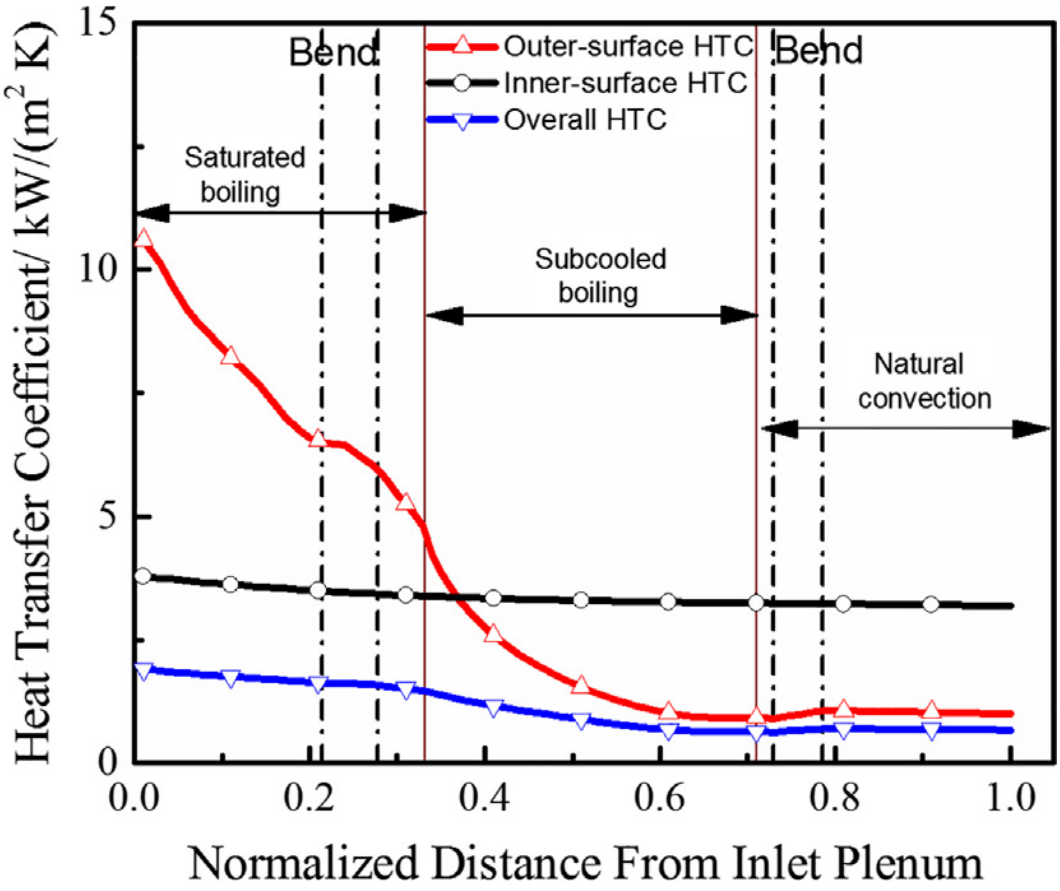

Fig. 1.17. Distribution of the heat transfer coefficient along the tube (Tao, Gu, Xiong, Jiang, & Xie, 2018).

After a detailed analysis of the heat transfer mechanisms, a parametric analysis is performed. Three different values of mass flux, inlet temperature and pressure are studied, showing always a good agreement between numerical predictions and experimental results.

Increasing all these parameters, a benefit on the heat transfer coefficient was detected. The reason is clearly that increasing the mass flux, liquid velocity increases, which has a positive feedback on the *Re*. It produces a higher inner-surface heat transfer coefficient. Furthermore, also the outer heat transfer mechanism is affected by the inner one because the thermal resistance is dominated by the convection inside the tube. Lower primary fluid velocity means that its energetic content is released in a shorter time in the upper regions. In this way, saturated boiling regime (the most efficient one)

goes on for a shorter distance. Subcooled boiling regime decays even easier because the temperature difference between primary fluid and the bulk of the tank is smaller and natural convection regime (the less efficient one) can be established even at the center of the horizontal section.

Also the effect of inlet temperature was investigated: increasing the inlet temperature, the resulting jump of temperature between the tube's inner region and the pool increases and the exchanged heat flux increases too.

Finally the variation of the inlet pressure doesn't significantly affects the heat transfer mechanism.

To finish, the test 6 x 7 C-shaped tubes heat exchanger is studied in different operating conditions, demonstrating that local heat flux is strongly affected by the temperature at the inlet section and by the water mass flowrate inside the tube.

1.2.2 *Numerical simulations*

Ge et al. (2018) investigated the behavior of secondary side fluid and heat transfer performance of the AP1000 PRHR HX immersed in IRWST, through 3D CFD model implemented through the CFD commercial package of FLUENT. They showed how the fluid motion is characterized by strong buoyancy force inside the tube bundle heat exchanger, in particular in the upper horizontal section. Then the water goes transversally, enhancing the thermal mixing in the upper region of the pool. After moving far from the PRHR HX and reaching the remote boundary of the IRWST, the fluid goes back to the heat source transversely and water recirculation is established. Fig. 1.18 shows the temperature distribution inside the IRWST after 2000s.

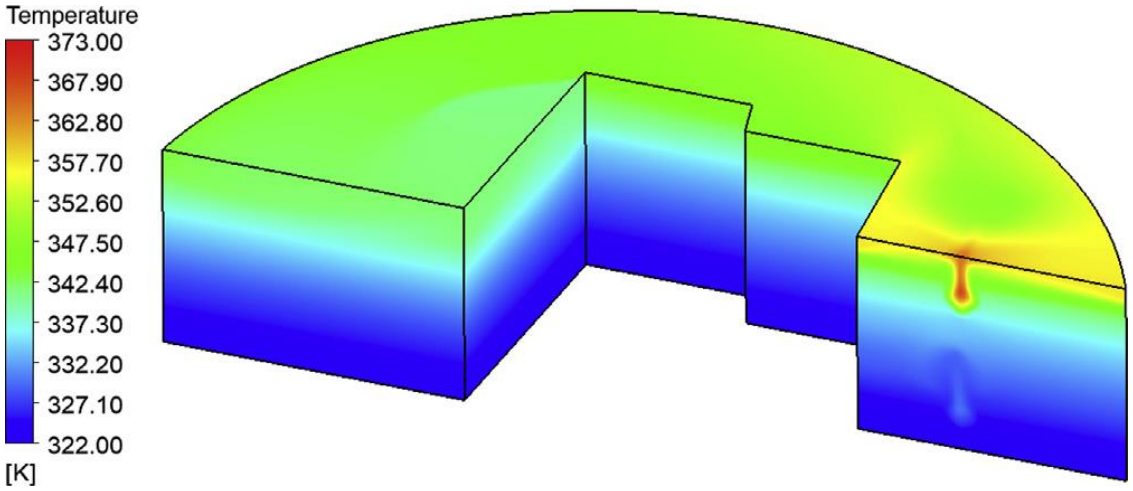

Fig. 1.18. Water temperature distribution inside the IRWST after 2000 s (Ge, Tian, Qiu, & Su, 2018).

In the lower part of the IRWST a non-contributing region exists. The non-contributing mass of water inside the pool starts to take part in the heat transfer mechanism only after 6500s. As a matter of fact, pool water temperature in the upper and horizontal sections is affected by a larger temperature gradient than in the lower section of the heat exchanger (Fig. 1.19(a)). The x-axis shows the normalized tube length, from the section at inlet to the one at the outlet of the heat exchanger. When liquid temperature reaches the saturation value, it remains constant. As the simulation goes on, saturated water occupies the upper regions of the IRWST, thanks to the effect of the buoyancy forces. The temperature profile inside the tank is showed in Fig.1.19 (b), where the x-axis shows the normalized height of the IRWST with the origin placed in the bottom of the pool. Bulk temperature is higher in the upper regions because of the thermal stratification. As simulation's time increase, bulk temperature starts to increase also in the lower region, which means that water is contributing to the heat transfer process and that the thermal stratification process is expanding to lower regions. Bulk temperature profile starts to show a relatively small

difference of temperature between the top and the bottom of the pool only after 6500 s, meaning that also the lower region of the pool are involved in the heat transfer process. This difference of temperature gets smaller and smaller until the saturation temperature is reached everywhere in the IRWST and thermal stratification is suppressed.

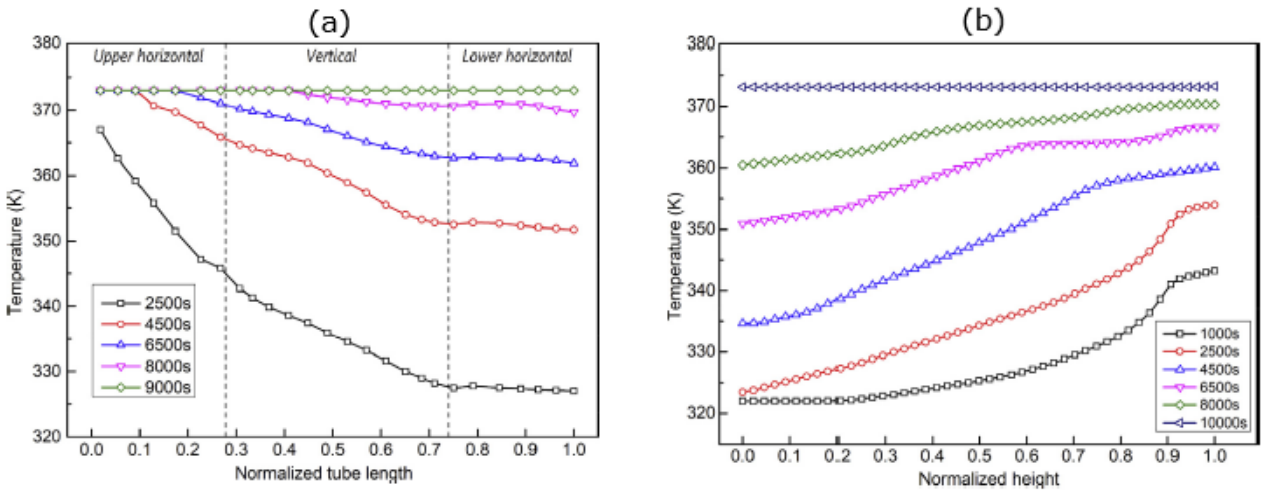

Fig. 1.19.Thermal stratification build up in: (a) IRWST regions near the PRHR HX, (b) IRWST bulk region (Ge, Tian, Qiu, & Su, 2018).

One of the most important parameters obtained from the simulation is the heat flux through the PRHR HX. The local heat flux profile after 8000s is showed in Fig. 1.20. Hot primary fluid is mostly cooled when it passes through the upper horizontal section. As a matter of fact, the highest value of heat flux is computed at the inlet section, where it is more than the 400% of the average heat flux, and about 70% of the total removed power is extracted in the upper horizontal section. Most of the thermal power is removed in the upper horizontal section because of the phase transition occurring on the secondary side (IRWST). Then about the 25% of the total power is exchanged in the vertical section of the tubes and about 5% in the lower horizontal section.

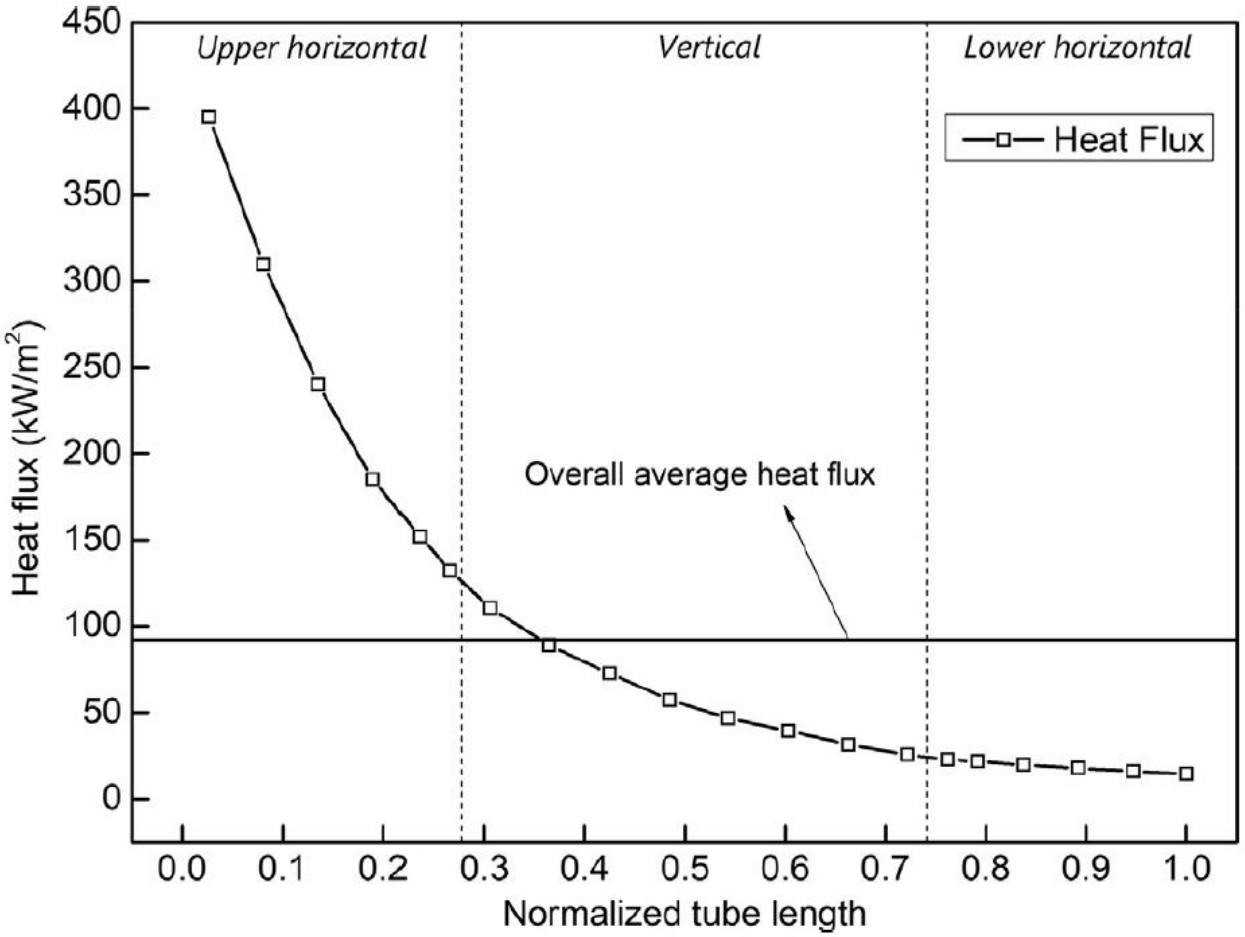

Fig. 1.20. Local heat flux profile (Ge, Tian, Qiu, & Su, 2018)

As regards the inner and outer average heat transfer coefficient, its profile within the tube bundle is shown in Fig. 1.21. On the outer surface of the tubes bundle, the heat transfer coefficient shows a remarkable variation, from 24 kW/(m^2 K) at the inlet to 2.6 kW/(m^2 K) at the outlet. For the primary coolant, the heat transfer coefficient profile shows a slightly reduction through the bundle because of the variation of water thermophysical properties, from 5.9 kW/(m^2 K) to 4.1 kW/(m^2 K).

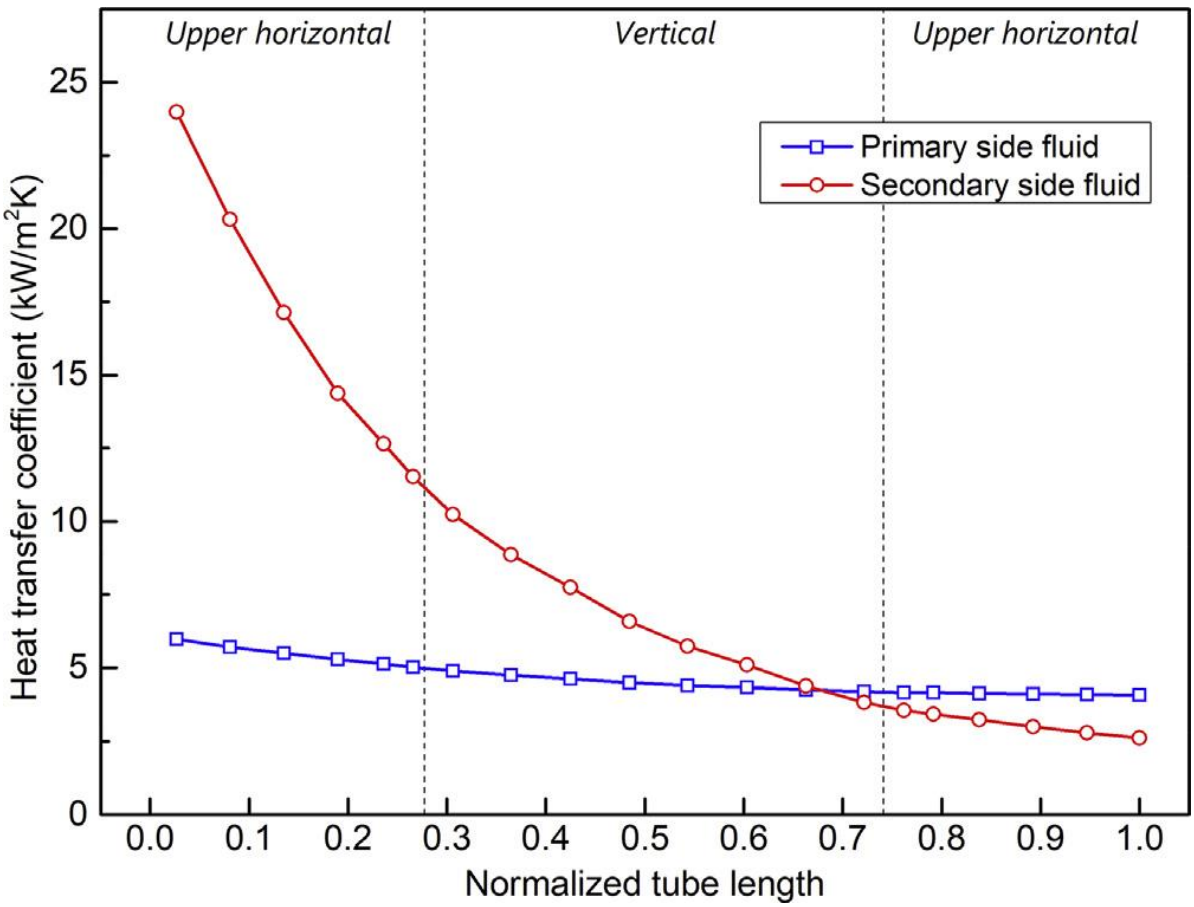

Fig. 1.21. Heat transfer coefficient along the heat transfer tubes (Ge, Tian, Qiu, & Su, 2018).

Verma et al. (2013) investigated the effect of suppression of thermal stratification in one of the GDWP sectors of an AHWR using shrouds. These shrouds are used to create a natural recirculation loop that can help to improve the cooling process of the isolation Condenser (IC), which is the heat source. Loops produced by the shrouds are capable to increase the effective mixing and thermal stratification can be avoided.

Simulations are carried out using RELAP5. At first, the performance of the pool with no shroud was investigated. Time dependent temperature evolution at different height of the pool are shown in Fig. 1.22. As the vertical temperature stratification builds up, in the bottom of the pool (below the level of the IC), water doesn't contributes to the heat transfer process. On the other hand, the upper regions of the pool get continuously heated. Assuming that at the center of the pool a heat source is placed, and this is following the decay heat released by the core, boiling conditions are reached on the top of the pool after only 25 h. This result is much lower than the expected three days (grace period).

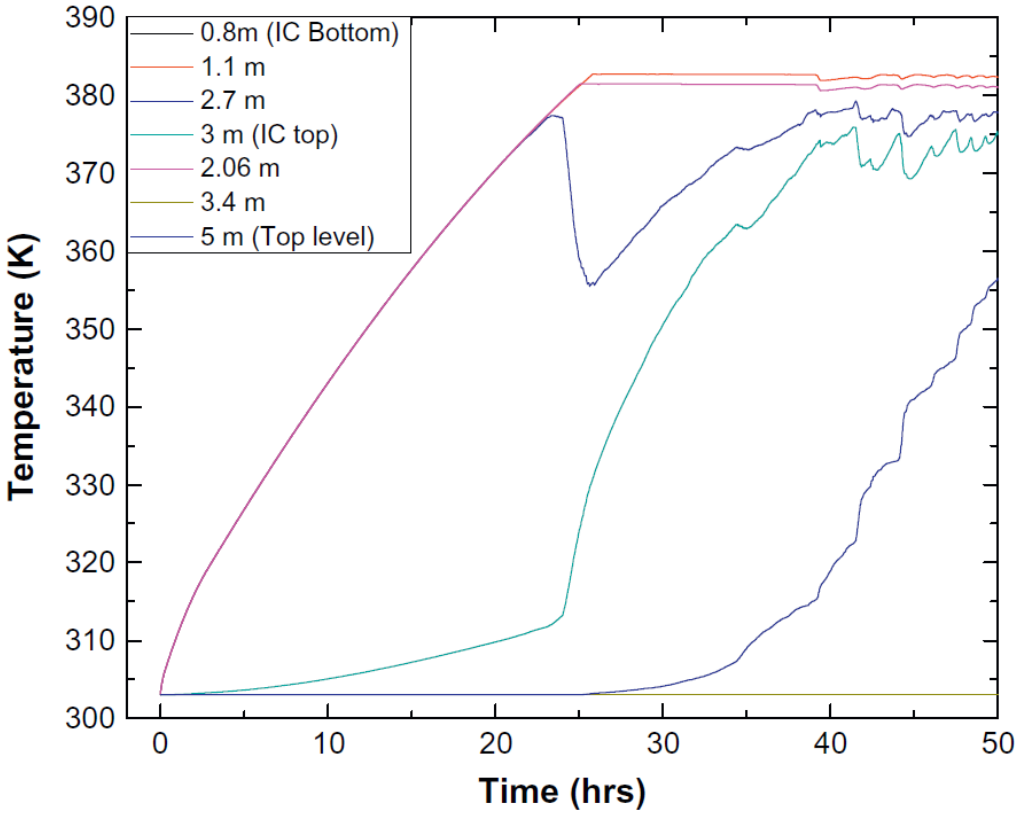

Fig. 1.22. Time dependent temperature evolution at different height of the pool without shrouds (Verma, Nayak, Vikas, & Vase, 2013).

Successively, the configuration of the pool without the shrouds is compared with three different situations: GDWP with three, five or seven shrouds. A seven shrouds configuration is shown in Fig. 1.21.

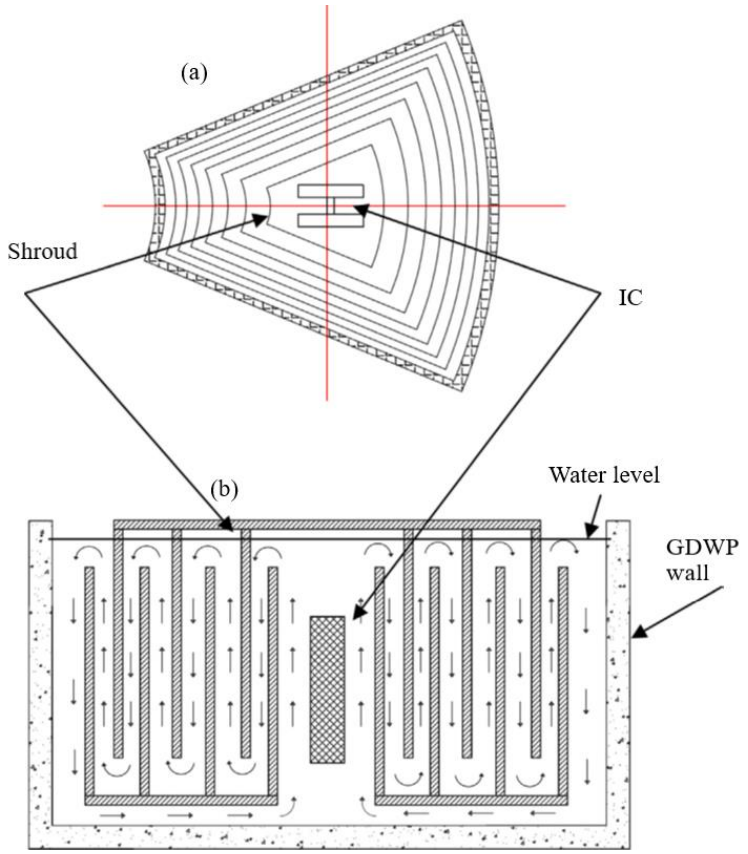

Fig. 1.23. One sector of GDWP with a concept of seven shrouds. (a) Top view. (b) Cross section (Verma, Nayak, Vikas, & Vase, 2013).

For this analysis, thermal conduction through the shrouds wasn't taken into account, assuming adiabatic shrouds. Temperature and mass flow rate time behavior is examined for a period of three days. The temperature distribution of the water entering and leaving the IC compartment is displayed in Fig. 1.24. It shows a fluctuating profile for five (Fig. 1.24(a)) and seven shrouds (Fig. 1.24(b)) configurations. This phenomenon can be better understood by the mass flowrate at different sections, which is shown in Fig. 1.25. Fluid passing through the IC section is heated up. When the temperature rises, buoyancy force is established. When it is strong enough to win the fluid-dynamic resistance in the furthest channel from the heat source, a peak of the flowrate occurs, which enhances the thermal mixing and the temperature at the inlet and outlet of the first channel is practically the same. Considering the configuration with 7 shrouds rather than 5 but the same flow area, this phenomenon is magnified because of the higher pressure drop through the channels. As the fluid temperature drops again, a reduction of the mass flowrate is observed and consequently the temperature difference between the inlet and the outlet of the IC section becomes larger and the cycle starts again. Anyway, the improved mixed guarantees a pool temperature lower than the saturation one for the grace period.

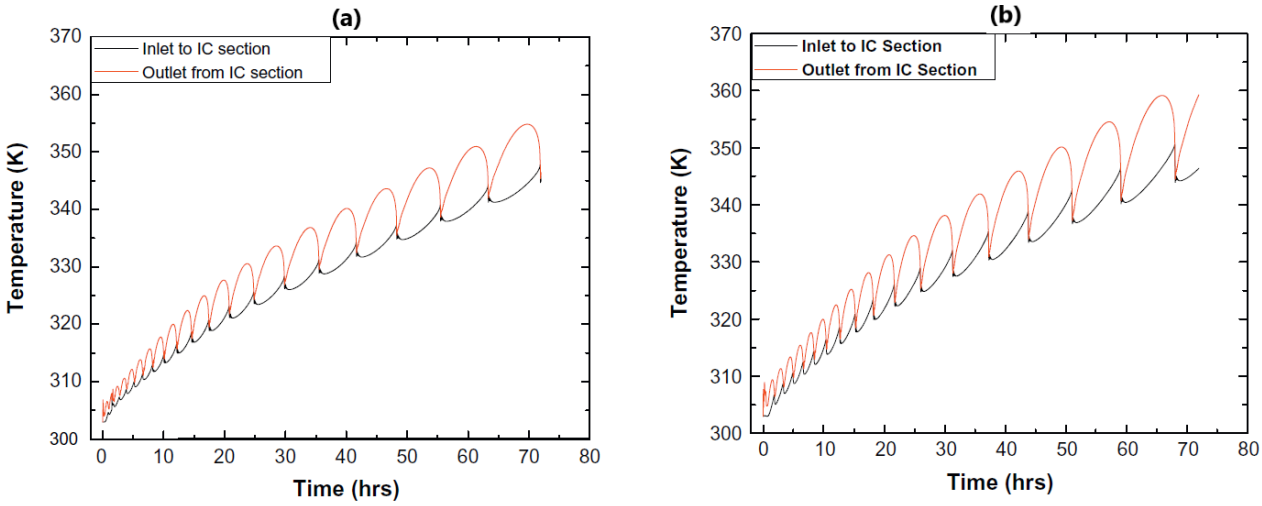

Fig. 1.24. Temperature at the isolation condenser inlet and outlet sections for (a) five shrouds and (b) seven shrouds configuration (Verma, Nayak, Vikas, & Vase, 2013).

Considering simpler configuration with a low number of shrouds (3 shrouds configuration), lower final temperature and much smaller fluctuations are observed. On the other hand, higher peaks in the mass flow rate time dependent behavior are detected, because of the lower pressure drop through the channels (higher flow area and shorter length of the loop). Another important aspect is that after a flowrate's peak, there is a transitory flow reversal. This is due to water temperature in the innermost channel of the shrouds that is higher than the water temperature flowing in the IC section, as a consequence of the mixing process.

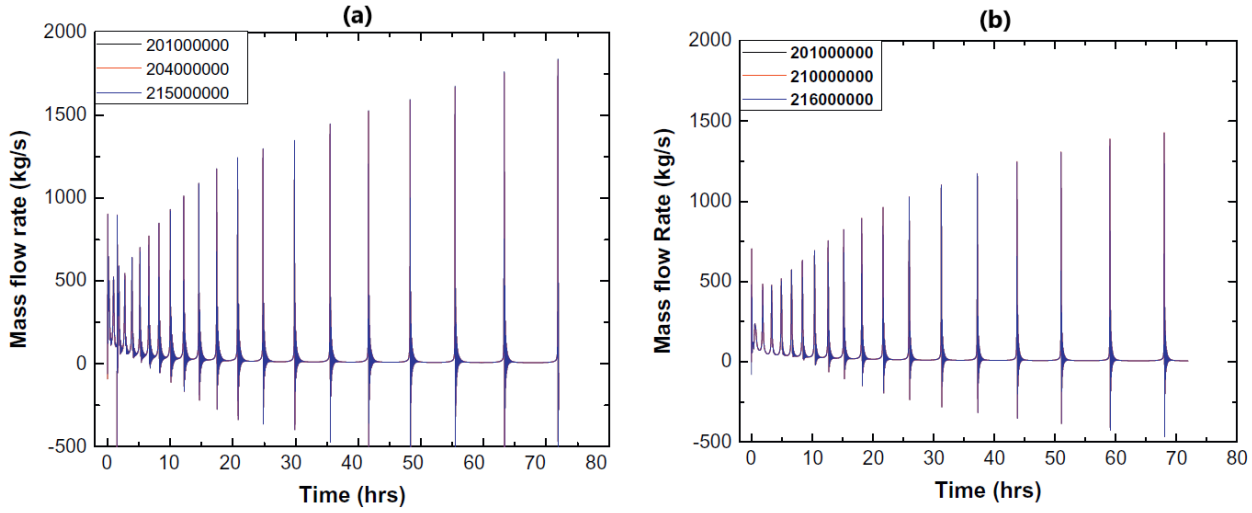

Fig. 1.25. Mass flowrate at the inlet and outlet of the Isolation Condenser's section and in the outermost shroud for (a)five shrouds and (b) seven shrouds configuration (Verma, Nayak, Vikas, & Vase, 2013)..

Highlighting the benefits coming from the reduction of the number of shrouds, the analysis of a three shrouds configuration is performed. As a matter of fact, the temperature profile is characterized by practically no fluctuation, if compared with the previous configurations. It can be seen in Fig. 1.26.

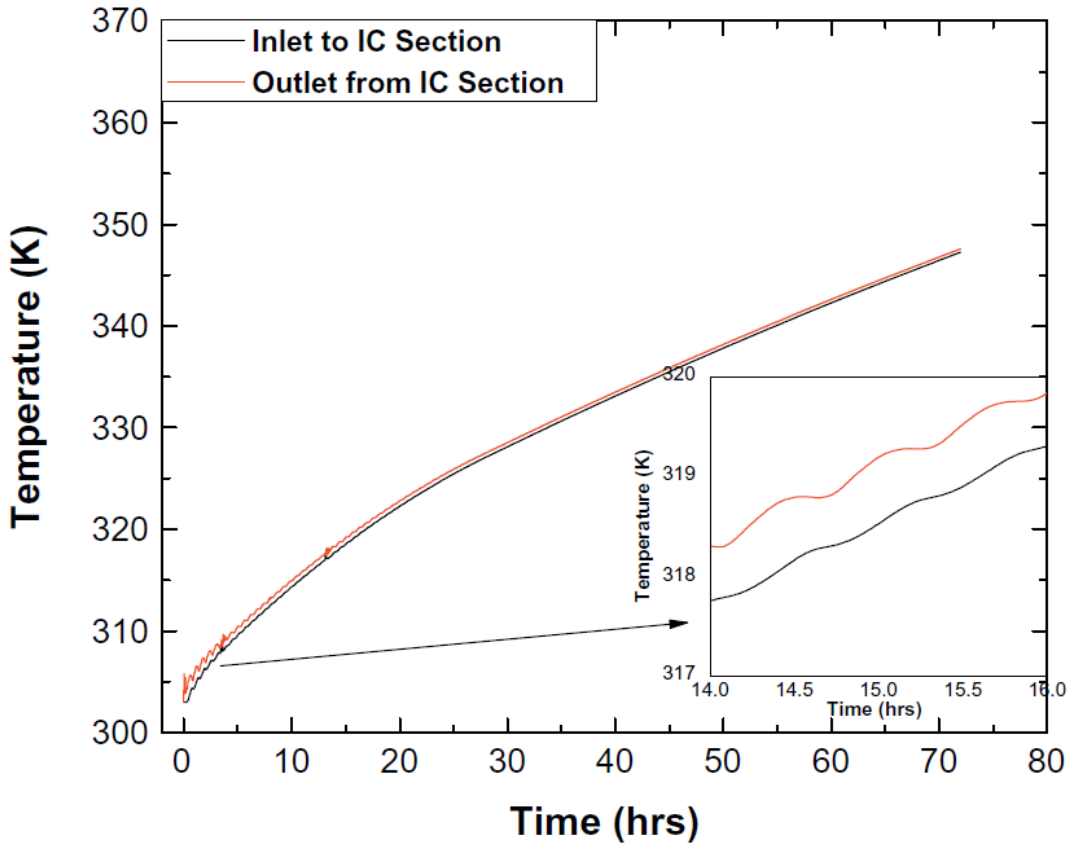

Fig. 1.26. Time dependent behavior of temperature at the Isolation Condenser's section for three shrouds configuration (Verma, Nayak, Vikas, & Vase, 2013).

Comparing the average temperature profile of the three configuration, it's easy to see that the lower one is obtained by the one adopting three shrouds, as shown in Fig. 1.27.

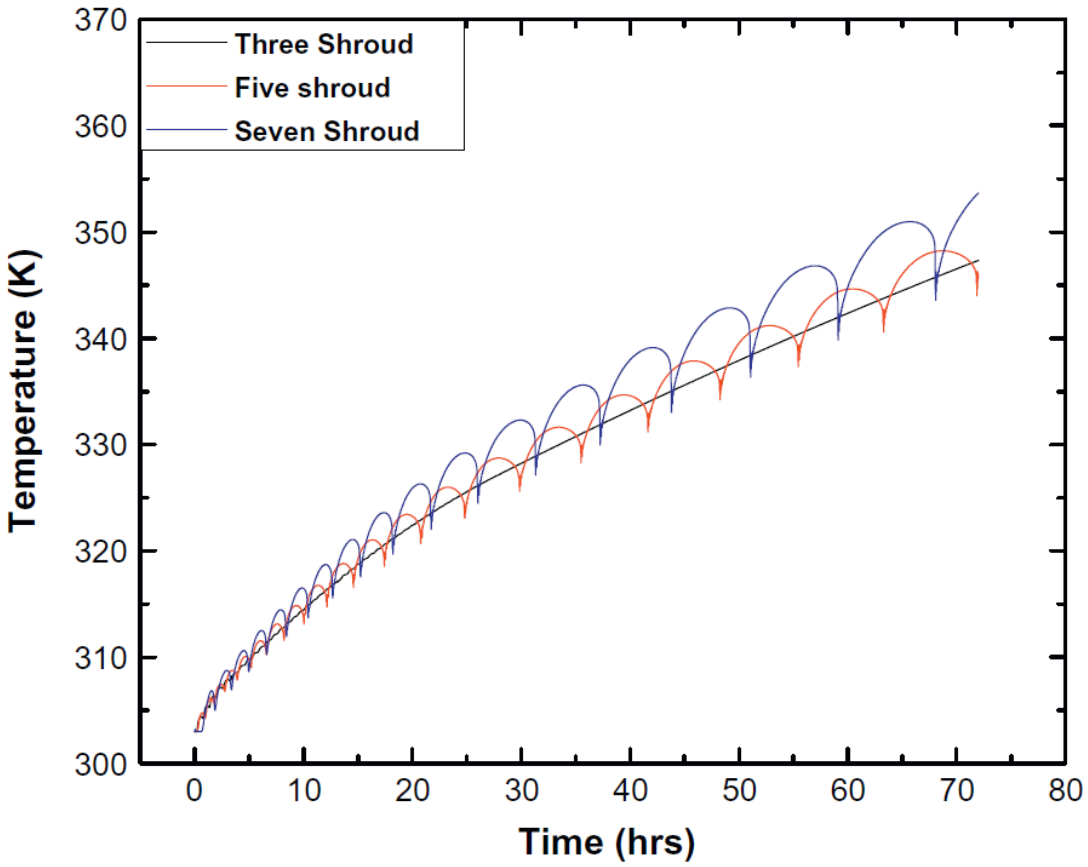

Fig. 1.27. Comparison of average temperature of last downward flow shroud (Verma, Nayak, Vikas, & Vase, 2013).

This result is achieved also thanks to the behavior of the mass flow rate, reported in Fig. 1.28. It is positive for most of the time and barely affected by fluctuations.

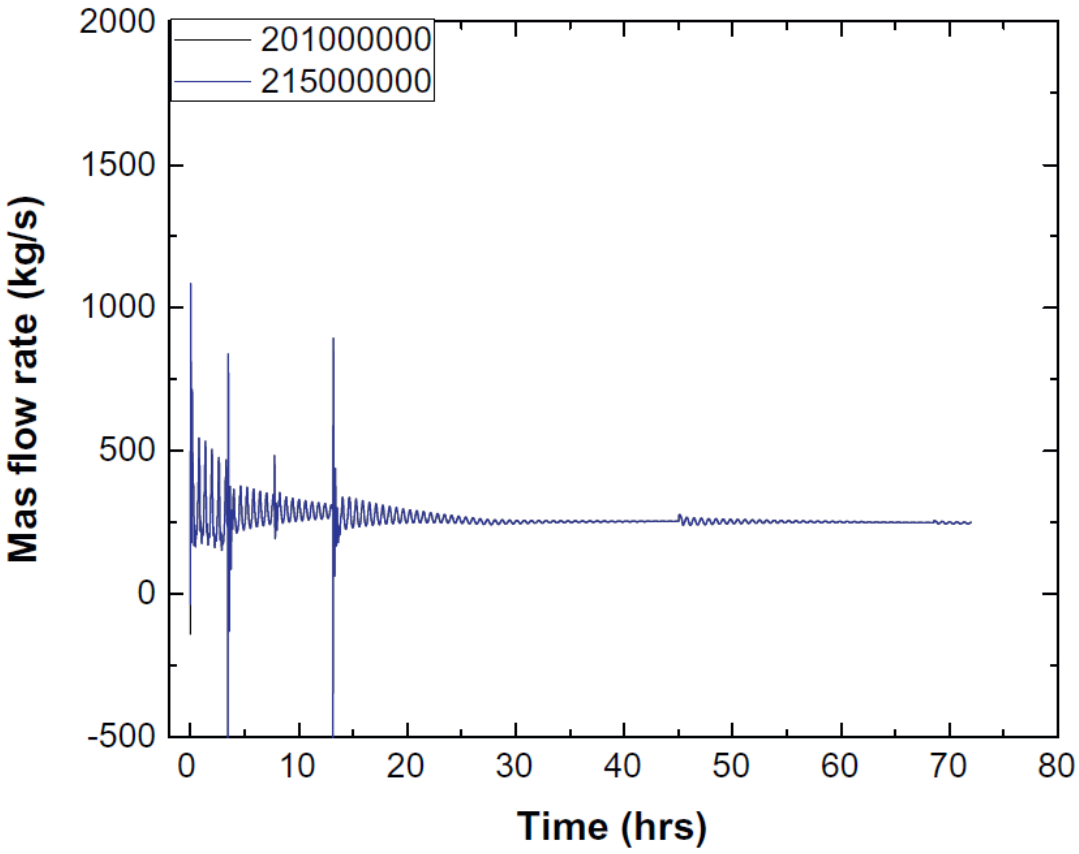

Fig. 1.28. Mass flow rate for three shrouds configuration (Verma, Nayak, Vikas, & Vase, 2013).

In conclusion, simulations show that shrouds configuration in a GDWP helps to suppress thermal stratification within the grace period after a SBO. Furthermore, a three shrouds configuration reduces oscillation of temperature and mass flow rate.

Another study that deserves to be mentioned concerning shrouds effect in GDWP of the AHWR is the one published by Kumar (b) et al. (2017). It is focused on a parametric study which investigates the effects of: number of shrouds (single-shroud and three shrouds configuration), different flow areas, different height, different materials and influence of leakages. The characteristic time of these analysis is higher than the above-mentioned research and it is equal to ten days. Also in this case the simulations are carried out using RELAP5.

The single shroud configuration, Fig. 1.29, is the simplest one. The vertical base plate provides both structural support for the vertical wall and constitutes the channel through which water can flow in loop.

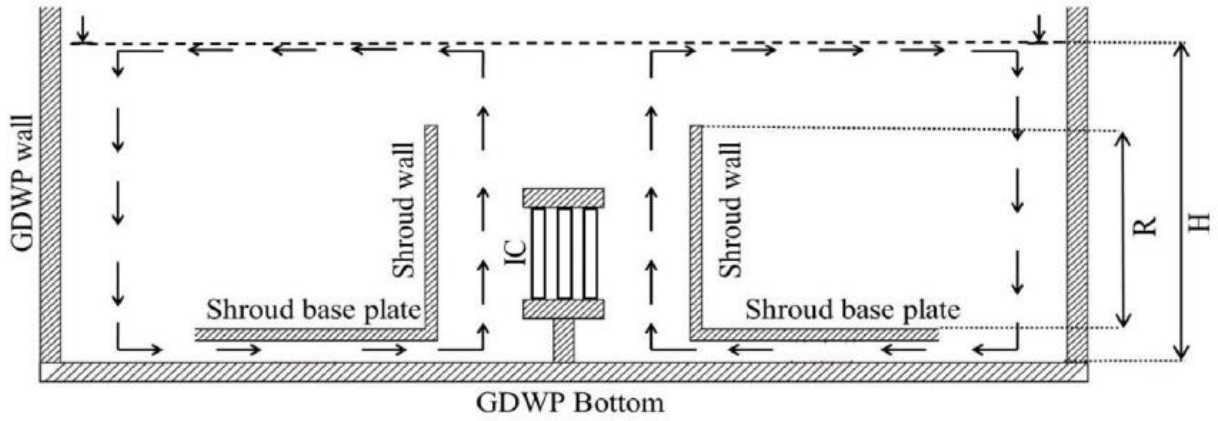

Fig. 1.29. Sketch of single-shroud configuration. R is the shroud wall's height and H is the water level. (Kumar (b), Grover, Vijayan, & Kannan, 2017).

In order to study geometrical effects on this configuration, the flow area of the IC section changes between 4%, 10%, 25% and 40% of the cross section area of a pool's sector . Configurations with different flow area are called respectively SS1, SS2, SS3, SS4. For each set of flow area, the ratio between the shroud's height (R) and the water level (H) is changed, as reported in Table 1.3.

Table 1.3. . Water level-to-height ratio for single shroud configuration (Kumar (b), Grover, Vijayan, & Kannan, 2017).

Configuration	Height of shroud (z) [m]	Height of the water level (H) [m]	z/H [-]
R1	3.45	5.85	0.589
R2	3.85	5.85	0.658
R3	4.25	5.85	0.727
R4	4.65	5.85	0.795
R5	5.05	5.85	0.863

All possible combinations between SS and R configurations are analyzed. At first, the effect of the spacing variation with a fixed configuration R is investigated (R1). The temperature variation evaluated at the outlet of the IC as a function of the entire time of the simulation (Fig. 1.30 (a)) is basically the same for all the configurations except for the SS4, corresponding to the largest flow area. At the beginning of the simulation (Fig. 1.30 (b)) all the profiles show a peak, but for SS4 this peak is softer and delayed. At the end of this transient, SS4 profile becomes the lower one and it is characterized by a delayed boiling (almost 12 h). Since the SS4 configuration seems the best one at improve mixing and delay boiling inside the pool, the shroud ratio R is changed only for the last flow area configuration (SS4). Results are shown in Fig. 1.30 (c) and 1.30 (d). They show that the effect of R has practically no impact on the time required to reach saturation conditions inside the pool. Under this conditions, boiling can be avoided for almost of 5.5 days.

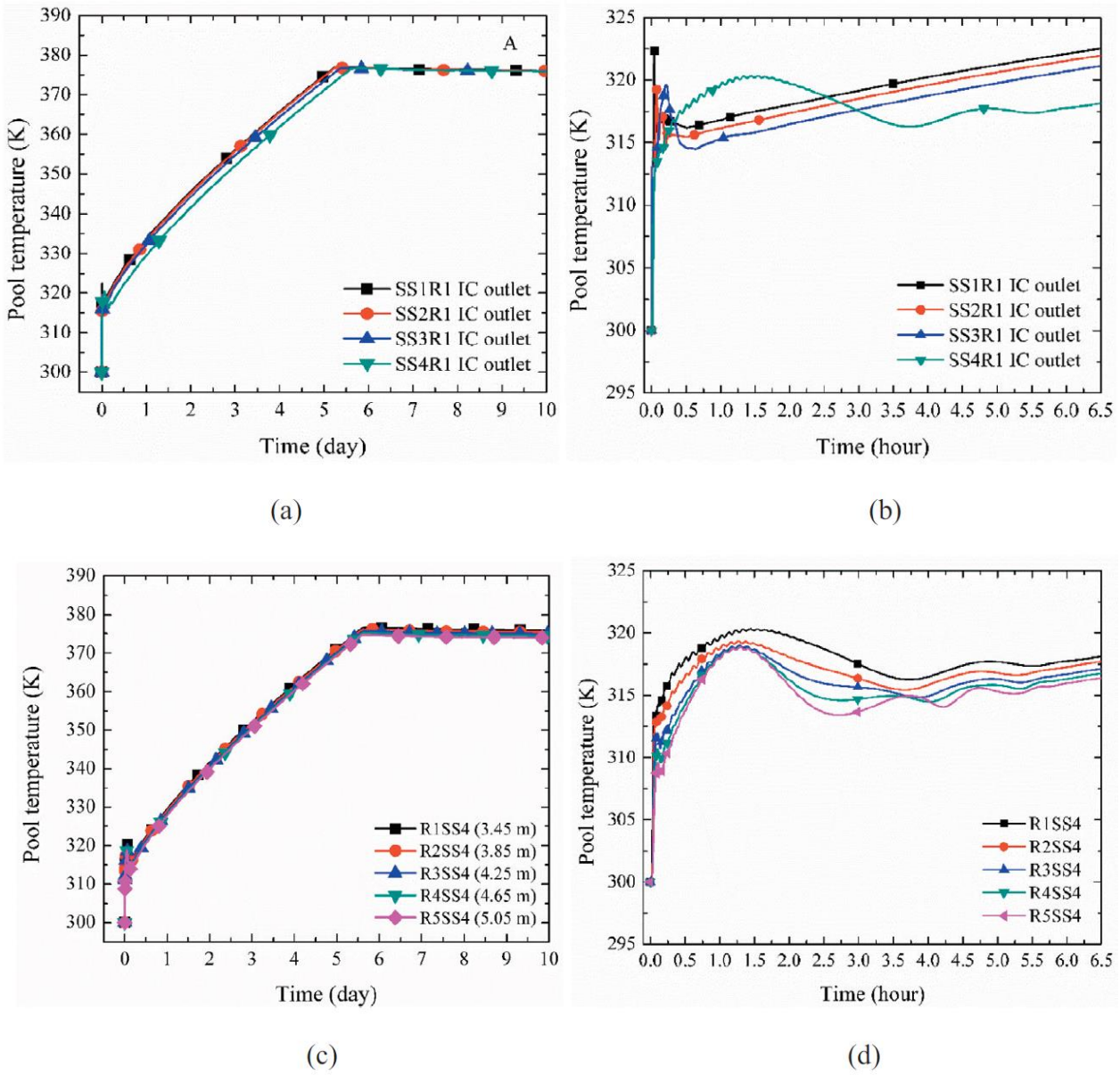

Fig. 1.30. Time dependent temperature at the outlet section of the IC (a) for 10 days and (b) for first 6.5 with fixed R configuration equal to R1 and different SS configurations; (c) for 10 days and (d) for first 6.5 for fixed SS configuration equal to SS4 and different R configurations (Kumar (b), Grover, Vijayan, & Kannan, 2017).

Then the performance of three-shrouds configuration is investigated. The system is shown in Fig. 1.31.

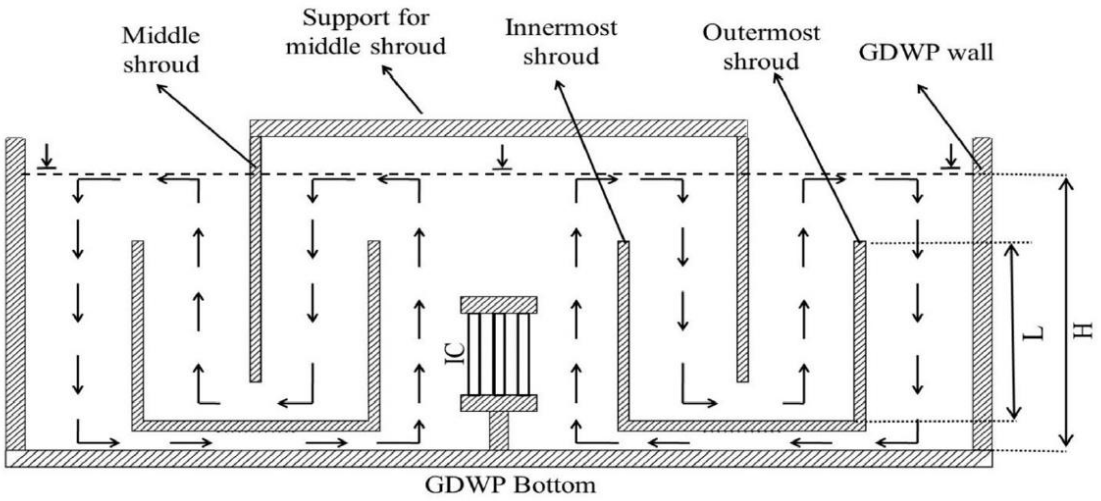

Fig. 1.31. Sketch of single-shroud configuration. L is the shroud's height and H is the water level. (Kumar (b), Grover, Vijayan, & Kannan, 2017).

As for the previous case, the flow area of the IC section is varied between 4%, 10%, 25% and 40%. The remaining area is divided equally, in order to have the same flow area in the other channels. The height of all the shrouds is the same for each simulation, as the bottom clearance. The shroud height varies between L1 to L5, as shown in Table 1.4.

Table 1.4 Water level-to-height ratio for three-shroud configuration (Kumar (b), Grover, Vijayan, & Kannan, 2017).

Configuration	Height of shrouds (z) [m]	Clearance between shrouds [m]	Height of the water level (H) [m]	z/H [-]
L1	3.45	2.0	5.85	0.589
L2	3.85	1.6	5.85	0.658
L3	4.25	1.2	5.85	0.727
L4	4.65	0.8	5.85	0.795
L5	5.05	0.4	5.85	0.863

Again, the z/H ratio if fixed and then temperature variation at the IC outlet is evaluated for increasing flow areas. Results shown in Fig. 1.41 are summarized in Table 1.5.

Table 1.5. Time required to reach saturation conditions inside the pool for different three-shrouds configurations (Kumar (b), Grover, Vijayan, & Kannan, 2017).

Configurations	TS1 saturation time (days)	TS2 saturation time (days)	TS3 saturation time (days)	TS4 saturation time (days)
L1	9.55	9.20	8.10	8.90
L2	9.95	9.65	9.15	9.70
L3	9.95	9.94	9.92	9.95
L4	7.10	7.10	6.85	5.95
L5	7.05	7.00	6.85	6.65

Figures from Fig. 1.41(a) to Fig. 1.41(e), shows the z/H ratio progressively higher. Fig. 1.41 (d) and 1.41 (e), corresponding to L4 and L5 configurations, show that reducing too much the clearance between shrouds produces negative effects in terms of prolonged heat removal by natural circulation. As a matter of fact, the poorest results are obtained adopting configurations L4 and L5: saturation condition are reached almost in 7.10 days (L4 with TS1 and TS2) or, in the worst condition, in 5.95 days (L4 with TS4), as shown in Fig. 1.32 (d). The main reason is associated to the lower flowrate inside the recirculation loop provided by the shrouds due to the higher pressure losses through the channels. On the other hand, for values of the shroud height ratio L1, L2 and L3 combined with shroud spacing configurations varying TS1, TS2, TS3 and TS4, pool water reaches saturation conditions between 9 and 10 days. There are some exception like the cases of TS3 and TS4 at L1 (Fig. 1.32 (a)), where saturation conditions are reached after 8.1 and 8.9 days respectively.

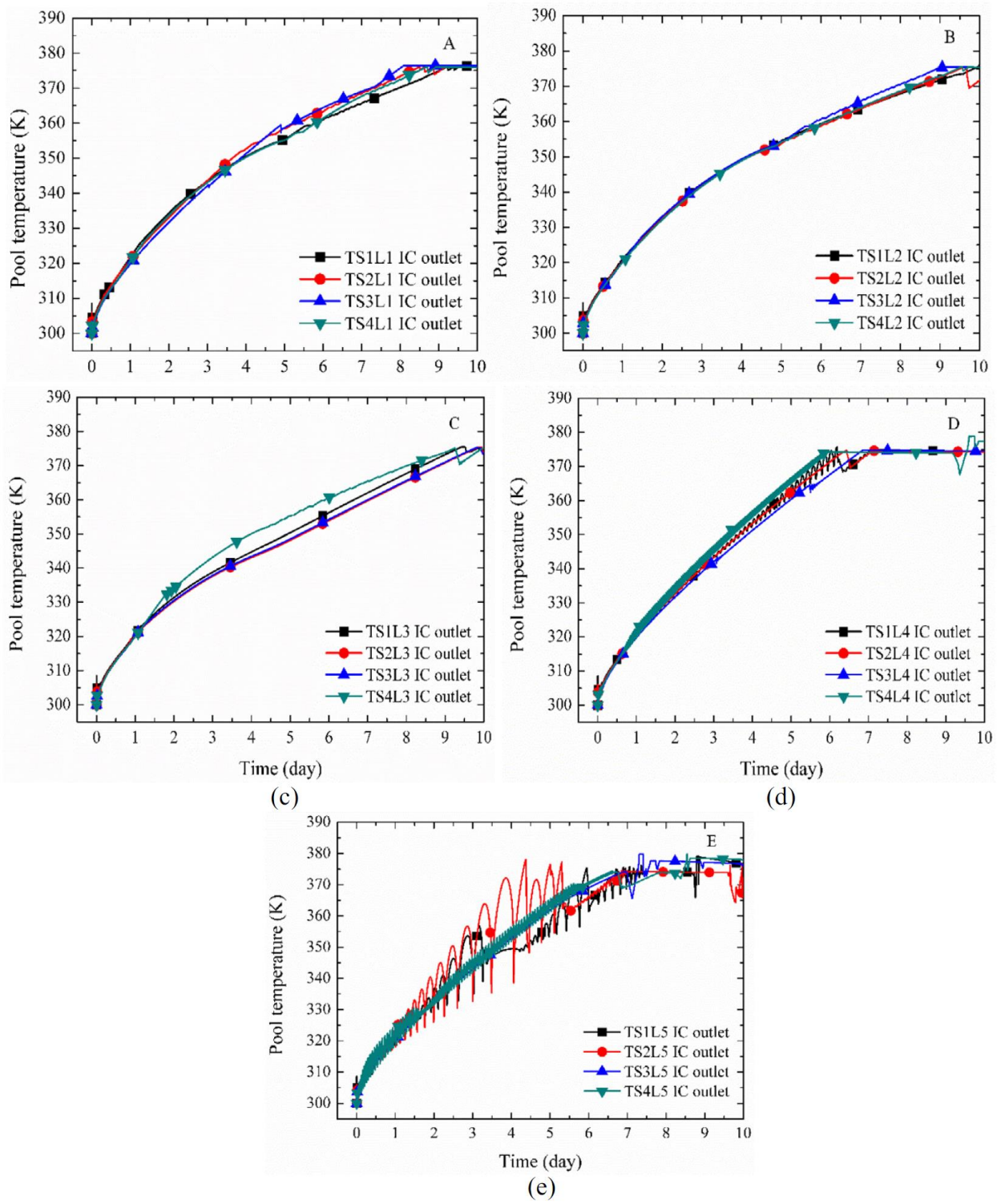

Fig. 1.32. Time dependent temperature at the outlet section of the IC for different flow area values for fixed values of water level-to-height ratio: (a)L1, (b)L2, (c)L3, (d)L4 and (e)L5 for three shrouds configuration. (Kumar (b), Grover, Vijayan, & Kannan, 2017)

A further analysis is performed in order to evaluate the effect of the different materials on conductivity through the shrouds. In the above-mentioned simulation the effect of conductivity was neglected. In order to perform this evaluation, the GDWP TS3L3 configuration is considered (corresponding to shroud's length of 4.25 m and ratio L/H=0.727, spacing ratio between shrouds equal to 25% for each channel).

The chosen material are: steel, Brass, Aluminum, copper and insulator material. Respective values of thermal conductivity are 50, 109, 205, 385 and 0 W/mK. Results are shown in Fig. 1.33.

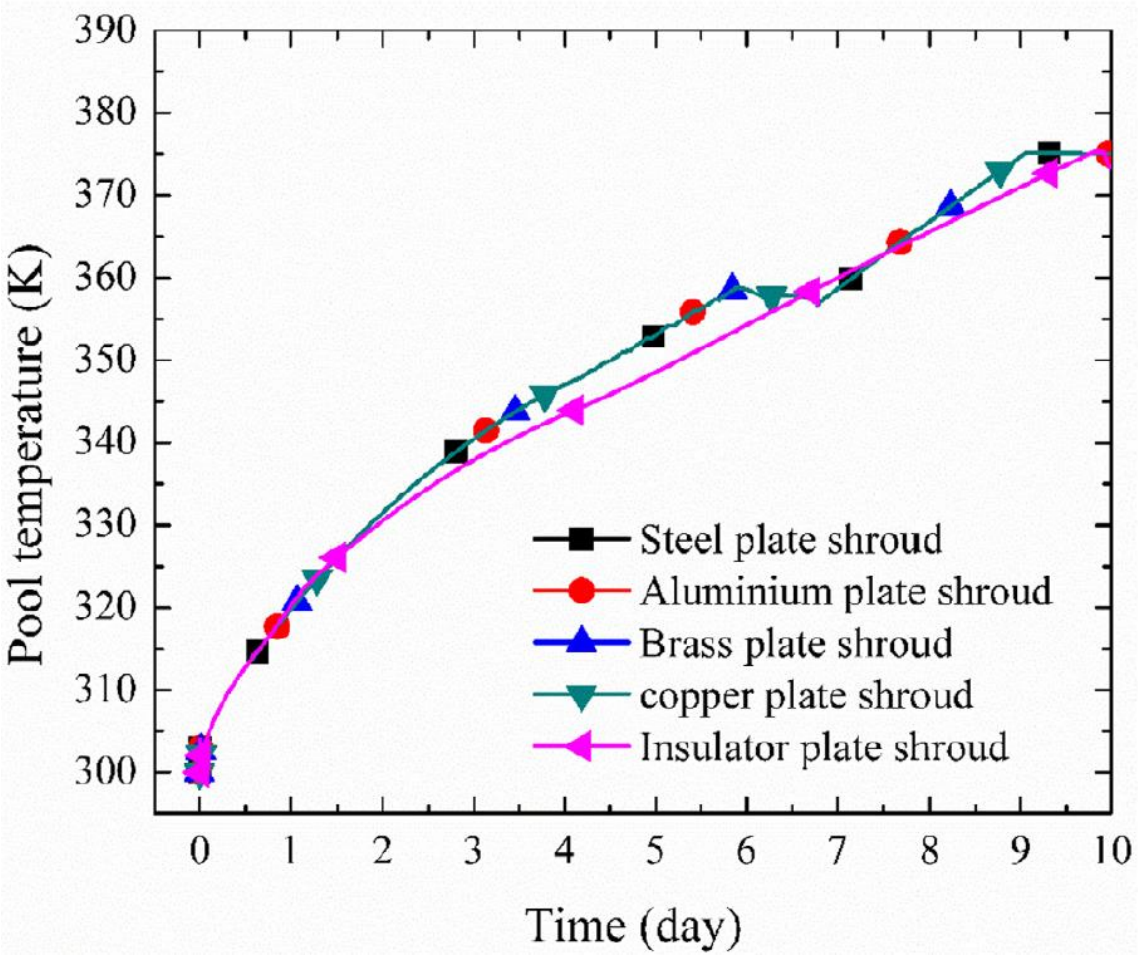

Fig. 1.33. Pool temperature variation at the IC section for different thermal conductivities assuming L3,TS3 three-shrouds configuration(Kumar (b), Grover, Vijayan, & Kannan, 2017).

There is no significant variation between the considered material, except for the insulator which provides a lower temperature profile. Furthermore, insulator material such as plastic materials are lighter and cheaper, which represent another strong point of this choice.

Finally the effect of leakages through the middle shroud is observed. The obtained results are shown in Fig. 1.34.

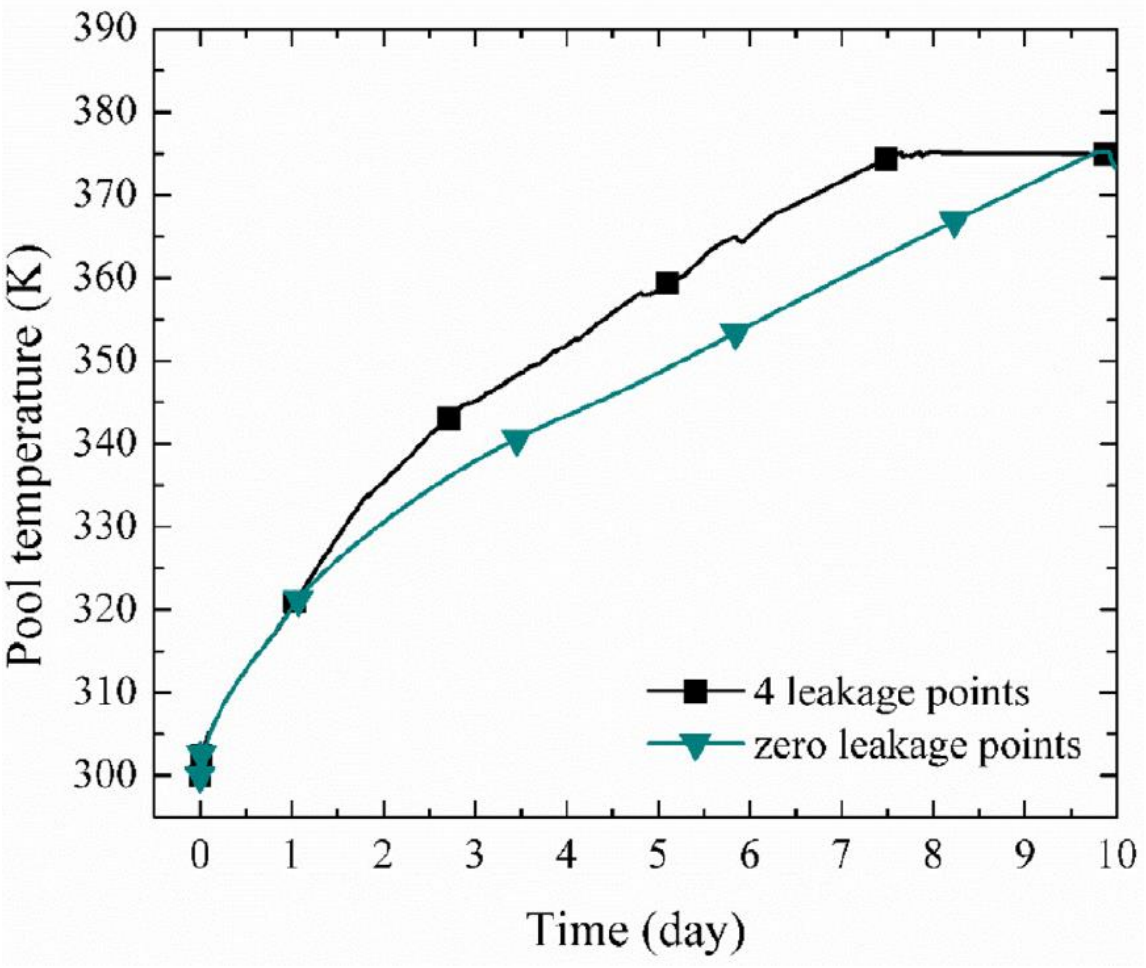

Fig. 1.34. Effect of leakage with 4 leakage point equally distributed through the middle shroud on temperature at IC outlet on pool side for TS3L3 configuration (Kumar, Grover, Vijayan, & Kannan, 2017).

Providing shorter paths for hot water deteriorates the mixing process and the saturation in the pool occurs earlier (almost three days earlier).

So, the best configuration that can be achieved in this kind of system is provided by three shrouds made by nonconductive or perfectly insulated material. As regard the geometrical arrangement L1, L2 and L3 layouts seem to be more effective in suppressing thermal stratification whatever the shroud spacing is. All three shrouds flow area configurations (TS1-TS4) show similar results for shroud height ratio L3.

The numerical study carried out by Tian et al. (2017) brings attention to the scale problem of experimental analysis in the field of pool boiling and natural circulation.

CFD was used to investigate the main properties of saturated pool boiling in the confined space, establishing a numerical model based on a PRHR HX placed in a IRWST, which are applied in

AP1000. The computational work was performed using a commercial version of FLUENT (version 15.0).

During the initial stage of the simulation, subcooled boiling is the heat transfer process through which the outer tubes' surfaces release heat to the water in the IRWST. When water reaches the saturation temperature, saturated boiling occurs. VOF (Volume Of Fluid) model is used to simulate boiling. The vapor-liquid phase transition is modeled by a UDF (User Defined Function). One of the advantages of the VOF model is that it is capable to track the interface between liquid and vapor and the bubbles' topological deformation. From the numerical model point of view, liquid water is considered the primary phase while vapor is treated as the secondary phase for VOF. The model's description is reported below.

Interface's tracking is achieved by solving continuity equations for small volume fractions of the two phases of fluid as follows:

- Mass conservation

$$\frac{1}{\rho_l}\left(\frac{\partial}{\partial t}(\alpha_l\rho_l) + \nabla\cdot(\alpha_l\rho_l\vec{v})\right) = S_l \qquad (eq.\,1.4)$$

$$\frac{1}{\rho_v}\left(\frac{\partial}{\partial t}(\alpha_v\rho_v) + \nabla\cdot(\alpha_v\rho_v\vec{v})\right) = S_v \qquad (eq.\,1.5)$$

  Where α is the volume fraction [-], ρ is the density [kg/m^3], v is the velocity vector [m/s] and S is the volumetric mass source term [kg/m^3/s].

- Momentum equation

$$\frac{\partial}{\partial t}(\rho\vec{v}) + \nabla\cdot(\rho\vec{v}\vec{v}) = -\nabla p + \nabla\cdot\left(\mu(\nabla\vec{v} + \nabla\vec{v}^T)\right) + \rho\vec{g} + F_V \qquad (eq.\,1.6)$$

  Where p is the pressure [Pa], μ is the dynamic viscosity [Pa s] and F_v is the interface-induced volume force [N]. Fluid density and fluid viscosity are evaluated respectively through eq. 1.7 and eq. 1.8:

$$\rho = \rho_l\alpha_l + \rho_v\alpha_v \qquad (eq.\,1.7)$$

$$\mu = \mu_l\alpha_l + \mu_v\alpha_v \qquad (eq.\,1.8)$$

- Energy equation

$$\frac{1}{\rho}\left(\frac{\partial}{\partial t}(\rho H) + \nabla\cdot(\rho_l\vec{v}H) = \nabla\cdot(k\nabla T) + S_h\right) \qquad (eq.\,1.9)$$

Where k is the effective thermal conductivity [W/m/K], T is the temperature [K] and S_h is the heat source term [W/m^3], and H is the specific energy [J/kg], which can be calculated using eq. 1.10:

$$H = \frac{\alpha_l \rho_l H_l + \alpha_v \rho_v H_v}{\alpha_l \rho_l + \alpha_v \rho_v} \qquad (eq. 1.10)$$

Then, the Continuous Force Model (CFM) is introduced to model the surface tension like a pressure drop multiplied by a surface. It is a method developed in 1992 by Brackbill et al. used for modeling the surface tension effect on fluid motion. "Interfaces between fluids of different properties, or "colors", are represented as transition regions of finite thickness across which some specific variables change continuously. At each point in the transition region, a force density is defined which is proportional to the curvature of the surface of constant color at that point. The continuum method eliminates the need for interface reconstruction, simplifies the calculation of surface tension, enables accurate modeling of two- and three-dimensional fluid flows driven by surface forces, and does not impose any modeling restriction on the number, complexity, or dynamic evolution of fluid interface having surface tension." (Brackbill, Kothe, & Zemach, 1992).

Thanks to the CFM, the surface tension is treated as a volume force (F_V) in the momentum equation, and it can be written according to the eq. 1.11:

$$F_V = \frac{\sigma(\alpha_l \rho_l \kappa_v \nabla \alpha_v + \alpha_v \rho_v \kappa_l \nabla \alpha_l)}{0.5(\rho_l + rho_v)} \qquad (eq. 1.11)$$

Where $\kappa_l = \frac{\Delta \alpha_l}{\nabla \alpha_l}, \kappa_v = \frac{\Delta \alpha_v}{\nabla \alpha_v}$.

For this case study, liquid water is the heat transfer fluid. Inside the tube, single-phase forced-convection is the dominant heat transfer mechanism, meanwhile outside the tube pool boiling is the considered heat transfer mechanism. In that case, the Grashof (Gr) number is used to evaluate the flow-regime. Gr is defined in eq. 1.12:

$$Gr = \frac{g\beta(T_s - T_\infty)D^3}{v^2} \qquad (eq. 1.12)$$

Where β is the coefficient of thermal expansion [1/K], T_s and T_∞ are respectively the surface and the bulk temperature, D is the characteristic length [m] and v is the kinematic viscosity [m^2/s].

The transition from laminar to turbulent flow occurs for $10^9 < Gr < 10^{10}$ considering natural convection on vertical tubes. In the considered study, the boundary layer is assumed to be turbulent ($1.05\times10^{10} < Gr < 2.38\times10^{10}$), therefore the κ-ε model is adopted (good performances for rotating flow, flow separation and secondary flow).

Mass and energy transfer is defined in eq. 1.12. It is an important parameter in the process of phase transition. knowing that the volumetric mass terms for liquid and vapor, S_l and S_v, can be obtained by the temperature field or boundary condition, the following relationship between the volumetric mass source and the heat source term is shown in eq. 1.13:

$$S = \frac{S_h}{h_{fg}} \qquad (eq.\,1.13)$$

Where h_{fg} is the latent heat [J/kg].

The mass flow rate at the liquid-vapor interface (eq. 1.14) is based on Hertz-Kundsen equation (Schrage, 1953):

$$|S''| = \phi \sqrt{\frac{M}{2\pi R}} \left(\frac{p_v}{\sqrt{T_v}} - \frac{p_{sat}(T_l)}{\sqrt{T_l}} \right) \qquad (eq.\,1.14)$$

Where M is the molecular weight of vapor [g/mol], R is the universal gas constant (8.314 J/mol/K), φ is a correction factor.

In the saturation conditions, the relation between pressure and temperature can be provided by the Clausius-Clapeyron equation (Knudsen, 1934):

$$\frac{dp}{dT} = \frac{h_{fg}}{T\left(\frac{1}{\rho_v} - \frac{1}{\rho_l}\right)} \qquad (eq.\,1.15)$$

Moving into a discrete condition, eq. 1.15 can be rewritten as the eq. 1.16:

$$p - p_{sat} = \frac{h_{fg}}{T\left(\frac{1}{\rho_v} - \frac{1}{\rho_l}\right)} (T - T_{sat}) \qquad (eq.\,1.16)$$

So that it is possible to substitute eq. 1.16 in eq. 1.14 (Hertz-Kundsner equation):

$$|S''| = \phi \sqrt{\frac{M}{2\pi R T_{sat}}} \frac{h_{fg}}{T\left(\frac{1}{\rho_v} - \frac{1}{\rho_l}\right)} \frac{(T - T_{sat})}{T_{sat}} \qquad (eq.\,1.17)$$

In this way, the liquid and vapor source term can be obtained and can be used in eq. 1.4 and in eq. 1.5. Assuming the evaporation coefficient equal one (liquid crossing the interface completely evaporates and vapor crossing the interface complety condenses),vapor and liquid source term can be written respectively as shown in eq. 1.18 and eq. 1.19.

$$S_v = \frac{r_l \alpha_l \rho_l (T_l - T_{sat})}{T_{sat}}, \qquad T_l > T_{sat} \qquad (eq.\,1.18)$$

$$S_l = \frac{r_v \alpha_v \rho_v (T_l - T_{sat})}{T_{sat}}, \qquad T_l \leq T_{sat} \qquad (eq. 1.19)$$

Where *r* is an empirical coefficient called intensity factor and it is set as 0.1.

The considered system is the PRHR HX applied in an AP1000 PWR. The heat exchanger is characterized by a bundle of 689 C-shape tubes. Outer tubes of the bundle are characterized by a more efficient pool boiling heat transfer. In order to obtain conservative results, a tube located in the inner region of the bundle is considered for the analysis, see Fig. 1.35. Taking advantage of the symmetry, only a 1/4 of the computational domain is taken into account.

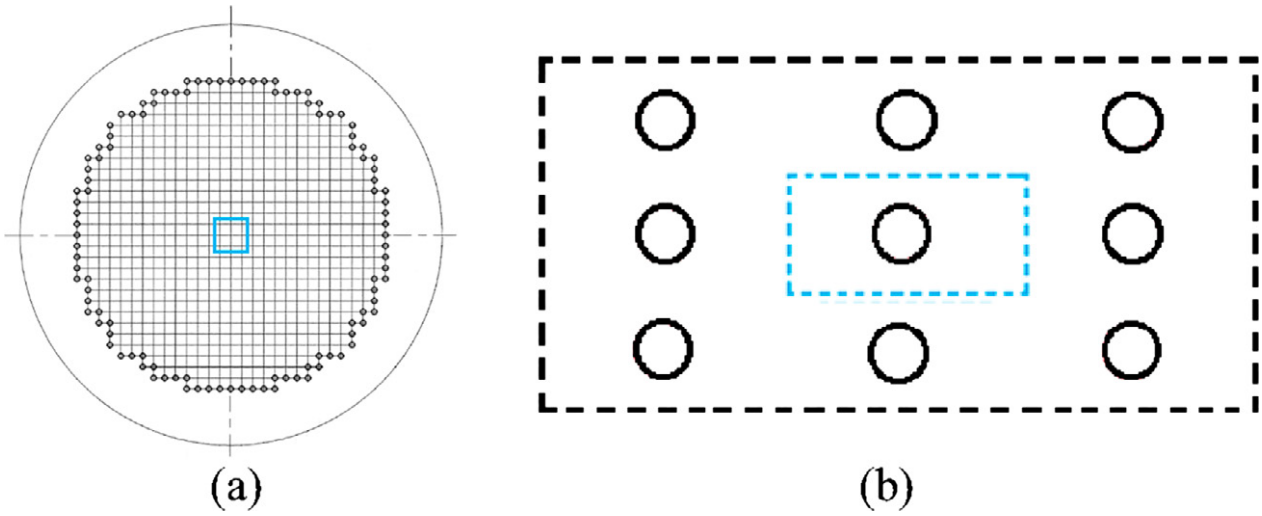

Fig. 1.35. (a) Domain of the vertical section of the tube, (b) the computational region (Tian, Zhang, Wang, Cui, & Cheng, 2017).

The outer diameter of the tube is equal to 19.05 mm. The thickness of tube is equal to 1.65 mm. The computational region is set 1*D*×2*D*. The tube's length is equal to 270*D*, and the water level of the pool is 320*D*. Boundary conditions are listed in the Table 1.6. Numbers in the tables refer to Fig.1.36:

Table 1.6. Boundary conditions (Tian, Zhang, Wang, Cui, & Cheng, 2017).

No.	Location	Boundary type
1	Tube inlet	Free stream velocity
2	Tube outlet	Pressure-outlet
3	Tube wall	Coupled
4	Pool bottom	Wall
5	Pool sides	Symmetry
6	Pool outlet	Pressure-outlet

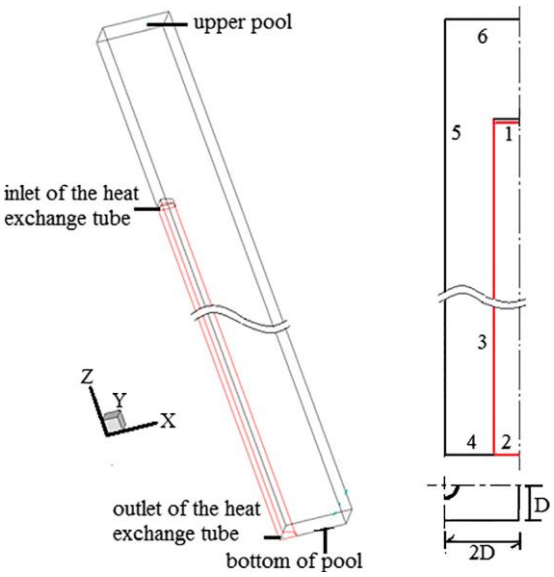

Fig. 1.36. Numerical model (Tian, Zhang, Wang, Cui, & Cheng, 2017)

The mesh (hexahedral shape) is obtained using GAMBIT. The mesh is finer near wall region, were the gradients of the considered variables are high. Then, grid independence tests are performed. A total number of elements equal to 7,205,488 is chosen.

For the validation of the numerical model, two different conditions in the nucleate boiling regime are considered. Different inlet temperature are taken into account: T_1 (395.15 K) and T_2 (420.15 K). The corresponding difference of temperature between the tube's outer surface and the pool water saturation temperature (eq. 1.20).

$$\Delta T = T_{wall} - T_{sat} \qquad (eq.\,1.20)$$

In this case, the corresponding difference of temperature are respectively $10 < \Delta T_1 < 15$ K and $20 < \Delta T_2 < 30$ K. Results obtained by numerical simulations are compared with one of the most widely used nucleate pool boiling correlation (eq. 1.21, eq. 1.22, eq. 1.23):

- Rohsenow correlation (Rohsenow, 1951):

$$q" = \mu_l h_{fg} \sqrt{\frac{g(\rho_l - \rho_v)}{\sigma}} \left(\frac{C_p (T_s - T_{sat})}{C_{sf} h_{fg} Pr_l^s} \right)^3 \qquad (eq.\,1.21)$$

  Where $q"$ is the heat flux [W/m^2], C_{sf} is a coefficient depending on the selected fluid and surface material. For the combination of water and stainless steel (mechanically polished) this coefficient is 0.013.

- Corletti et al. correlation (Corletti, Hochreiter, & Squarer, 1989):

  Where the same previous correlation is proposed, but the coefficient C_{sf} is equal to 0.034 (obtained from Westinghouse's PRHR test facility).

- Kang correlation (Kang, 1998):

$$q" = \frac{0.019\varepsilon^{0.570}\Delta T^{4.676}}{D^{1.238}L^{0.072}} \qquad (eq.1.22)$$

  Where ε is the surface's roughness. This correlation comes out from an experimental study performed on vertical tubes immerged in a water tank (0.79×0.86 m cross section and 1 m height). Tube were simulated by electrically heated rod.

- Parlatan-Rohatgi correlation (Parlatan & Rohatgi, 1997):

$$q" = 52.4\Delta T^{3.058} \qquad (eq.1.23)$$

  That can be applied in the superheat interval $6 \leq \Delta T \leq 22$ K. The tested tube length is 2m.

Results are shown in Fig. 1.37.

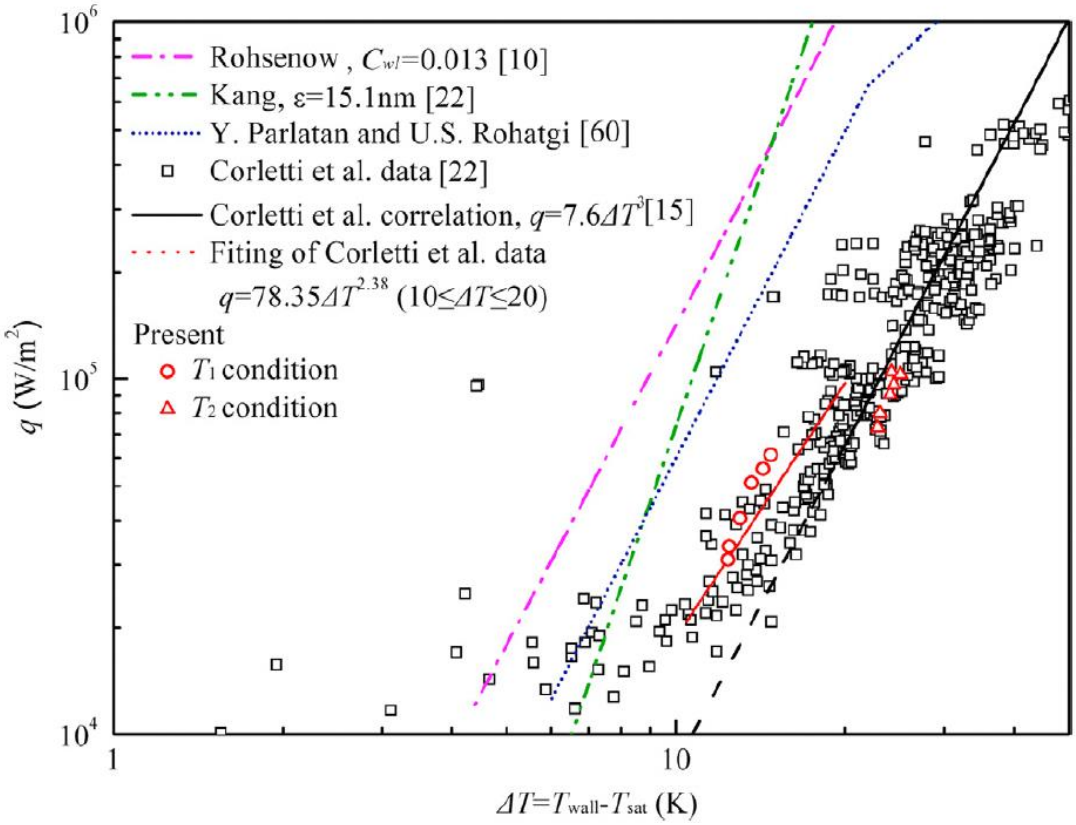

Fig. 1.37. Heat flux as a function of the excess of temperature for all the considered correlation (Tian, Zhang, Wang, Cui, & Cheng, 2017)

There is a significant difference between the results predicted by Rohsenow, Kang and Parlatan-Rohatgi. One of the main reason is that the nucleate boiling surface affects boiling transfer (roughness, dimensions, active sites of nucleation), so different experimental conditions lead to different results.

Another important aspect is that predictions provided by these empirical correlations are greater than the results obtained by correlation and PRHR HX tests performed by Corletti et al. previously mentioned. One of the reasons can be the different tube geometries since all the other correlations are extrapolated by experimental studies performed on shorter tubes with bigger pitches. Comparing Corletti et al. experimental data with Corletti et al. correlation, it is possible to see that correlation provides a comparable results with the experimental data only in the range of $20 < \Delta T < 40$ K. In addition, within the range of ΔT_2, numerical results and experimental data provide almost the same result. For this range of temperature, a new correlation can be extrapolated (eq. 1.24):

$$q'' = 7.6\Delta T^3 \quad (20 < \Delta T \leq 30\ K) \qquad (eq.\ 1.24)$$

For T_1 conditions, corresponding to a $10 < \Delta T_1 < 20$ K, the numerical simulation predicts the experimental data published by Corletti et al. Based on these experimental data, another correlation (eq. 1.25) can be extrapolated for this range of superheat temperature:

$$q" = 78.35\Delta T^{2.38} \ (10 \leq \Delta T \leq 20\ K) \qquad (eq.\ 1.25)$$

Tian et al. validated the new correlations (eq. 1.24 and eq. 1.24) showing a good agreement with experimental data collected by Corletti et al. and deviations between empirical correlations and numerical simulation's results are shown in Table 1.7.

Table 1.7. Numerical results compared with Corletti et al. correlation. (Tian, Zhang, Wang, Cui, & Cheng, 2017)

Conditions	Numerical results	Correlations based on the Corletti et al. data	Correlations results	Deviation (%)
T_1	31,054.7	$q = 78.35\Delta T^{2.38}$	31,228.1	0.5
	33,812.5	$10 \leq \Delta T \leq 20$	31,538.5	7.2
	40,560.1		35,014.4	15.8
	52,023.3		40,207.7	29.4
	56,900.4		44,516.2	27.8
	62,250.2		48,293.8	28.9
T_2	72,922.6	$q = 7.6\Delta T^3$	89,077.8	18.1
	79,911.1		91,469.2	12.6
	90,516.7		104,062.4	13.0
	96,220. 1		110,403.5	12.8
	104,738.9		107,710.9	2.8
	102,887.1		120,044.6	14.3

From the physical fields analysis, the following parameter of the water pool are studied: flow field, temperature field and phase distribution for the vertical section of a tube placed in the intermediate region of bundle. Different axial location along the tube are considered. Physical parameter fields along the tube length present consistent differences. Results are shown in Fig. 1.38.

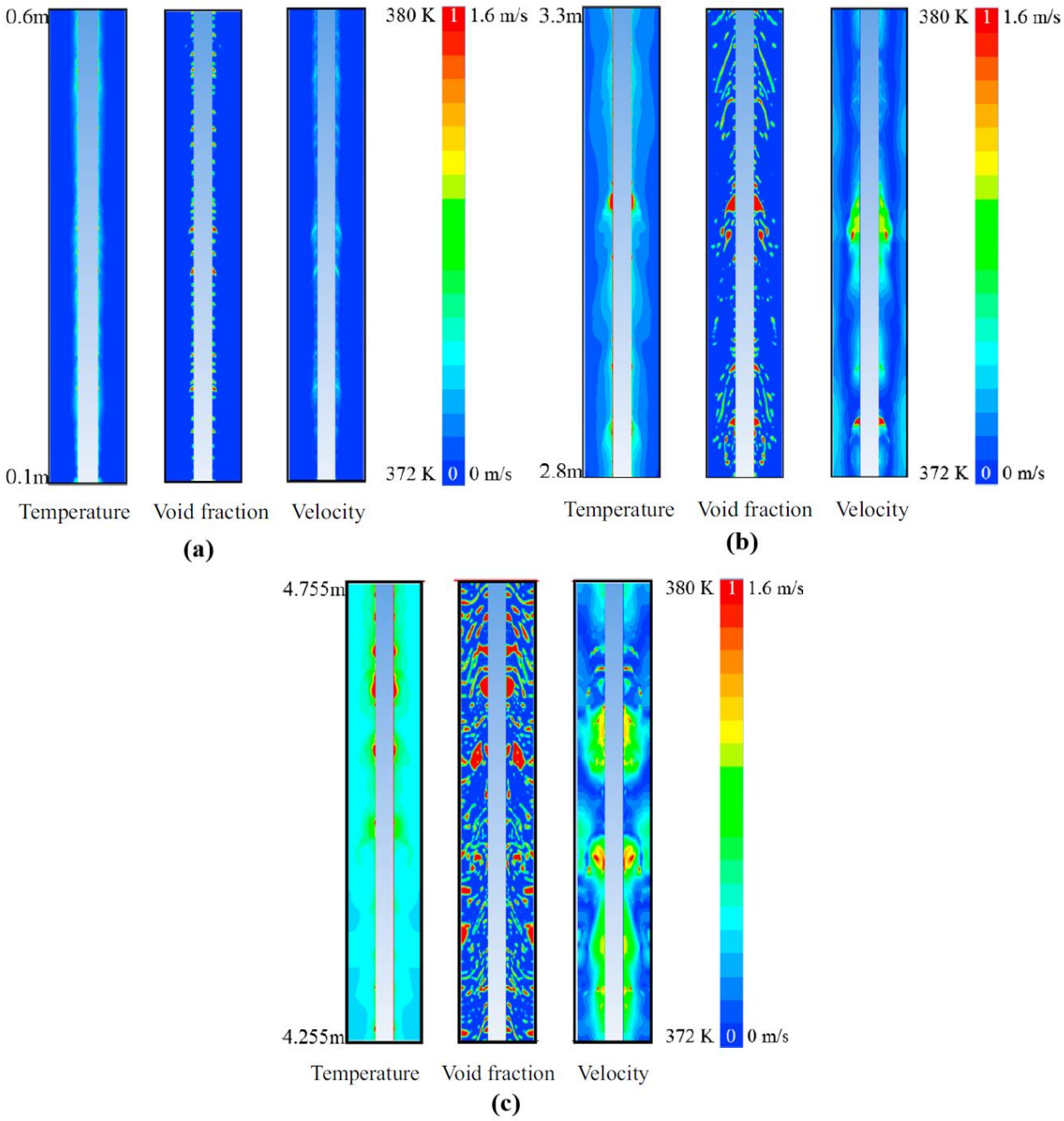

Fig. 1.38. Physical fields at (a) lower part, (b) middle part, (c) upper part of the vertical tube in the longitudinal direction (Tian, Zhang, Wang, Cui, & Cheng, 2017)

Fig. 1.38 (a) shows temperature, velocity and void fraction fields in the bottom of the vertical section of the tube. From the void fraction profile, the formation and growing of bubbles on the tube surface can be noticed. Pool temperature is obviously higher next to the tube and it is approaching to the saturation value, meanwhile bulk temperature is still below the saturation point. As a matter of fact, void fraction is non zero on the surface, but it is mainly a local effect. Bubbles

grow on the surface, but if they detach quickly condense because of the subcooled water that surrounds them.

In the middle region, Fig. 1.38 (b), bubbles coalescence and collapse but differently from what happens in lower regions, many bubbles are capable to reach the main stream. The resulting of: tension (acting perpendicularly to the wall), buoyancy and tangential force of the flow field produces bubbles elongation. Higher mixing and agitation can be detected also by the velocity field.

In the upper region, Fig. 1.38 (c), pool water is at saturation conditions. The bubbly flow significantly affects the velocity field, which is more chaotic due to the mixing.

As regards the primary fluid, Fig. 1.39 shows the temperature profile of hot liquid, inner and outer wall respect to the length of the vertical tube section (L), starting from the bottom of the pipe. Also the radial temperature distribution is shown for two different heights: at L=1 m and at L=5 m.

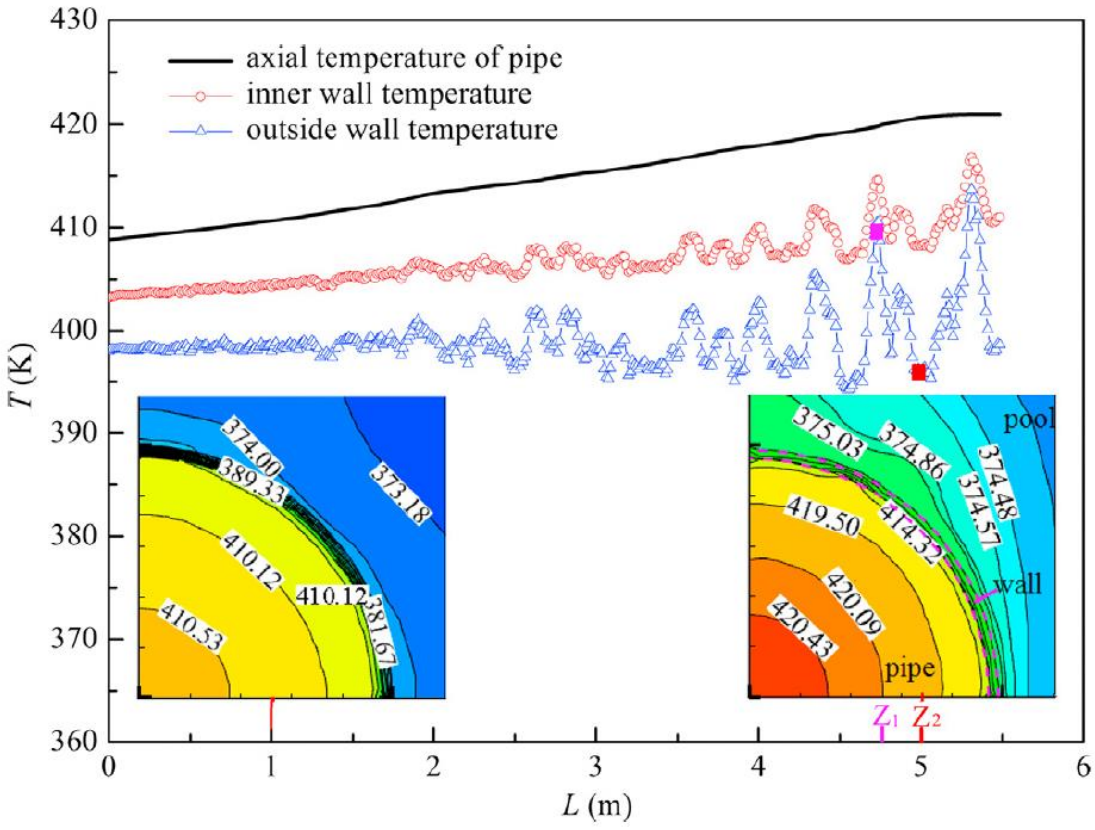

Fig. 1.39. Axial, inner wall and outer wall temperature distribution in the vertical section of the tube (Tian, Zhang, Wang, Cui, & Cheng, 2017).

Moving upward, the primary fluid temperature profile increases gradually, also inner and outer tube surface temperature increase. In the upper half of the tube's vertical section, strong fluctuations on the inner and outer wall temperature profile can be detected. In particular there's a peak of

temperature occurring at Z_1 (4.75 m) and a valley occurring at Z_2 (5.00 m). This behavior is due to bubble formation, coalescence and detachment, and can be easily view in Fig. 1.41, where void fraction is showed at axial positions Z_1 and Z_2 (moving from the blue to the red, void fraction increases).

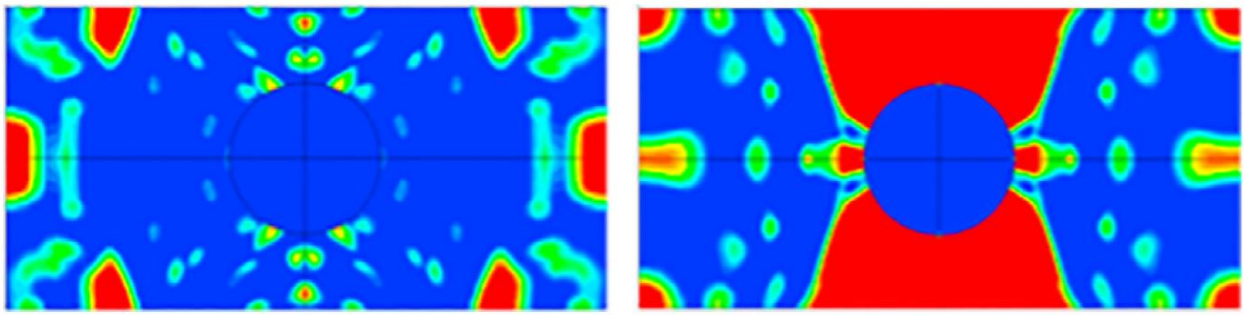

Fig. 1.40. Void fraction and velocity field at (a) Z_1 and (b) Z_2.(Tian, Zhang, Wang, Cui, & Cheng, 2017).

When bubbles detach from the surface (Fig. 1.41 (a)), fresh subcooled liquid can rewet the wall and the heat transfer coefficient becomes lower because of the single-phase heat exchange. Then, liquid can evaporate (Fig. 1.41(b)) and the bubble nucleation improves the heat transfer, resulting in a relatively low thermal resistance. As a matter of fact, the heat transfer coefficients at Z_1 and Z_2 are respectively equal to 1514.9 W/m^2/K and 5750.6 W/m^2/K.

In order to evaluate the time-dependent behavior of the heat flux, the tube length is split into six sections and in each section the local heat flux is evaluated. Bottom section (section 1) starts at 0.5 m, all the other sections' height is equal to 1 m. Results are shown in Fig. 1.42 for a very small time interval (from 2.5 up to 3.2 s). In the lower half of the vertical tube section (sections from 1 to 3) the heat flux is almost steady. In the upper half of the tube (sections from 4 to 6) the heat flux profiles show remarkable fluctuations because of the dominant boiling phenomena. Time-average heat fluxes on the outer tube's surface increase along the tube. They are 5.53x10^4, 6.12 x10^4, 7.27 x10^4, 9.08 x10^4, 9.62 x10^4 and 10.12 x10^4 W/m^2 respectively from the bottom section to the top section. Can be noted that the heat flux of section five is higher than the one at section six when t=3.2 s, probably because of the presence of bubbles.

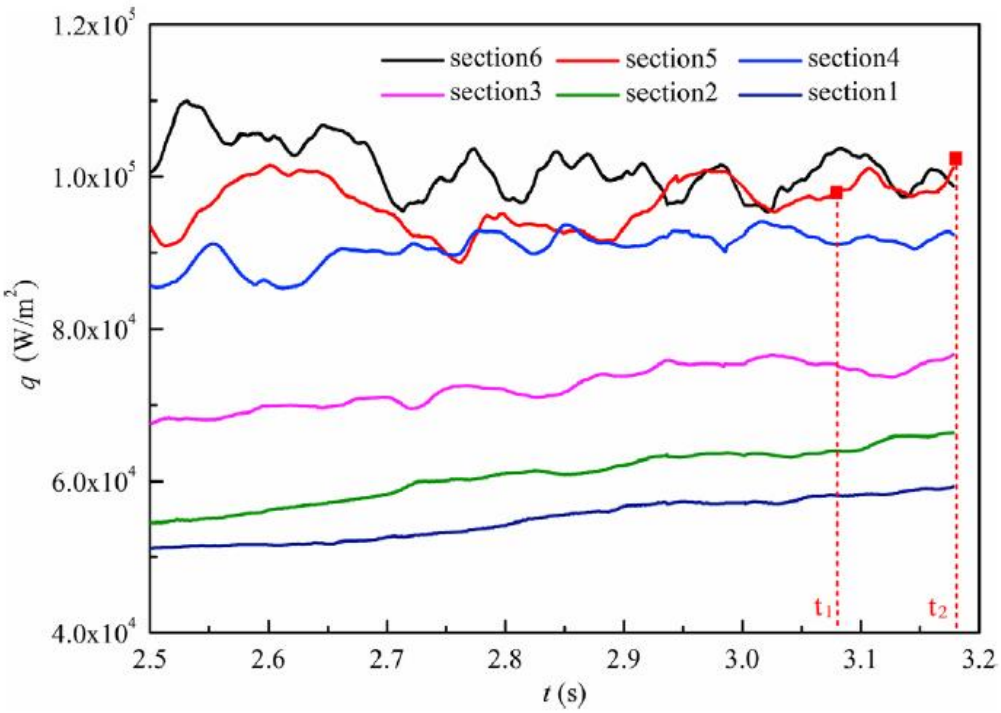

Fig. 1.41. Time dependent heat flux for different sections of the tube (Tian, Zhang, Wang, Cui, & Cheng, 2017).

Concluding, the numerical model describing pool boiling is validated by empirical correlations and by experimental data. Results show the effect of tube length on nucleate pool boiling heat transfer mechanism, in particular, for large-scale vertical heat transfer tubes, the predicted heat power removed is lower because of the bubble coalescence, resulting in bigger vapor slugs. When larger vapor slug is formed on the outer wall surface, the number of activation sites becomes lower, so nucleation heat transfer mechanism deteriorates. Anyway, to study the effect of tube's height and high heat flux on the pool boiling, experimental studies and numerical simulations need to be performed.

Another interesting numerical investigation performed on a scaled PRHR HX immersed in a IRWST is the one discussed by Tao et al. (2018). The experimental apparatus was described in section 1.2.1. The schematic of PRHR test facility is shown in Fig. 1.13 and the main operating parameters are summarized in Table 1.2. The goal of this numerical investigation is to provide a hot primary fluid temperature profile and an outer wall temperature profile. Furthermore, these temperatures are used to compute the local heat flux and the heat transfer coefficient, in order to characterize the different stages of the heat transfer mechanism occurring during the experimental procedure.

At first, the discretization of a heat transfer tube is provided, as shown in Fig. 1.42. The pipe A is discretized into *n* cells in the longitudinal direction.

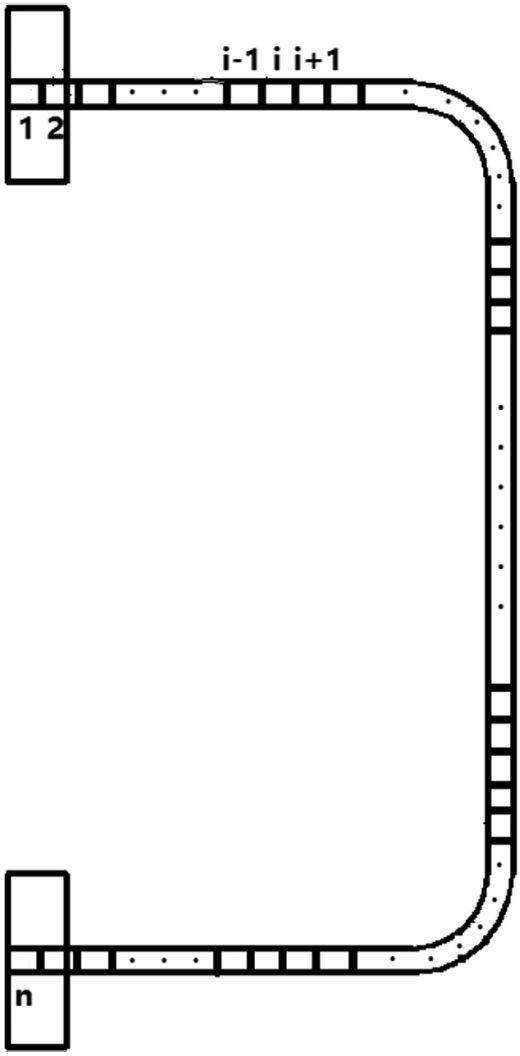

Fig. 1.42 Heat transfer tube discretization (Tao, Gu, Xiong, Jiang, & Xie, 2018).

For the calculations a steady state is assumed. The algorithm adopted is shown in Fig. 1.44. It is based on empirical correlations to describe the heat transfer mechanism occurring between the outer surface of the wall and the IRWST water.

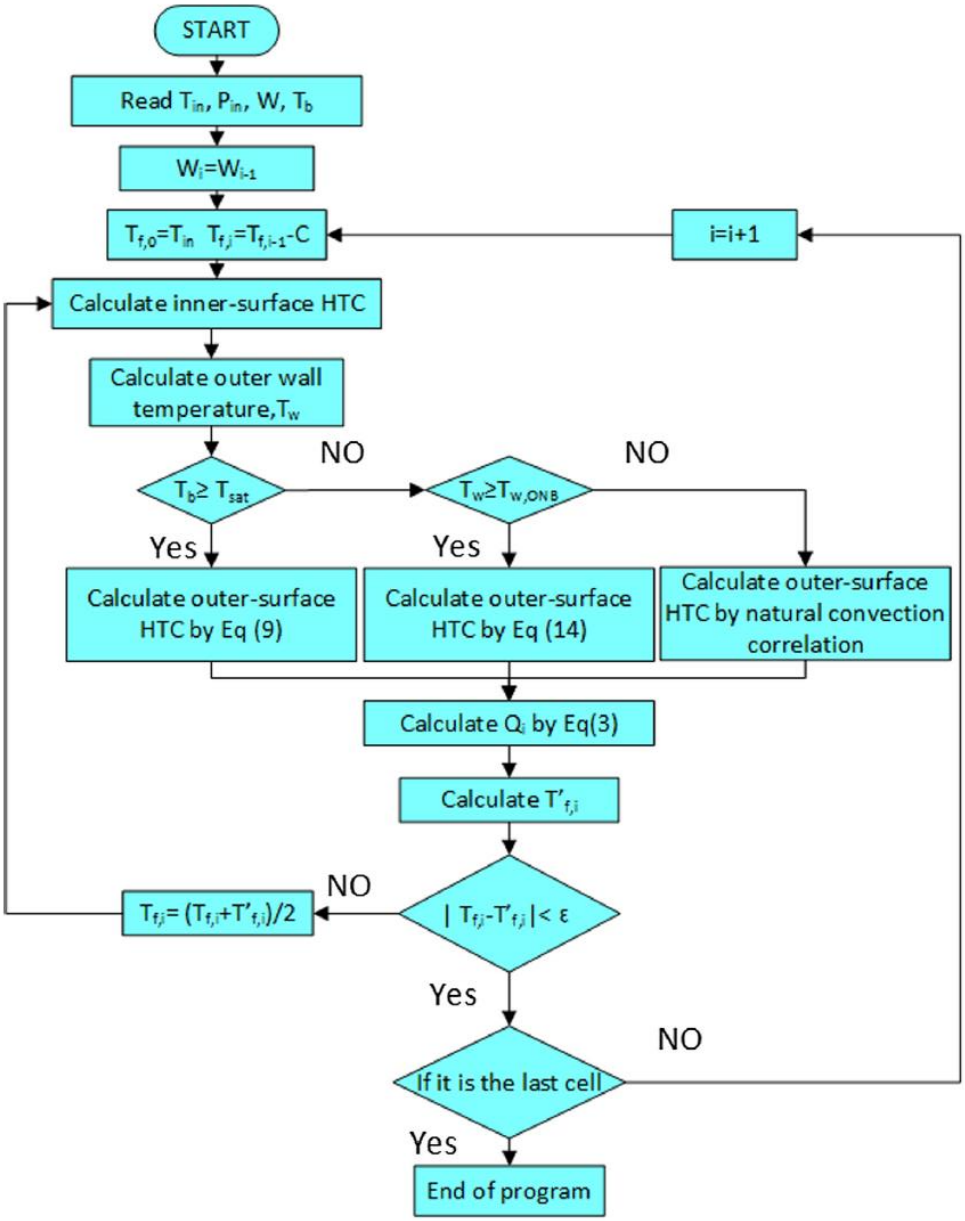

Fig. 1.43. Flowchart of the solution algorithm. Eq(9) refers to Rohsenow correlation, Eq(14) refers to Bergles-Rohsenow correlation. (Tao, Gu, Xiong, Jiang, & Xie, 2018).

The thermal power released from the *i-th* cell to the tank is calculated by eq. 1.26 (steady-state 1D equation of heat transmission):

$$Q_i = \frac{\pi L_i}{\frac{1}{d_1\alpha_1} + \frac{1}{2k_w}\log\left(\frac{d_2}{d_1}\right) + \frac{1}{d_2\alpha_2}}\left(T_{f,i} - T_{b,i}\right) \qquad (eq.\,1.26)$$

With: L_i the length of the *i-th* cell, d_1 and d_2 the inner and outer tube diameter, α_1 and α_2 the inner and outer heat transfer coefficient of the tube surface, k_w the thermal conductivity of the wall (assumed constant), $T_{f,i}$ and $T_{b,i}$ the fluid temperature in the tube and the bulk temperature (last one obtained by experiments) of the *i-th* cell.

The heat transfer Q_i is also related to the temperature decay along the tube. According to the steady-state 1D energy balance equation, it can be evaluated as written in eq. 1.27:

$$Q_i = WC_p\left(T_{f,i-1} - T_{f,i}\right) \qquad (eq.\,1.27)$$

Where: W is the mass flow (obtained by experimental measurements).

As regards the heat transfer coefficient of the inner and outer surface of the tube, different correlations are used and compared. In particular, for the inner side, Taler correlation, Gnielinski correlation and Dittus-Boelter correlation are employed. From numerical analysis, the difference on heat transfer coefficient resulted smaller than 5% and on the heat transfer rate smaller than 1%. Since Dittus-Boelter is the simplest one, it is used in the following calculations and it is reported in eq. 1.28 (Incropera, Dewitt, Bergman, & Lavine, 2011):

$$Nu = \frac{\alpha_1 d_1}{k_f} = 0.023 Re^{0.8} Pr^{0.3} \qquad (eq.\,1.28)$$

Where k_f is the fluid thermal conductivity, Re is the Reynolds number and Pr is the Prandtl number.

The heat transfer mode on the outer surface is more complex. It could be saturated boiling, subcooled boiling or natural convection. When the bulk water inside the tank reaches the saturation condition, the heat transfer mode on the outer surface is considered to be saturated boiling. In this case the Rohsenow correlation, shown in eq. 1.12, is employed to calculate the heat transfer coefficient (Rohsenow, 1951).

The water saturation temperature at different heights of the tank can be evaluated using the corresponding pressure calculated using eq. 1.29:

$$p = p_0 + \rho g H \qquad (eq.\,1.29)$$

Where p_0 is the pressure at the top of the tank, ρ is the density of the water, and H is the distance from the free surface of the water pool.

When outer wall temperature reaches the value of onset boiling, boiling phenomena are assumed to occur, otherwise, natural convection is the heat transfer mechanism at that point. The temperature of onset boiling on the outer surface of the tube can be evaluated using the Bergles-Rohsenow correlation (Bergles & Rohsenow, 1694):

$$T_{w,ONB} = T_{sat} + 0.556\left(\frac{556.3q''}{p^{1.156}}\right)^{0.3538p^{0.0234}} \quad (eq.\,1.30)$$

Where p is the pressure [Pa].

When the wall temperature is higher than the value obtained by eq. 1.30, and the bulk temperature in the IRWST is lower than the saturation value (depending on the pressure obtained by eq. 1.29), the heat transfer mechanism between pool water and the outer surface of the heating pipe is the subcooled boiling. On the other hand, if the bulk temperature reaches the saturation conditions, saturated boiling occurs.

For the single-phase natural convection, two different correlations can be used, according to the tube's orientation: horizontal or vertical. Churchill and Chu provided different correlations for each configuration. In particular, single phase free convection along the lower horizontal section is evaluated by eq. 1.31 (Churchill & Chu, 1975):

$$Nu = \left(0.6 + 0.387\left(\frac{Ra}{\left(1+\left(\frac{0.559}{Pr}\right)^{\frac{9}{16}}\right)^{\frac{16}{9}}}\right)^{\frac{1}{6}}\right)^{2} \quad (eq.\,1.31)$$

It can be used for a wide range of Rayleigh (Ra), and the outer diameter is used as characteristic length. Ra is defined in eq. 1.33:

$$Ra = Gr * \mathrm{Pr} \quad (eq.\,1.32)$$

Where Gr is the Grashof number was defined in eq. 1.12

Where x is the characteristic length, g is the gravity acceleration, β is the thermal expansion coefficient [1/K], μ is the dynamic viscosity [Pa s] and $\rho$is the liquid density [kg/m^3]. Pr is the Prandtl number.

The other Churchill and Chu correlation (Churchill & Chu, 1975) that is used for natural convection along the vertical section of the test pipe is shown in eq. 1.33:

$$Nu = \left(0.825 + 0.387 \left(\frac{Ra^{\frac{1}{6}}}{\left(1 + \left(\frac{0.492}{Pr} \right)^{\frac{9}{16}} \right)^{\frac{8}{27}}} \right) \right)^2 \qquad (eq. 1.33)$$

In that case the characteristic length becomes the distance from the lower horizonal section of the heat exchanger.

As regards bended sections, no correlations are available, so the heat transfer coefficient is obtained by interpolating eq. 1.32 and eq. 1.35.

For subcooled boiling, Bergles and Rohsenow suggested the interpolation of boiling and convection heat flux, as reported in eq. 1.34 (Bergles & Rohsenow, 1694):

$$q = q_{nc} \sqrt{1 + \left(\frac{q_{nb}}{q_{nc}} \left(1 - \frac{q_i}{q_{nc}} \right) \right)^2} \qquad (eq. 1.34)$$

Where q is the heat flux, q_{nc} is the single-phase natural convection heat flux and q_{nb} is the nucleate boiling heat flux. The heat flux q_i is obtained as the product between the wall superheat of the boiling onset and the heat transfer coefficient obtained Churchill and Chu correlations.

Numerical results are compared with the experimental results, previously discussed in section 1.2.1. Adopting this theoretical model, a good prediction of the local heat transfer along the tube is confirmed. The discrepancy between experimental and numerical data is lower than 4%, as shown in Fig. 1.17.

A different heat transfer model was discussed by Ganguli et al. (2010) in order to describe the heat transfer process of a single-tube pool heat exchanger. The system (Fig. 1.12) was discussed in section 1.2.1. In order to provide a mathematical model capable to describe such a complicated system, saturation temperature and latent heat can be assumed constant. As regards thermophysical properties of water and steam, they are evaluated at saturation temperature. The model is based on the repartition of the heat flux exchanged between the outer tube surface and the pool, into three different components, as shown in eq. 1.35:

$$q"_{tot} = q"_F + q"_Q + q"_E \qquad (eq. 1.35)$$

Where $q"_F$, $q"_Q$ and $q"_E$ are respectively the heat flux due to single-phase convection, quenching and evaporation.

Single phase natural convection is calculated using eq. 1.36:

$$q_F" = 0.14\,\rho_L c_p \left[\frac{\beta g \Delta T^4 \alpha^2}{\nu}\right]^{\frac{1}{3}} \qquad (eq.\,1.36)$$

Where ρ_L is the liquid density [kg/m^3], c_p is the liquid specific heat [J/kg/K], β is the thermal expansion coefficient [1/K], α is the thermal diffusivity [m^2/s], ν is the kinematic viscosity [m^2/s] and ΔT is the temperature difference between the heated wall and the bulk temperature.

The evaporation heat flux is the flux required to produce bubbles on the heated surface and it is obtained by eq. 1.37

$$q_E" = \dot{m}_w \lambda \qquad (eq.\,1.37)$$

Where λ is the latent heat of vaporization, and $\dot{m}_w$ is the periodic release of bubbles by each nucleation site, which can be computed using eq. 1.38:

$$\dot{m}_w = \rho_G \pi \frac{d_w^3}{6} N_A f \qquad (eq.\,1.38)$$

With f is the bubble frequency [Hz], d_w is the bubble departure diameter [mm] and N_A is the nucleation site density, which is obtained by Kurul and Podowki correlation (Kurul & Podowski, 1991):

$$N_A = \left(185 \cdot \Delta T_{sup}\right)^{1.805} \qquad (\text{eq.}\,1.39)$$

$$\Delta T_{sup} = T_{wall} - T_{sat} \qquad (eq.\,1.40)$$

As regards the quenching heat flux, it is the heat flux due to the liquid water that replaces the volume where a bubble used to grow, or the volume occupied by a bubble before than that collapsed. Quenching heat flux can be obtained using eq. 1.41

$$q_Q" = 2\sqrt{\pi\, k\, \rho\, C_p\, f d_b^2}\, N_A\, \Delta T \qquad (eq.\,1.41)$$

Where d_b is the bubble diameter [mm].

Knowing all the component of the heat flux exchanged from the heated pipe to the pool, an energy balance can be performed, in order to evaluate the total amount of energy released to the pool at time *t* (eq. 1.42).

$$E_{tot}(t) = E_F + E_Q + E_E = q_F"A_F t + q_Q"A_Q t + q_E"A_E t \qquad (eq. 1.42)$$

Where A is the heat transfer surface of each one of the heat transfer mechanisms [m^2]. Results are summarized in table 1.8.

Table 1.8. Energy balance in the glass tank (Ganguli, Sathe, Pandit, Joshi, & Vijayan, 2010).

Time	Input energy	Evaporative energy		Quenching energy		Convective energy	
t(s)	$E(J) \times 10^6$	$E_E(J) \times 10^6$		$E_Q(J) \times 10^6$		$E_F(J) \times 10^6$	
-	-	CFD	Experiments	CFD	Experiments	CFD	Experiments
50	6.25	3.24	4.05	0.259	0.323	1.51	1.88
80	10	0.112	0.172	1.54	2.36	6.51	7.46
120	15	1.83	2.37	2.89	3.74	11.6	8.89
160	20	0.018	0.020	5.00	5.61	17.8	14.4
200	25	1.60	1.66	6.68	6.93	24.1	16.4

Input energy was experimentally measured as the product between the condensed mass of water times the latent heat of evaporation. Energy components are evaluated using the same correlations implemented in the numerical model (eq. 1.36, eq. 1.37 and eq. 1.41) but temperatures are detected by thermocouples.

Evaporative heat flux is dominant during the starting phase (until 50 s), and experimental and numerical analysis are comparable. When pool boiling nucleation is reached, the convective heat flux prevails because of the development of turbulence. Also the quenching heat flux becomes higher and higher from 80 s until the end of the experiment, thanks to the increasing bubble production which results in higher water flowrate filling up the area where bubble used to grow. A certain discrepancy between experimental and numerical result as regards quenching heat flux and convective heat flux can be noticed, especially during the last 40 s of the analysis.

For the considered time interval (50-200 s), the major contribution is provided by the energy associated to the convective heat flux (85-90%), meanwhile evaporative and quenching heat flux are less significant (respectively 8-10% and 2-3% of the total energy released to the tank water). This suggests that the most of the energy transfer from the hot tube to the system is due to mixing processes for $0 < t < 200$ s. They are improved by the turbulent flow regime, achieved also by the evaporation of water in contact with the heated channel (evaporative heat flux) and by the replacement of fresh water in the area where bubbles used to grow (quenching heat flux). Furthermore, the energy associated to these heat transfer mechanisms shows a good agreement between experimental data and numerical simulation. Convective energy, on the other hand, is affected by a deviation of ±20%. The reason may be related to the adopted instrumentation (i.e. thermocouples with low response time). Results are also shown in Fig. 1.44.

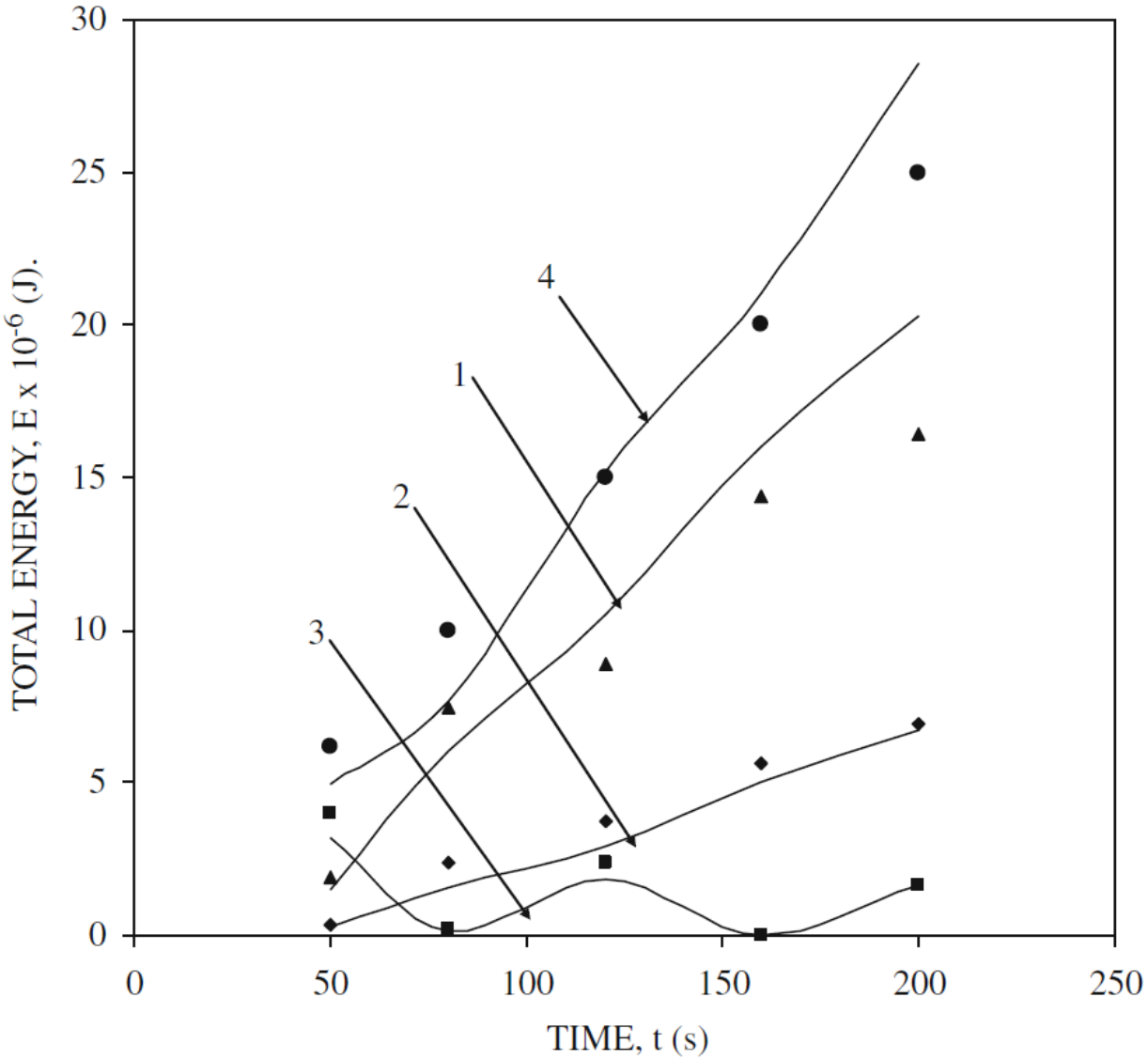

Fig. 1.44. Energy variation respect to time. . CFD — (1) E_F, (2) E_Q , (3) E_E and (4) $E_{tot.}$ Experimental (triangle) E_F, (rhombus) E_Q, (square) E_E and (circle) E_{tot}. (Arijit, et al., 2010)

1.3 CONCLUSIONS ON THE STATE OF ART

As regards the investigation on the heat transfer performance of PRHR HX immerged in the IRWST, adopting a C-shape heating rods bundle, both experimental studies on scaled system and numerical simulations were carried out.
In the first case different techniques were adopted (e.g. PIV, thermocouples) in order to highlight the most important parameter such as the velocity field and the temperature field distribution, showing a certain agreement with computational analysis. Lu, et al., (2016) tried to investigate the evolution of the "thermal interface" during the heat exchange of a 3x4 PRHR HX. Thermal interface's motion has great influence on thermal stratification phenomenon, in particular as regards the mixing of the lower region, which is not involved in the heat transfer for most of the time. Tao, et al., (2018) performed a parametric study in a scaled 6x7 PRHR HX in order to evaluate the effect on the heat exchange of different operating conditions. For increasing mass flowrate and inlet temperature, an increase of the heat transfer coefficient was detected. They also showed the repartition of the heat flux across the vertical and the horizontal sections, highlighting that most of the heat transfer occur in the upper horizontal and in the higher region of the vertical tube. However, the involved phenomena can not be fully investigated in scaled systems because of the influence of geometrical parameter (H/D ratio, pitch between the bundle, number of tubes in the bundle and so on).
From the numerical simulations' point of view, Ge, et al., (2018) simulated the heat transfer between PRHR HX and water in the IRWST. According to the results obtained by the simulation, thermal stratification suppression is reached later than detected in the scaled experiments. This result can be explained because the lower region of the tank seems to contribute earlier to the heat transfer through natural circulation. The radial mixing produces a stronger recirculation far away from the PRHR HX and, consequently, the bottom of the IRWST is involved more easily in the heat exchange, thus temperature gradient is weaker. Also Tian, et al., (2017) numerically investigated the heat transfer characteristic of a single tube, based on the PRHR HX's bundle. Their model was validated by experimental data and empirical correlations, showing that the tube length strongly affects the heat transfer, in particular during the nucleate boiling regime. They also compared different empirical correlations, illustrating remarkable differences between them, depending on the conditions in which tests were performed, i.e. flow regime (subcooled or saturated boiling), range of temperature (subcooling degree, excess of temperature), heat flux (constant or time dependent and its absolute value), mass flowrate, pipe inclination, surface's roughness.

The other category of experimental study can be identified by the single tube heat exchanger. This kind of system can be very useful in order to investigate the heat transfer mechanism during the pool boiling under different conditions. PIV techniques are widely used in this field, but also

thermocouples, of course. They are characterized by a simpler design, if compared to bundle heat exchangers, but can be used to study the process of thermal stratification, the evolution of the thermal interface or the development of the heat transfer mechanisms under particular conditions of interest, since, for single tube heat exchanger, different configuration can be tested (e.g. different tube shape, different kind of confinement).

Tian, et al., (2018) investigated the local heat transfer characteristics of pool boiling on a vertical tube (length and diameter respectively equal to 1500 mm and 20 mm) under two different configurations: unconfined and confined space. The confinement was obtained by a squared glass shell (cross section 80 mm x 80 mm). The heat transfer mechanism in the confined space is convective boiling, as a result of the stronger natural convection flow which enhances the longitudinal heat transfer, in contrast to the radial mixing observed in the pool boiling. The improvement of the longitudinal heat transfer reduces the stagnation of the water in the lower region, reducing the thermal stratification.

Also Ganguli, et al., (2010) performed some experimental measurements on a single-tube heat exchanger, focusing on pool boiling heat transfer. In this case a different approach was followed because also a CFD analysis were performed. The model was validated by experimental measurements, considering the total heat flux divided in three components: single phase natural convection, evaporation and quenching heat flux. The heat transfer mechanism was studied in a relatively small time interval (from 50 s to 200 s after the onset of subcooled boiling). During the heat exchange, the energy transfer was mainly due to the convective heat flux.

From the cited studies, there are some aspects that are quite well understood, and other that need to be further investigated. In particular, during the first phase of the pool boiling heat exchange, the instauration of the single-phase natural circulation can be predicted quite easily. As a matter of fact, it is the simplest heat transfer mechanism and the literature in this field can be very useful to predict the fluid behavior in terms of heat transfer coefficient. Typically Churchill & Chu correlations are used in order to evaluate the Nusselt number during this stage of the heat transfer process. Also the thermal stratification build-up seems to be well known, also because, during the last decades, it was subject of study for systems like solar storage thanks. However, in nuclear industry, the delay (or, even better, the suppression) of thermal stratification is pursued, which represents a more challenging goal. In order to reach this result is fundamental to better understand some issues of the thermofluid-dynamics in pool heat exchangers.

To the present day, one of the most important limits is represented by the dimension of the system (pool and heat exchanger). As a matter of fact, due to the complexity of two-phase heat exchange, the heat transfer mechanism is affected by the system's scale. Higher vertical surfaces involved in the heat exchange implicate higher buoyancy forces. The intensification of buoyancy forces affects positively the heat exchange and the secondary fluid is in general capable to remove an higher heat

flux from the heated pipes. In addition, as the size of the heat exchanger increases, different flow regimes can be observed. One of the reasons that make this kind of heat transfer mechanism so complex is the presence of a set of phenomena involved with the bubble dynamic inside the liquid (e.g. film dynamic, bubble's formation, bubble's detachment, interaction between bubbles and main flow, bubbles collision, sliding and so on) which are phenomena that characterize different phases during the subcooled pool boiling and the saturated pool boiling.

From these considerations, the main uncertainties related to the thermofluid-dynamic in pool heat exchangers seem to be related to the lack of experimental measurements on different space-scale, considering different tube and/or pool geometries or studies focused on some phase of the heat transfer mechanism, in particular two-phase regimes.

As regards the system's size, it is difficult to get proper insight of the boiling over tube in industrial applications because of the expensive industrial scale experiments. As a matter of fact the height of the heat exchanger represents one of the most debated point. However CFD can easily be implemented, with less costs, to investigate local heat transfer characteristics and mechanisms, providing also quantitative information about temperature, phase distribution, flow field and so on and so for. Anyway, numerical models need experimental measurements in order to be validated.

Concerning the geometries involved, different tube shape (e.g. vertical or C-shaped) or different bundle arrangement (different pitches) can lead to different results that need to be further investigated. Furthermore, pool boiling in confined space shows interesting results in terms of improvement of the heat transfer mechanism, "however, the literature of pool boiling on the vertical tube bundles and a vertical tube in confined space is insufficient" (Tian, Chen, Wang, Cui, & Cheng, 2018). Different operating conditions (e.g. different flowrate, heat flux, range of temperature) may also highlight limits of correlations, when they are not sufficient to predict some aspect concerning the heat exchange.

As regards the two-phase heat transfer mechanism, in most of the experimental set-ups described in section 1.2.1 the heat transfer is achieved using electrically heated rods or using subcooled liquid as primary fluid probably for two reasons: they are simpler solutions (in particular the first one) and condensation is assumed to be not relevant and only pool boiling on the wall-pool interface is studied. Actually condensation should be taken into account in further studies in order to investigate a wide range of accidents involving natural circulation safety systems where primary fluid is steam or a two-phase mixture rather than subcooled liquid.

Considering the difficulties related to large scale systems, it is not so easy to study in detail the effect of tube length on pool boiling. On the other hand, the aspects that need to be further analyzed are the pool boiling with vertical tube eventually in confined space, which can help into the

evaluation of the heat transfer in tube bundles (much closer to real industrial applications than the single tube) and the condensation process occurring on the inner side of the tube.

For this purpose, pool boiling heat transfer will be investigated in a experimental system. A small cylindrical tank (inner diameter equal to 592 mm, height equal to 1000 mm) filled y water at atmospheric pressure will be the thermal sink. The heat source, starting from a simpler configuration, will be a single vertical tube in unconfined space. An electrically heated rod will be used during the first experimental phase. Than the heat source will be replaced by dry saturated steam in order to evaluate how the pool boiling changes respect these two configuration, respectively characterized by an imposed heat flux and by an imposed temperature. After the single tube analysis, the effect of confinements can be evaluated, or tube bundle's performances can be studied.

In this section, the description of the heat transfer mechanisms occurring in the experimental system will be addressed. On the pool side, the liquid is heated up and the heat transfer mechanism is the pool boiling. Assuming an imposed temperature configuration of the experimental system, on the inner tube side there is saturated steam that, flowing inside the pipe, undergoes to condensation.

2.1 POOL BOILING

Boiling heat transfer occurs when liquid temperature reaches the saturation temperature corresponding to the liquid pressure. When saturation condition are reached, formation of vapor bubbles occurs. Bubbles can grow and detach from the interface where the heat transfer is occurring. In pool boiling the heat transfer process occurs between the liquid and a hot surface (i.e. a pipe). At the beginning, liquid is stagnant and its motion nearby the heating surface is due to natural convection. As the heat transfer continues, bubbles can nucleate on the surface and liquid motion is also induced by the mixing resulting from bubble growth and detachment. On the other hand, during forced convection boiling, fluid motion is induced externally (by a pressure difference) and by bubbles motions. A further boiling classification can be performed distinguishing subcooled and saturated boiling. Subcooled boiling occurs under thermodynamic instability conditions: far from the heat source, liquid's bulk temperature is below the saturation value. On the contrary, near the heat source the fluid reaches the saturation conditions and bubbles can be formed. When they detach and reach the subcooled liquid they condense. During the saturated boiling, the temperature of the liquid is homogeneous and it is equal to the saturation temperature everywhere. In that case bubbles are formed at the liquid-heat source interface and they can move through the liquid under the effect of buoyancy forces.

Pool boiling is a heat transfer mechanism occurring in presence of a heated surface which is submerged in a large volume of stagnant liquid. Also for pool boiling is possible to distinguish the subcooled pool boiling (if the liquid temperature is below the boiling point) and the saturated pool boiling (if the liquid temperature is at its boiling point. In order to better understand this mechanisms that characterize the saturated pool boiling the boiling curve can be analyzed.

2.1.1 *The boiling curve (imposed heat flux)*

Nukiyama was the first to study pool boiling, in 1934, identifying different regimes throughout the evolution of the heat transfer (Nukiyama, 1934). The experimental apparatus is schematically shown in Fig. 2.1. It was made by a Pyrex tank (15 cm x 15 cm x 40 cm) filled by deionized saturated water at atmospheric pressure. The heat input from the horizontal wire (Q) was determined by measuring the current flow I. The wire temperature was estimated measuring the

potential drop E and knowing how the electrical resistance (R_{el}) changed with temperature. This configuration is called power-control heating, since the wire temperature is a dependent variable of the power setting.

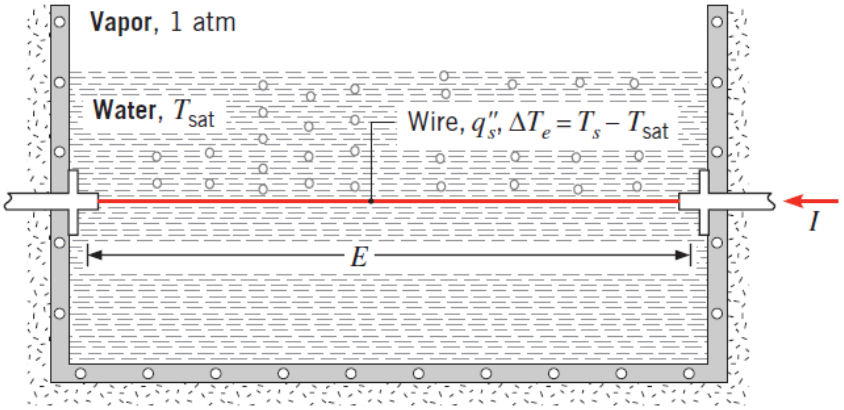

Fig. 2.1. Schematic of the Nukiyama experimental system (power control heating configuration) (Incropera, Dewitt, Bergman, & Lavine, 2011).

The results of the experiment for water at the atmospheric pressure are showed in the so called "boiling curve" Fig. 2.2. The curve is the representation of the surface heat flux against the excess of temperature ΔT_e which is defined in eq. 2.1, as follows:

$$\Delta T_e = T_{wall} - T_{sat} \qquad (eq. 2.1)$$

Looking at the boiling curve, it is possible to see that for excess temperature lower than 5 °C boiling does not occur. The Onset of Nucleate Boiling (ONB) is detected when $\Delta T_e \approx 5$ °C. With further increase in power, the heat flux sharply increased in the nucleate boiling region until it reaches the Critical Heat Flux (CHF). CHF corresponds to the maximum heat flux that can be achieved during nucleate boiling. Beyond this value, an increase of the heat flux produces an impressive increase of the excess of temperature, because of the occurrence of film boiling. On the other hand, reducing the power, the variation of ΔT_e with the heat flux follows the cooling curve, passing through the minimum heat flux, where a further decrease of power causes the excess temperature to drop abruptly. Then the process follows the boiling curve, passing through the nucleate boiling regime (at low heat flux) and through the natural convection regime. The hysteresis effect showed in Fig. 2.2 can be achieved only through a power-control heating. In order to observe the fluctuations of the heat flux during the transition boiling regime, the excess temperature must be the control variable. This kind of arrangement can be obtained, for example, by heating the heat transfer surface with a hot liquid flowing inside a tube. In that case the heat flux can be calculated by measuring the hot liquid temperature variation:

$$q'' = W\ c_p \frac{T_{in} - T_{out}}{A} \qquad (eq.2.2)$$

Where W is the hot fluid mass flowrate, c_p is the hot liquid heat capacity at constant pressure, A is the heat transfer surface and $T_{in} - T_{out}$ is the drop of temperature of the hot fluid between the inlet and the outlet section.

The main characteristics of each regime occurring during pool boiling of water at atmospheric pressure are discussed below.

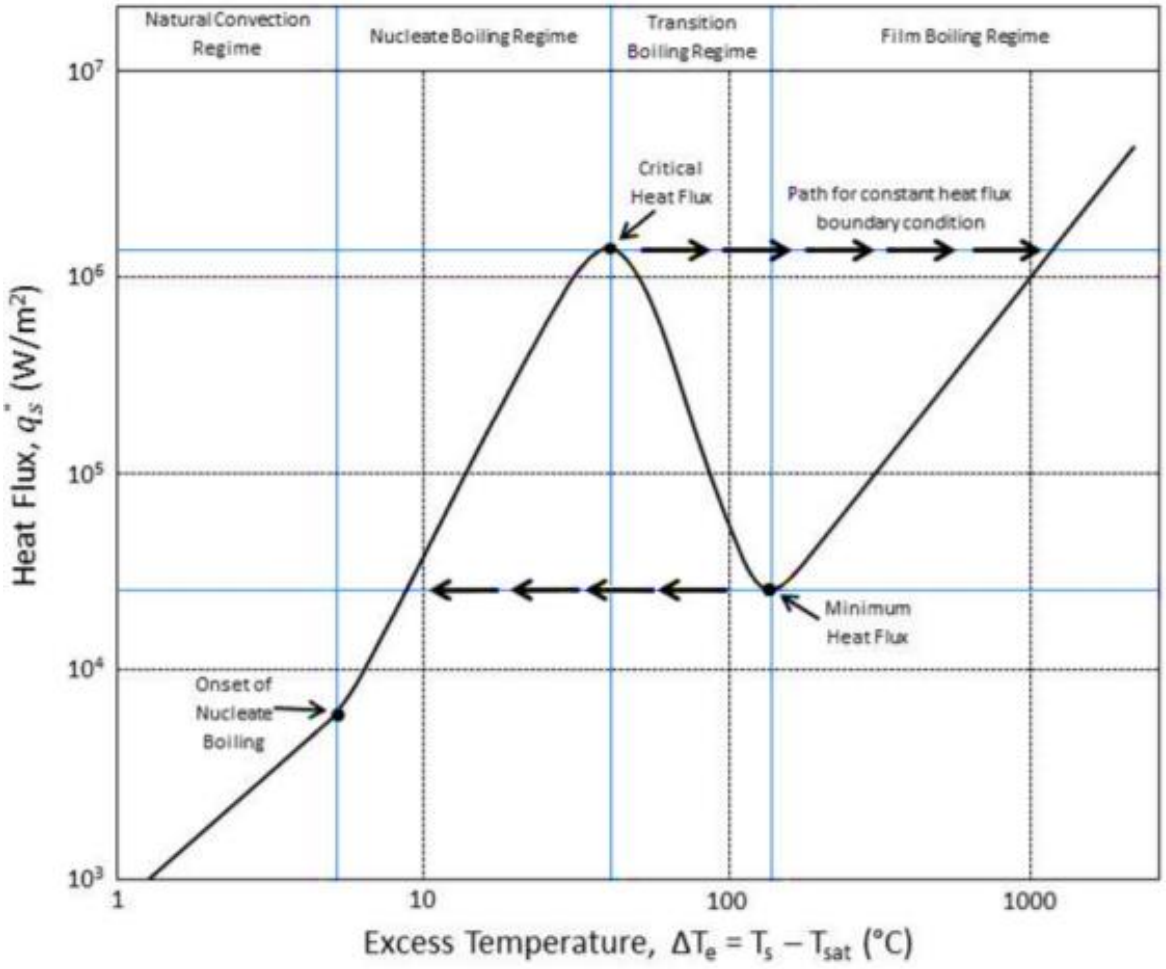

Fig. 2.2. Boiling curve for pool boiling of water at atmospheric pressure (Thompson, 2013).

- Nucleate boiling regime

Nucleate boiling regime's lower and upper limits are respectively ONB and the CHF, which corresponds to $5 \leq \Delta T_e \leq 30$ °C for water at atmospheric pressure. Within this range of temperatures, two different flow regimes can be detected. In the first region, up to $\Delta T_e \approx 10$ °C, bubbles formation

start to occur in few nucleation sites. Some of the bubbles depart from the heated surface, as shown in Fig. 2.3 (a). When bubbles detach from the wall, considerable fluid mixing near the surface is induced. Mixing produces a remarkable increase of the heat transfer coefficient h and the heat flux q_s''. When the excess of temperature becomes higher than 10 °C, the number of active nucleation sites increases, therefore more bubbles grow on the heated surface. This results in bubble coalescence and vapor, escaping as columns or jets, reaches the free surface as slugs of vapor, see Fig. 2.3 (b). In the vicinity of the heated surface, liquid encounters some difficulties to reach the solid surface because the region is densely populated by bubbles. As the excess of temperature increases, the heat flux starts being no more linear in the log-log plot of Fig. 2.2. When $q_s'' = q_{max}''$, the CHF is reached and a considerable amount of vapor is begin formed on the wire's surface. In this condition, fresh liquid can't easily rewet the heating surface, as illustrated in Fig. 2.3 (c). This regime is characterized by high values of heat transfer coefficient. For water at atmospheric pressure, the typical order of magnitude of the heat transfer coefficient is 10^4 W/m^2/K, meanwhile, under the same conditions, CHF's order of magnitude is 10^6 W/m^2.

- Film boiling regime

Film boiling regime starts when the excess of temperature exceeds 120 °C in water at atmospheric pressure, in correspondence of the minimum heat flux. There, the entire surface is covered by a thin layer of vapor and heat transfer from the heat source to the water occurs thanks conductive and radiative heat transfer mechanisms through the layer of vapor. When the surface temperature increases, radiation becomes more and more significant, and the heat flux becomes higher. During the film boiling adopting a power control heating, in order to detect an increase of heat flux, a remarkable excess of temperature is required (more than 1000 °C), but an excessive increase of the surface temperature can results into the melting of the heating rod. Film boiling is illustrated in Fig. 2.3 (e).

- Transition boiling regime

The region corresponding to $30 \leq \Delta T_e \leq 120$ °C is called transition boiling. In this regime, any point of the surface may oscillate between nucleate boiling (most efficient heat transfer mechanism of pool boiling) and film boiling (less efficient heat transfer mechanism of pool boiling). Transition boiling can be observed if the excess of temperature is the control variable. Within the range of temperature of transition boiling, the heat flux is affected by huge fluctuations due to the continuous transition between nucleate boiling and transition boiling. The behavior of the heat flux, illustrated in the boiling curve (Fig. 2.2), is a best-fit of the experimental measurements carried out. As the heating process goes on, for increasing values of the excess temperature, the heating surface is covered by a progressively increasing vapor film. Transition boiling is illustrated in Fig. 2.3 (d). When $\Delta T_e > 120$°C, film boiling occurs.

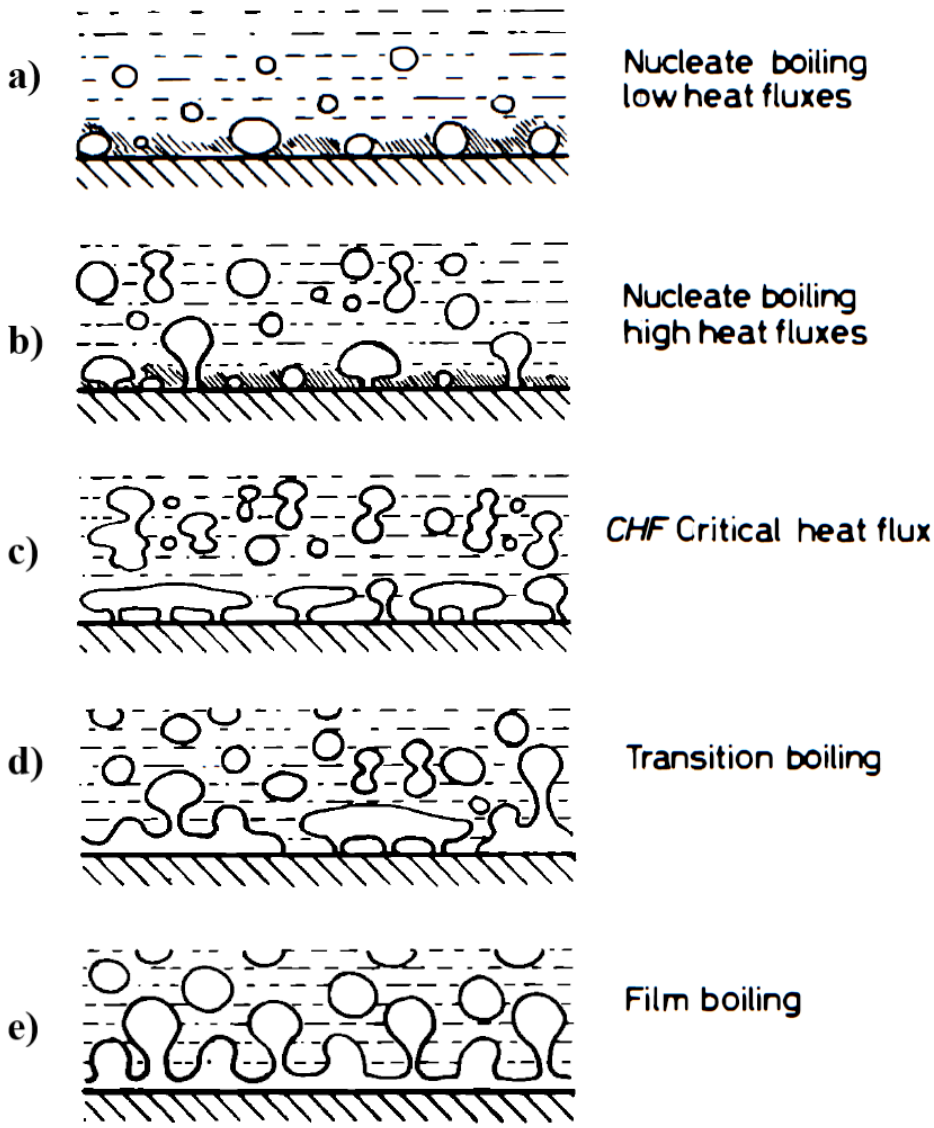

Fig. 2.3. Pool boiling regimes: a schematic representation(Collier & Thome, 1994)

2.1.2 *Pool boiling correlation*

The boiling curve previously described shows that various physical mechanisms characterize the different regimes, for this reason many heat transfer correlations were developed for the boiling process.

- Nucleate pool boiling

In order to evaluate the nucleate pool boiling, the total number of active nucleation sites should be required, as well the bubbles formation frequency from each site. Even though this kind of heat transfer mechanism is widely studied due to its interesting industrial application, there is no

mathematical model capable to describe in detail nucleate pool boiling regime. To the present day one of the most used correlations for the nucleate pool boiling is the one developed by Rohsenow (Rohsenow, 1951), eq. 2.3:

$$q_s'' = \mu_l h_{fg} \left(\frac{g(\rho_l - \rho_v)}{\sigma} \right)^{\frac{1}{2}} \left(\frac{c_{p,l} \Delta T_e}{C_{s,f} h_{fg} Pr_l^n} \right)^3 \qquad (eq. 2.3)$$

Where μ_l is the liquid dynamic viscosity [Pa*s], h_{fg} is the latent heat of evaporation, g is the gravity acceleration [m/s^2], ρ is the density [kg/m^3], σ is the surface tension [N/m], $c_{p,l}$ is the specific heat of liquid at constant pressure [J/kg/K], $Pr_{,l}$ is the Prandtl number of liquid water, ΔT_e is the excess of temperature. All the fluid's properties must be evaluated at the saturation temperature. $C_{s,f}$ and n are coefficients depending on the surface-fluid combination. Some values of these parameters are showed in table 2.1.

Table 2.1 Values of $C_{s,f}$ and n coefficients for some combinations of fluid-surface's material (Incropera, Dewitt, Bergman, & Lavine, 2011)

Surface-Fluid Combination	$C_{s,f}$	n
Water-Copper		
-Scored	0.0068	1.0
-Polished	0.0128	1.0
Water-Stainless steel		
-Chemically etched	0.0133	1.0
-Mechanically polished	0.0132	1.0
-Ground and polished	0.0080	1.0
Water-Brass	0.0060	1.0
Water-nickel	0.006	1.0
n-Pentane-Copper		
-Polished	0.0154	1.7
-Lapped	0.0049	1.7
Benzene-Chromium	0.0101	1.7

There are also other correlation that can be used in order to evaluate the heat transfer coefficient during the nucleate boiling heat transfer. One of them is the Mostinsky correlation, eq. 2.4 (Collier & Thome, 1994):

$$h = A' * F(p) * q_s''^{0.7} \qquad (eq. 2.4)$$

Where *A'* is a constant and *F(p)* is a function of pressure. They are defined respectively in eq. 2.5 and eq. 2.6:

$$A = 0.1011 p_{cr}^{0.69} \qquad (eq. 2.5)$$

$$F(p) = 1.8 * p_r^{0.17} + 4p_r^{1.2} + 10p_r^{10} \qquad (eq. 2.6)$$

This correlation depends only on the exchanged heat flux during the nucleate boiling [W/m^2] and on pressures, in particular n the critical pressure p_{cr} [bar], which is the pressure corresponding to the critical point (thermodynamic condition in which vapor can not be liquefied by compression) and by the reduced pressure p_r which is the ratio between the pressure of a fluid and its critical pressure. This correlation is easier to use than the Rohsenow correlation, and can be very useful if some of the fluid's properties are not available.

Another widely used correlation is the Cooper's one (Collier & Thome, 1994):

$$h = 55 * p_r^{0.12-0.4343 \ln R_p} (-0.4343 \ln p_r)^{-0.55} M^{-0.5} q_s''^{0.67} \qquad (eq. 2.7)$$

Also this correlation depends strongly on the reduced pressure p_r, but also on the molecular weight of the liquid M [g/mol], on the heat flux [W/m^2] and also on the surface's roughness R_p [μm]. For unspecified surface, R_p is set equal to 1.0 μm. Cooper also suggested multiplying h by a factor 1.7 for boiling on horizontal copper cylinders. The range of applicability of this correlation covers values of reduced pressure from 0.001 to 0.9 and values of molecular weight from 2 up to 200.

- Maximum and minimum heat flux

The critical heat flux represent a point of great interest on the boiling curve. Zuber (Zuber, 1958), through a hydrodynamic stability analysis, obtained an expression which is approximated by eq. 2.8:

$$q''_{max} = C h_{fg} \rho_v \left(\frac{\sigma g (\rho_l - \rho_v)}{\rho_v^2} \right)^{\frac{1}{4}} \qquad (eq. 2.8)$$

Where h_{fg} is the latent heat of evaporation, g is the gravity acceleration [m/s^2], ρ is the density [kg/m^3], σ is the surface tension [N/m]. Subscript v and l are referred respectively to saturated steam

and saturated liquid. Constant C takes into account the geometry of the system, for examples for large horizontal cylinders and sphere C=π/24 (the Zuber constant), for large horizontal plates C=0.149, but in general the value C=0.15 can be used.

If heat flux drops below the minimum value, the stable vapor layer that characterizes the film boiling collapse, resulting in the cooling of the surface and the boiling regime becomes nucleate boiling. Zuber (Zuber, 1958) derived the correlation, reported in eq.2.9, for the minimum heat flux, from a large horizontal plate:

$$q''_{min} = C h_{fg} \rho_v \left(\frac{\sigma g (\rho_l - \rho_v)}{(\rho_l - \rho_v)^2} \right)^{\frac{1}{4}} \qquad (eq. 2.9)$$

It depends on the same parameters used in the previous correlation for the CHF. Also in that case fluid's properties must be evaluated in saturation conditions. The constant C=0.09 was determined by Berenson (Berenson, 1961) through experimental measurements. The results obtained by this correlation are acceptable at moderate pressure, but provides a less accurate estimation at higher pressures. Similar results is obtained for cylindrical horizontal tubes.

- Film pool boiling

When the film pool boiling is reached, a stable vapor layer can be detected on the heated surface and, at first, the dominant heat transfer mechanism is conduction through the vapor. If the wall temperature increases, radiative heat transfer becomes no more negligible, in particular when T_s>300 °C. These two phenomena are involved in the heat exchange, but their contribution is not linearly additive. Bromley investigated film boiling on horizontal tubes and suggested the calculation of the heat transfer coefficient from eq. 2.10 (Bromley, 1950):

$$\bar{h}^{\frac{4}{3}} = (\bar{h}_{conv})^{\frac{4}{3}} + \bar{h}_{rad} \bar{h}^{\frac{1}{3}} \qquad (eq. 2.10)$$

If $\bar{h}_{rad} < \bar{h}_{conv}$ the simpler eq. 2.11 can be used:

$$\bar{h} = \bar{h}_{conv} + \frac{3}{4} \bar{h}_{rad} \qquad (eq. 2.11)$$

The convective average heat transfer coefficient $\bar{h}_{conv}$ can be evaluated through eq. 2.12 for a sphere or a cylinder:

$$\overline{Nu_D} = \frac{\bar{h}_{conv} D}{k_v} = C \left[\frac{g(\rho_l - \rho_v) h'_{fg} D^3}{\nu_v k_v (T_s - T_{sat})} \right]^{\frac{1}{4}} \qquad (eq. 2.12)$$

Where D is the characteristic length, ν_v is the vapor kinematic viscosity [m^2/s], k_v is the vapor thermal conductivity [W/m/K], T_s and T_{sat} are the surface and the saturation temperature [K], C is a constant depending on geometry (0.62 for horizontal cylinders and 0.67 for spheres) and h'_{fg} is

the corrected latent heat. It takes into account the sensible heat required to keep the vapor layer above the saturation temperature and it is obtained using eq. 2.13:

$$h'_{fg} = h_{fg} + 0.8c_{p,v}(T_s - T_{sat}) \qquad (eq.\,2.13)$$

With $c_{p,v}$ that is the specific heat of vapor at constant pressure [J/kg/K].

Only vapor and liquid density and the latent heat must be evaluated at saturation condition, all the others properties must be evaluated at the film temperature T_{film} (average value between saturation temperature of vapor and surface temperature), which is defined by eq. 2.14:

$$T_{film} = \frac{1}{2}(T_{sat} + T_s) \qquad (eq.\,2.14)$$

The effective radiation coefficient is defined in eq. 2.15:

$$\bar{h}_{rad} = \frac{\varepsilon\, k_{S-B}(T_s^4 - T_{sat}^4)}{T_s - T_{sat}} \qquad (eq.\,2.15)$$

With ε emissivity of the solid and k_{S-B} the Stefan-Boltzmann constant.

2.1.3 *Parametric effects on pool boiling*

The most important aspects that affect pool boiling are liquid subcooling and solid surface roughness.

During the subcooled nucleate boiling, the heat exchange is enhanced thanks to the higher difference of temperature between the heated wall and the bulk fluid. For the natural convection heat transfer mechanism, the heat flux increases typically as $(T_s - T_l)^n$ with T_s and T_l that are respectively the hot surface temperature and the liquid temperature. The exponent n depends on geometrical parameters of the heat source and in general $5/4 \leq n \leq 4/3$. On the other hand, for nucleate boiling, the influence of subcooling can be considered negligible, even though the maximum and the minimum heat fluxes increases linearly with $\Delta T_{sub}=(T_{sat} - T_l)$. When the phase transition ends during the film boiling the heat flux increases strongly with ΔT_{sub}.

The influence of surface roughness is negligible as regards maximum and minimum heat fluxes and on film boiling. However, very rough surfaces can exchange high heat flux during the nucleate boiling regime. This because the increasing number of cavities, due to higher roughness values, provides more and large active sites for bubble growth, thus the nucleation site density is higher for rough surfaces than for smooth surface. However, under prolonged boiling, the effect of surface roughness generally diminish because larger nucleation sites are not stable sources of vapor entrapment.

2.2 CONDENSATION

Condensation is a heat removal process from a system by which vapor becomes liquid. This phenomenon can happen if the vapor is cooled and reaches saturation conditions so that the nucleation of droplets is induced. It's possible to distinguish the homogeneous and the heterogeneous condensation. In the first case the vapor condenses uniformly, for example through direct contact with a cold liquid. The second case is probably the most widely used for industrial applications because is the typical condensation mechanism occurring on cooled walls in contact with vapor. For the heterogeneous condensation there are two different mechanisms: drop-wise condensation and film-wise condensation. If the cooling wall is not wetted, vapor condenses as droplets that can grow in case of further condensation, otherwise, if the surface is easily wetted, the vapor that condenses producing a liquid film on the cooling wall. A schematic representation of condensation's mechanisms is shown in Fig. 2.3. In this section only the film condensation will be discussed for both laminar and turbulent flow regime.

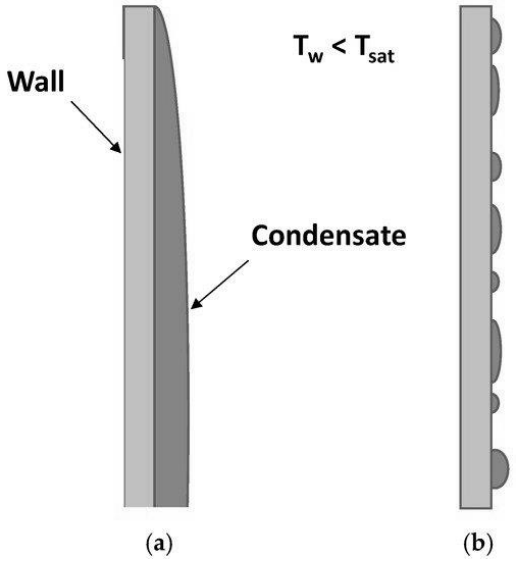

Fig. 2.4. Schematic representation of condensation modes on a vertical surface: (a) film-wise, (b)drop-wise (Khan, Tahir, Baloch, & Koç, 2019)

2.2.1 *Laminar film condensation on vertical surface*

During the laminar film condensation, assuming a downward motion of the vapor, the heat transfer coefficient depends on the hydrodynamics of the two phase fluid and on the heat transfer due to the latent heat.

As regards the hydrodynamics, an infinite portion of liquid film on the surface can be taken into account in order to analyze the force balance on a small control volume (see Fig. 2.4). Liquid properties are evaluated at the film temperature.

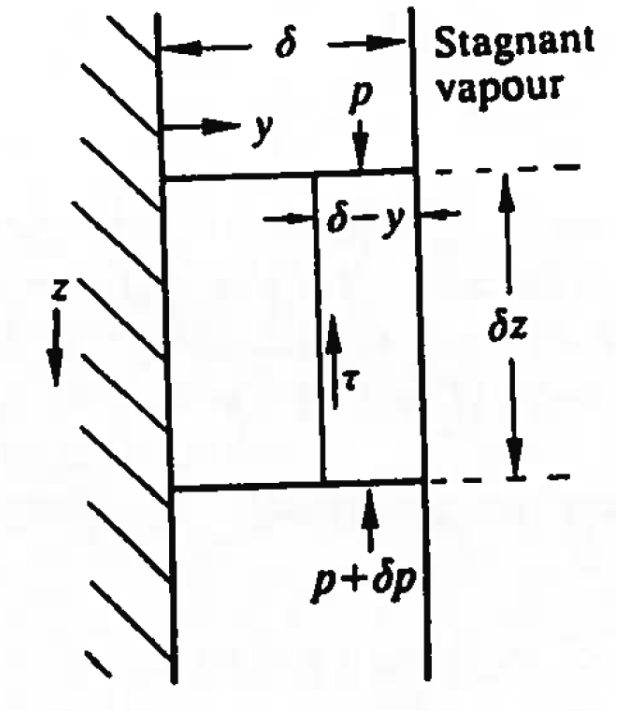

Fig. 2.5. Force balance in the liquid film control volume. Liquid is moving downward (Whalley, 1987)

The force balance in the vertical direction is written in eq. 2.16:

$$\tau * \delta z + \delta p * (\delta - y) = \rho_l * g * (\delta - y) * \delta z \qquad (eq. 2.16)$$

Where τ is the shear stress [Pa] δ is the thickness of the boundary layer, ρ_l is the liquid density. Knowing that for the laminar flow streamlines are vertical, the difference of pressure can be also written as

$$\delta p = \rho_g * g * \delta z \qquad (eq. 2.17)$$

So that the shear stress is given by:

$$\tau = \left(\rho_l - \rho_g\right) * g * (\delta - y) \qquad (eq. 2.18)$$

Reminding the definition of shear stress showed in eq. 2.19:

$$\tau = \mu_l * \frac{du}{dy} \qquad (eq. 2.19)$$

With *u* the liquid velocity along the z direction. Imposing the boundary condition *u(y=0)=0,* liquid velocity can be written in the form of eq. 2.20:

$$u = \frac{(\rho_l - \rho_g) * g * y}{\mu_l} * \left(\delta - \frac{y}{2}\right) \qquad (eq.\,2.20)$$

Which is true only if $\tau(y= \delta)=0$. In that case the relationship between the liquid mass flowrate variation respect to the film thickness is:

$$\frac{dM}{dz} = \frac{\rho_l(\rho_l - \rho_g)g}{\mu_l}\delta^2\frac{d\delta}{dz} \qquad (eq.\,2.21)$$

Integrating eq. 2.21 respect to the *y* direction, mass flowrate per unit width of liquid film is given by the eq. 2.22:

$$M = \int_0^{\delta} \rho_l\, u\, dy = \frac{\rho_l(\rho_l - \rho_g)g}{\mu_l}\frac{\delta^3}{3} \qquad (eq.\,2.22)$$

Concerning the heat transfer due to the latent heat, the exchanged heat flux depends on the condensate mass flowrate as follows:

$$q'' = h_{fg} * \frac{dM}{dz} \qquad (eq.\,2.23)$$

However, assuming that the thermal power is exchanged only through conduction, the heat flux can be also written as:

$$q'' = \Delta T_{sat}\frac{k_l}{\delta} \qquad (eq.\,2.24)$$

Where k_l is the liquid thermal conductivity [W/m/K].

Using eq. 2.24 in eq. 2.23, the liquid mass flowrate variation respect to the film thickness reported in eq. 2.21 can be rewritten as:

$$\frac{dM}{dz} = \frac{k_l \Delta T_{sat}}{h_{fg}\delta} \qquad (eq.\,2.25)$$

So that, it is possible to obtain the expression for the film thickness respect to z:

$$\delta^3\, d\delta = \frac{\mu_l k_l \Delta T_{sat}}{\rho_l(\rho_l - \rho_g)g\; h_{fg}} dz \qquad (eq.\,2.26)$$

Assuming that the thickness of the liquid is zero when *z=0* and then integrating, the film width at a certain distance *z* from the top becomes:

$$\delta = \left[\frac{4\mu_l k_l \Delta T_{sat} z}{\rho_l(\rho_l - \rho_g)g}\right]^{1/4} \qquad (eq.\,2.27)$$

Knowing the actual value of δ from eq. 2.27, the local heat transfer coefficient and the average one can be obtained from eq. 2.28:

$$h(z) = \frac{k_l}{\delta(z)} \qquad (eq.\,2.28)$$

Using eq. 2.27 in eq. 2.28, the final expression of the average heat transfer coefficient is given by eq. 2.29:

$$h = \frac{1}{L}\int_0^L h(z)dz = \frac{8^{\frac{1}{2}}}{3}\left[\frac{\rho_l(\rho_l - \rho_g)g\, h_{fg}\, k_l^3}{\mu_l\, \Delta T_{sat}\, L}\right]^{\frac{1}{4}} \qquad (eq.\,2.29)$$

Actually, when the vapor condenses on the cold wall it becomes subcooled liquid. In order to take into account also this component during the heat transfer process is sufficient to modify the latent heat. Two different correlations are listed below (eq. 2.30 and eq. 2.31).

Rohsenow (Rhosenow, 1956) suggested:

$$h'_{fg} = h_{fg} + 0.68\, c_{p,l}(T_{sat} - T_w) \qquad (eq.\,2.30)$$

Some years later, Sadasivan and Lienhard (Sadasivan & Lienhard, 1987) discovered that the modified latent heat depends also on the Prandtl number, for Pr_l>0.6 :

$$h'_{fg} = h_{fg} + \left(0.968 - \frac{0.163}{Pr_l}\right) c_{p.l}(T_w - T_{sat}) \qquad (eq.\,2.31)$$

The result obtained by the eq. 2.29, corrected by eq. 2.30 and eq. 2.31, can be also used for vertical tubes with radius $r \gg \delta$.

2.2.2 *Turbulent film condensation*

During the laminar flow, film's surface can be considered smooth, but if the average velocity in the liquid layer increases, the Reynold number inside the film increases to. It is defined by eq. 2.32:

$$Re_\delta = \frac{4M}{\mu_l} \qquad (eq.\,2.32)$$

And for values $\lesssim 30$ the flow regime is laminar. Then some waves on the film-vapor interface can be formed during the transition region. When $Re_\delta \simeq 1800$ the flow regime can be considered turbulent.

Some correlations can be used in order to evaluate the global Nusselt number during the transition and the turbulent flow regime. For the wavy regime, the Kutateladze (Kutateladze, 1963)correlation shown in eq. 2.33, is suggested:

$$\overline{Nu}_L = \frac{Re_\delta}{1.08\, Re_\delta^{1.22} - 5.2} \qquad (eq.\,2.33)$$

And for turbulent regime the Labuntsov (Labuntsov, 1957) correlation can be used:

$$\overline{Nu}_L = \frac{Re_\delta}{8750 + 58\, Pr_l^{-0.5}(Re_\delta^{0.75} - 253)} \qquad (eq.\,2.34)$$

2.2.3 *Phenomena affecting condensation*

The condensation analysis just discussed is not completely representative of the complex mechanisms interacting during condensation phenomena on a vertical surface and there are some aspects that need to be considered during future experimental measurements.

As concerns the phenomena that increase the heat transfer rate from the inner tube, they are:

- Liquid-vapor interface almost never smooth as in the control volume showed in Fig. 2.5. This results in an increase of the area of heat transfer and the heat transfer coefficient may be almost 20% higher, in particular during the wavy regime.
- Effect of shear stresses. During the condensation analysis no shear stresses on the liquid-vapor interface were considered, but actually they make the liquid film thinner, improving the heat transfer because the thermal resistance becomes lower.
- Turbulent flow. The film flow regime may become turbulent, and turbulences have two opposite effects: they increase the liquid viscosity making the layer thicker, and they increase the motion of the fluid. Anyway the resulting effect is the increase of the heat transfer coefficient.

On the other hand, the presence of incondensable gases inside the two-phase mixture condensing on the surface reduce the mass-flowrate of condensate, reducing the heat transfer coefficient.

3. *PRELIMINARY ANALYSIS OF THE SYSTEM*

In this section a preliminary analysis of the heat transfer characteristics of an experimental pool heat exchanger are discussed. The goal of this analysis is to evaluate the order of magnitude of the parameters (e.g. wall temperatures, exchanged heat flux, heat transfer coefficient) that characterizes different heat transfer mechanisms involved in a pool tank filled by water, which can be heated up in two different way: by an electrically heated rod (imposed heat flux configuration) or by dry saturated steam which is supposed to flow inside a tube (imposed temperature configuration). The heat transfer mechanisms taken into account are basically: natural convection and saturated nucleate boiling occurring on the outer surface of the heat source. Considering the tube as heat source, rather than the heating rod, also conduction through the tube is taken into account.

3.1 SYSTEM DESCRIPTION

The system is represented by a steel tank (inner diameter equal to 592 mm, height equal to 1000 mm) filled by water (water height equal to 700 mm) at the atmospheric pressure. As regards the heat source, for the imposed temperature configuration, a test tube (inner diameter of 20.7 mm, thickness of 6.35 mm) is adopted. For the imposed heat flux configuration an electrically heated rod (same tube's outer diameter, thermal power equal to 3300 W) is considered. The heat source is placed at the center of the tank. A schematic of the system is shown in Fig. 3.1 and in Fig. 3.2.

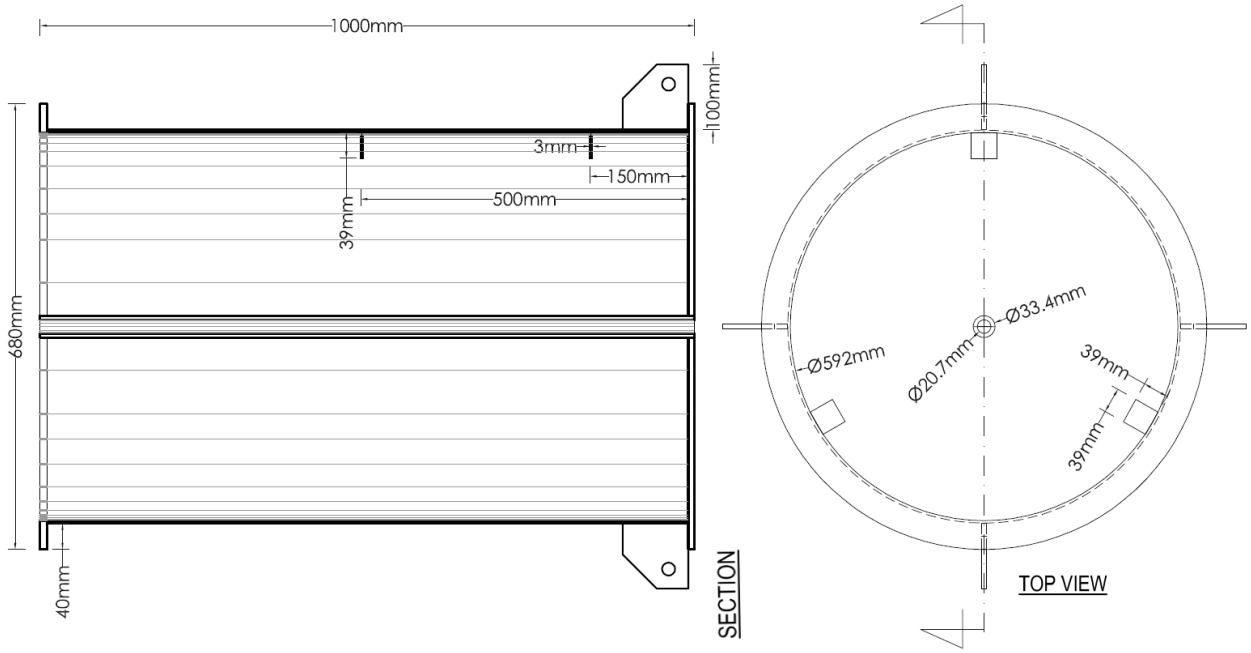

Fig. 3.1. Top view and section of the system (tank and tube configuration)

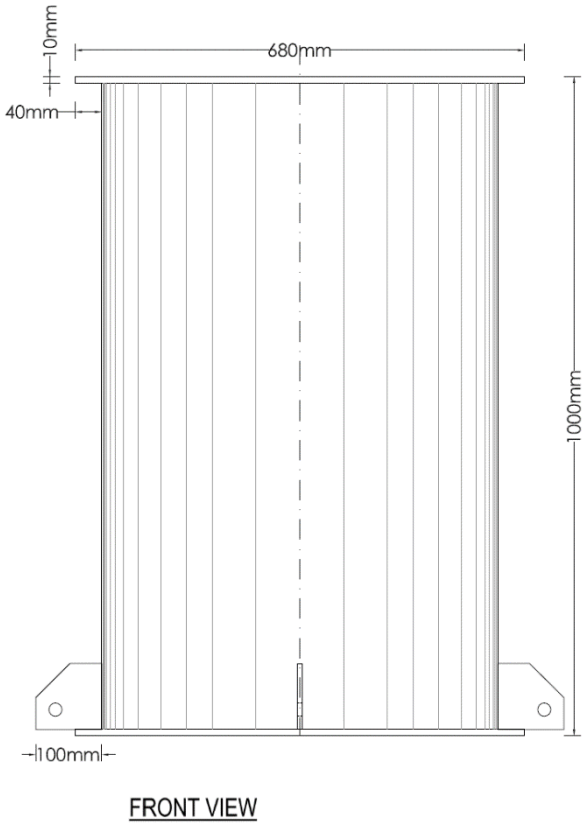

Fig. 3.2 Tank front view.

Main operating parameters are shown in table 3.1:

Table 3.1. Main operating parameters

Parameter	Value	U.M.
Tube's outer diameter (d_{out})	33.4	mm
Tube's inner diameter (d_{in})	20.7	mm
Tube's active length (L)	700	mm
Tank's inner diameter (D_{in})	592	mm
Inner pressure (p_{in})	4	bar
Inner temperature (T_{in})	143.6	°C

Test tube inlet mass flowrate (W)	12.5	g/s
Pool pressure (p_{pool})	1.0133	bar
Pool saturation temperature (T_{sat})	99.9	°C
Electrically heated rod's thermal power (Q)	3300	W

Knowing the geometrical parameters of the system, the reference mass of water inside the system and the corresponding thermal capacity con be obtained, in order to characterize the pool. The volume occupied by the water inside the pool is given by eq. 3.4:

$$V_{pool} = \pi L \left(\frac{d_{in,tank}^2}{4} - \frac{d_{out,tube}^2}{4} \right) = 0.1921 \, [m^3] \qquad (eq. 3.1)$$

And the total mass of water inside the pool can be obtained by eq. 3.2.

$$M_{water} = \rho_{pool}(20°C) * V_{pool} = 191.71 \, [kg] \qquad (eq. 3.2)$$

Then the pool's thermal capacity is:

$$C_{water} = c_p(20°C) * M_{water} = 802.27 \left[\frac{kJ}{K} \right] \qquad (eq. 3.3)$$

3.2 HEAT TRANSFER IN THE POOL

The considered heat transfer mechanisms are: conduction through cylindrical wall (thermal resistance of the condensed film layer is neglected), and with the pool free convection until average pool temperature is lower than saturation temperature at the atmospheric pressure, otherwise, saturated pool boiling. In order to characterize the process of heat transfer inside the experimental pool, a simplified model based on correlation is adopted. The most important parameters involved in the heat exchange are evaluated (e.g. average heat flux, average heat transfer coefficient, outer wall temperature) considering the imposed temperature configuration. Correlations (eq. 3.5-3.8) are used to compute the average heat transfer coefficient for natural convection heat transfer on vertical cylindrical surfaces and for the saturated pool boiling.

3.2.1 *Model's description*

The hypothesis on which the model is based are listed below:

- Imposed temperature configuration.

- All properties and parameters (e.g. temperatures, heat flux, heat transfer coefficient…) are spatially averaged over the active tube length (assumed to be 700 mm).
- Quasi-steady state assumption: the system's evolution is studied as a sequence of steady states in which all properties and parameters are evaluated for fixed values of pool temperature.
- Pool temperature is imposed between 20 °C and water's saturation temperature at atmospheric pressure.
- Tube's material is stainless steel AISI 304, and its properties does not change with temperature.
- Film thermal resistance on the inner tube's surface is neglected, so the inner wall temperature is the saturation temperature of the steam flowing inside.
- Constant dry saturated steam mass flowrate at the tube's inlet section.
- Constant inner pressure inside the tube.
- Subcooled boiling is not taken into account. When liquid temperature is lower than the saturation value natural convection occurs, otherwise saturated nucleate boiling is considered.

The heat transfer process can be schematically represented in Fig. 3.3 by the equivalent thermal circuit.

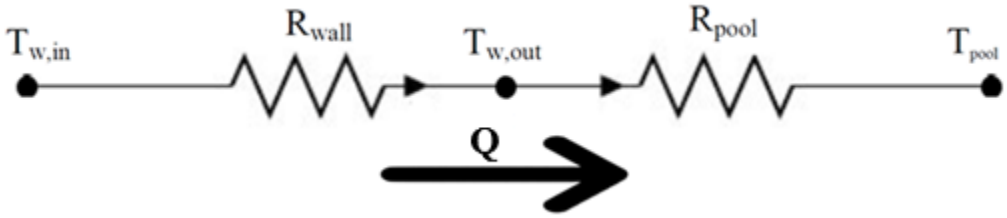

Fig. 3.3. Equivalent thermal circuit (imposed temperature configuration)

Where R_{wall} and R_{pool} are respectively the tube's thermal resistance and the pool thermal resistance [K/W]. They are defined in eq. 3.4.

$$R_{wall} = \frac{\ln\left(\frac{d_{out}}{d_{in}}\right)}{2 * \pi * L * k_{wall}};\ R_{pool} = \frac{1}{d_{out} * \pi * L * h_{out}} \qquad (eq.3.4)$$

Wall thermal resistance is assumed spatially constant and time-independent (geometry fixed, wall thermal conductivity independent from the temperature). Pool thermal resistance depends on the average global heat transfer coefficient, according to the heat transfer mechanism occurring on the outer wall surface. The thermal power exchanged through conduction between $T_{w,in}$ and $T_{w,out}$ is the same exchanged between $T_{w,out}$ and T_{pool}:

$$Q = \frac{T_{w,in} - T_{w,out}}{R_{wall}} = \frac{T_{w,out} - T_{pool}}{R_{pool}} = \frac{T_{w,in} - T_{w,pool}}{(R_{wall} + R_{pool})} \qquad (eq.\,3.5)$$

Each one of the heat transfer mechanisms occurring on the outer wall of the heat source is described by different empirical correlations which can be used in order to evaluate the average heat transfer coefficient.

As regards the natural convection regimes, correlations usually give as a result the Nusselt number. In this case the following correlation are used:

- Correlation 1: Churchill and Chu (eq. 3.6)

$$Nu_{L,flat\ plate} = \left(0.825 + \frac{0.387 * Ra^{\frac{1}{6}}}{\left(1 + \left(\frac{0.492}{Pr}\right)^{\frac{9}{16}}\right)^{\frac{8}{27}}} \right)^2 \qquad (eq.\,3.6)$$

  This correlation is valid for external flow on vertical flat plates and can be applied over a wide range of Rayleigh number (eq. 1.32) (from $Ra \sim 10^{-1}$ to $Ra \sim 10^{12}$). Fluid properties must be evaluated at the film temperature. (Incropera, Dewit, Lavine, & TheodoreL., 2011).

- Correlation 2: Fujii and Uehara (eq. 3.7)

$$Nu_L = Nu_{L,flat\ plate} + 0.97 * \frac{h}{D} \qquad (eq.\,3.7)$$

  This correlation is developed for external flow heat transfer from vertical cylinders. (Fujii & Uehara, 1970) and h is the tube's height and D its outer diameter. It can be applied for height to diameter ration from 1 to 60.

Concerning the saturated nucleate boiling, Cooper's correlation was used (eq. 3.8)

- Correlation 3: Cooper

$$h_{out} = 55\, p_r^{0.12 - 0.4343 \ln(\epsilon)} (-0.4343 * \ln(p_r))^{-0.55}\, M^{-0.5} (q")^{\frac{2}{3}} \qquad (eq.\,3.8)$$

  Where p_r is the reduced pressure and it is defined as the ratio between the pressure of the system (atmospheric pressure equal to 1.0133 bar) and the critical pressure of water (equal to 220.6 bar), M is the molecular weight of water [g/mol], q" is the exchanged heat flux [W/m^2] and ϵ is the surface's roughness [μm] (if this data is not available Cooper suggested to use 1 μm). (Coolier & J.R., 1994).

A script based on above mentioned hypothesis and correlation is implemented in order to evaluate the main heat transfer characteristics.

3.3 SCRIPT'S DESCRIPTION

The explanation of the implemented script will be addressed in this section. The objective of this analysis is the estimation of: average temperature on the outer tube's surface, average heat transfer coefficient between outer tube's surface and pool and average heat flux exchanged with the pool. The analysis is based on an iterative procedure: a pool temperature is fixed and an arbitrary value of the heat flux is initially guessed. Then, outer wall temperature and heat transfer coefficient are evaluated. A new value of heat flux is computed and it is compared with the guessed one. The value of the initially guessed heat flux is updated with the last computed value. When the relative error between the guessed and the computed heat flux becomes lower than a required tolerance, the convergence process ends. This procedure is repeated for different values of pool temperature (it varies from 20°C to water saturation temperature at atmospheric pressure). Flowcharts showing the script's procedure are shown, in Fig. 3.4 and Fig. 3.5, at the end of this section.

3.3.1 *Inner wall temperature*

At first, geometrical parameters and operating conditions (pressure and mass flowrate inside the tube) are set. At the pipe's inlet, fluid is dry saturated steam. Assuming that the thermal resistance of the liquid film condensed on the inner wall surface is zero, the inner wall temperature is:

$$T_{w,in} = T_{sat}(p_{in}) = T_{sat}(4\ bar) = 143.6\ °C$$

Then the pool temperature $T_{pool(i)}$ is set. If pool temperature is lower than T_{sat}, natural convection is the dominating heat transfer mechanism, otherwise the saturated pool boiling must be evaluated.

3.3.2 *Outer wall temperature*

An arbitrary value of the heat flux *q"* is guessed in order to evaluate the outer wall temperature through the conduction equation (eq. 3.9), derived by eq. 3.5:

$$T_{w,out} = T_{w,in} - q" * (\pi * L * d_{out}) * R_{wall} \qquad (eq.\ 3.9)$$

Wall thermal resistance is a constant since geometry is fixed and the material properties are assumed spatially constant and independent from temperature (k_{wall}=15.75 W/m/K).

3.3.3 *Water properties and dimensionless parameter*

Thermophysical properties of water are evaluated at the film temperature (eq. 2.14), that is the average temperature between the hot surface and the pool temperature. All properties are obtained using XSteam for Matlab, except for the water expansion coefficient β [1/K] since its value it not

explicitly provided by XSteam. For this reason β is computed assuming a linear behavior between 20°C and T_{sat}, thus it is obtained through linear interpolation, from eq. 3.10:

$$\beta(T_{film}) = \beta(20°C) + \left(\beta(T_{sat}) - \beta(20°C)\right) * \frac{T_{film} - 20°C}{T_{film} - T - sat} \qquad (eq. 3.10)$$

Where β(20°C)=2.275x10^{-4} 1/K and $\beta(T_{sat})$=7.501x10^{-4} 1/K.

When the film temperature reaches the saturation value, film temperature is assumed constant (equal to T_{sat}) and fluid properties are evaluated in saturated conditions. In order to calculate the natural convection average heat transfer coefficient, the average Grashof number and the Prandtl number must be evaluated. Their expression is written in eq. 3.11 and 3.12.

$$Gr_L = \beta * g * \left(T_{w,out} - T_{pool}\right) * \frac{L^3}{\nu^2} \qquad (eq. 3.11)$$

$$Pr = \mu * \frac{c_p}{k} \qquad (eq. 3.12)$$

Where g is the gravity acceleration [m/s^2], L is the active tube length and ν is the cinematic viscosity [m^2/s], μ is the dynamic viscosity [Pa*s], c_p is the specific heat at constant pressure [J/kg/K] and k is the water thermal conductivity [W/m/K].

Grashof and Prandtl numbers are necessary to evaluate the global Rayleigh number. It is computed as follows:

$$Ra_L = Gr_L * \mathrm{Pr} \qquad (eq. 3.13)$$

It is a dimensionless number too and it is used in order to evaluate the global Nusselt number through correlations previously written in eq. 3.6, which gives as result the global Nusselt number for flat plates, and in eq. 3.7, which gives the actual global Nusselt number for cylindrical geometry.

3.3.4 *Heat transfer coefficient*

Knowing the value of the global Nusselt number, it is possible to obtain the heat transfer coefficient for natural convection regime thanks eq. 3.14, which is the definition of Nusselt number, and eq. 3.15.

$$Nu_L = h_{out} * \frac{L}{k_{water}} \qquad (eq. 3.14)$$

So that:

$$h_{out} = Nu_L * \frac{k_{water}}{L} \qquad (eq. 3.15)$$

This procedure can be followed until the pool temperature is lower than T_{sat}. When saturation conditions are reached inside the pool, the heat transfer coefficient is evaluated by using correlation described by eq. 3.8.

3.3.5 *Average power and average heat flux*

Now that the average global heat transfer coefficient is known, the thermal power exchanged can be obtained using the eq. 3.16:

$$Q = \pi L \frac{T_{w,in} - T_{pool}}{\frac{1}{2\,k_{wall}} \ln\left(\frac{d_{out}}{d_{in}}\right) + \frac{1}{d_{out}\,h_{out}}} \qquad (eq.\,3.16)$$

And the heat flux is computed as the ratio between the result of eq. 3.17 and the heat transfer area, as written in eq. 3.17:

$$q" = Q/(\pi * L * d_{out}) \qquad (eq.\,3.17)$$

Finally the computed value can be compared with the guessed one through the evaluation of the relative error:

$$relative\ error = |q" - q"_{guessed}|/q"_{guessed} \qquad (eq.\,3.18)$$

After that, the value of the guessed heat flux is updated with the computed one coming from eq. 3.17 and a new iteration is carried out. When the relative error is lower than the required tolerance (10^{-4}), a new value of pool temperature is imposed and the convergence procedure restarts with the same initial guessed on the heat flux.

3.3.6 *Vapor quality*

From the experimental point of view, the exchanged heat flux can not be directly measured. By the way, it can be evaluated by monitoring the condensed mass flowrate at the outlet. Assuming dry saturated steam at the inlet, the product between the specific enthalpy of vaporization H_{fg} and the condensed mass flowrates is the heat power input to the system. Knowing the total heat input, it is possible to obtain the average heat flux exchanged inside the system, from the inner wall to the pool using eq. 3.19 and eq. 3.20.

$$Q = W_{condensed} * H_{fg} = W(1 - x)H_{fg} \qquad (eq.\,3.19)$$

$$q" = Q/A \qquad (eq.\,3.20)$$

Where x is the vapor quality and it is defined as the ratio between the mass of steam and the total mass of the two-phase mixture.

The outlet quality is computed through eq. 3.21:

$$x_{out} = \frac{H_{out} - H_{l,sat}}{H_{v,sat} - H_{l,sat}} \qquad (eq.\,3.21)$$

H_{sat} is the specific enthalpy in saturation condition [J/kg], the subscript *l* or *v* refers to the liquid or vapor saturated conditions. Considering that the specific enthalpy at the saturation conditions depends only on one parameter (inner pressure) which is constant, the outlet title depends only on the outlet specific enthalpy.

On the other hand the outlet specific enthalpy can be using eq. 3.22:

$$H_{out} = H_{in} - \frac{Q}{W} \qquad (eq.\,3.22)$$

Where $H_{in}=H_{sat,v}(p_{in})$.

3.3.7 *Saturation time*

Finally, the time required by the pool water to reach saturation conditions is studied. Pool water temperature increases in time because of the thermal power released by the heat source. The energy *E* delivered to the pool can be obtained by eq. 3.23:

$$E = M_{water} \int_{20°C}^{T_{sat}} c_p \, dT \qquad (eq.\,3.23)$$

Knowing the mass of water and its thermal capacity, assuming that specific heat at constant pressure doesn't changes with temperature (eq. 3.1 and 3.2), the energy required by the pool water to reach the saturation conditions becomes:

$$E = C_{water} * (T_{sat} - 20°C) \cong 64.2\ MJ \qquad (eq.\,3.24)$$

In order to evaluate the time evolution of pool temperature, by the way, a time-discretization is needed, thus temperature is computed using eq.3.25:

$$T_{pool}(t) = T_{pool}(t - \Delta t) + \frac{E\,(t)}{C_{water}} \qquad (eq.\,3.25)$$

Where pool temperature at time t depends on the pool temperature evaluated at the previous time-step (Δt=1s) and the energy is obtained by eq. 3.26

$$E(t) = Q * \Delta t \qquad (eq.\,3.26)$$

Q is the average power exchanged during the time step Δt. The value of power *Q* depends on the assumed configuration. For the imposed temperature configuration, *Q* depends pool temperature at

time *t*, otherwise, for the imposed heat flux configuration it is constant (equal to 3.3 kW). A comparison between these two configuration is shown in the next section.

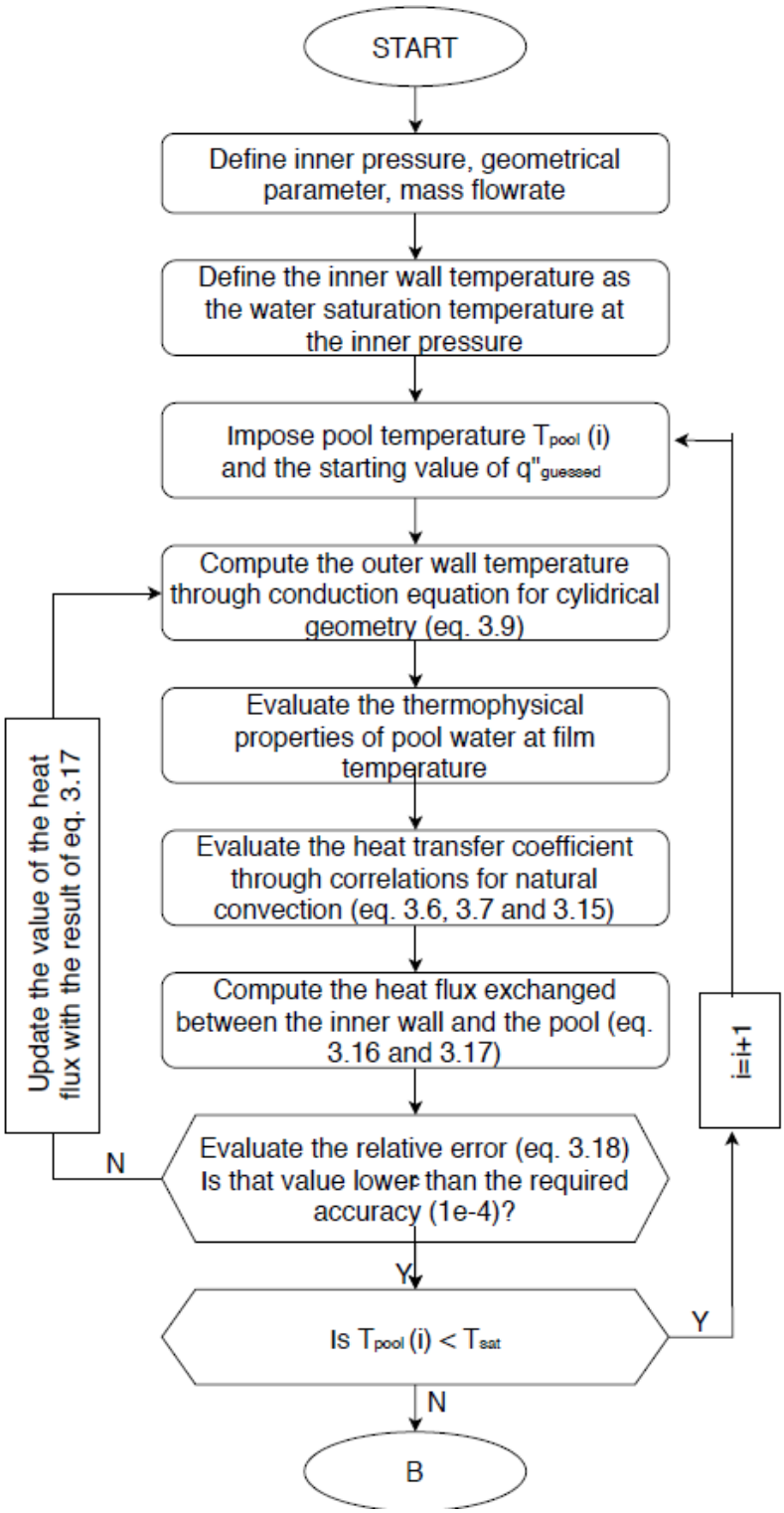

Fig. 3.4.Algorithm adopted to evaluate the heat transfer characteristics during the free convection stage

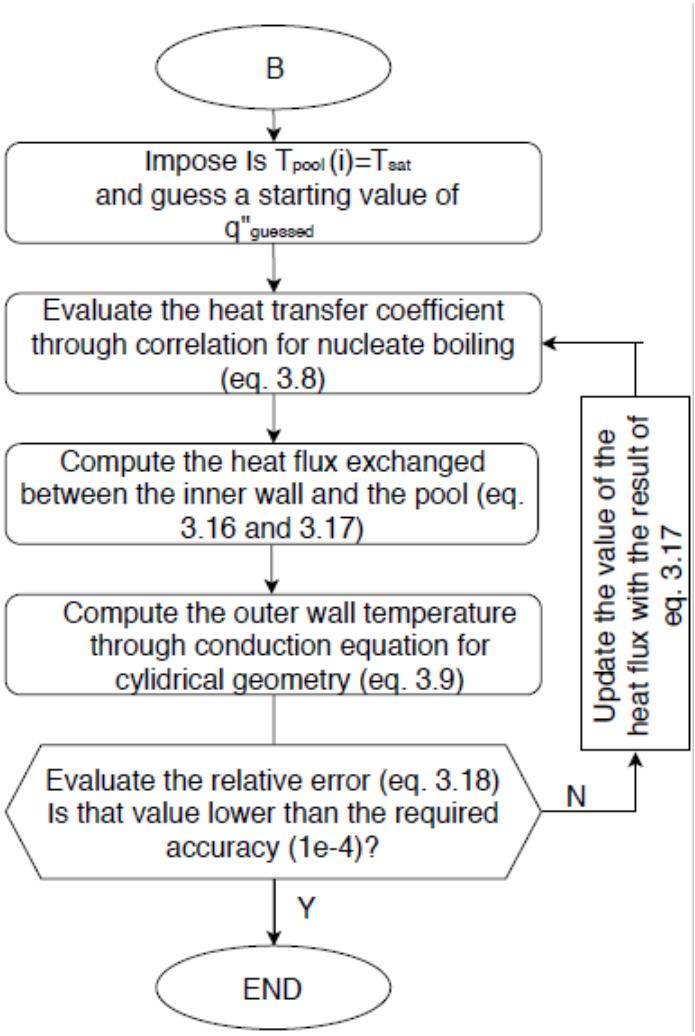

Fig. 3.5. Algorithm adopted to evaluate the heat transfer characteristics during the saturated pool boiling stage

3.4 SCRIPT'S RESULTS

At the end of the script's analysis the behavior of average outer pool temperature, average heat flux and average global heat transfer coefficient is obtained for different values of pool temperature. The script's results will be discussed in this section.

3.4.1 *Outer wall temperature*

For each value of pool temperature, a different value of heat flux is obtained and outer wall temperature is computed by eq. 3.9 (where inner wall temperature is imposed and wall thermal resistance is assumed constant). The outer wall temperature as a function of the pool temperature shows an increasing trend during the natural convection regime, as shown in Fig. 3.6. Outer wall temperature varies from 93.3 °C to 125.8 °C during the natural convection heat transfer. Then,

when pool temperature reaches the saturation value at the atmospheric pressure, outer wall temperature drops to 109.5 °C because of the more efficient heat transfer mechanism.

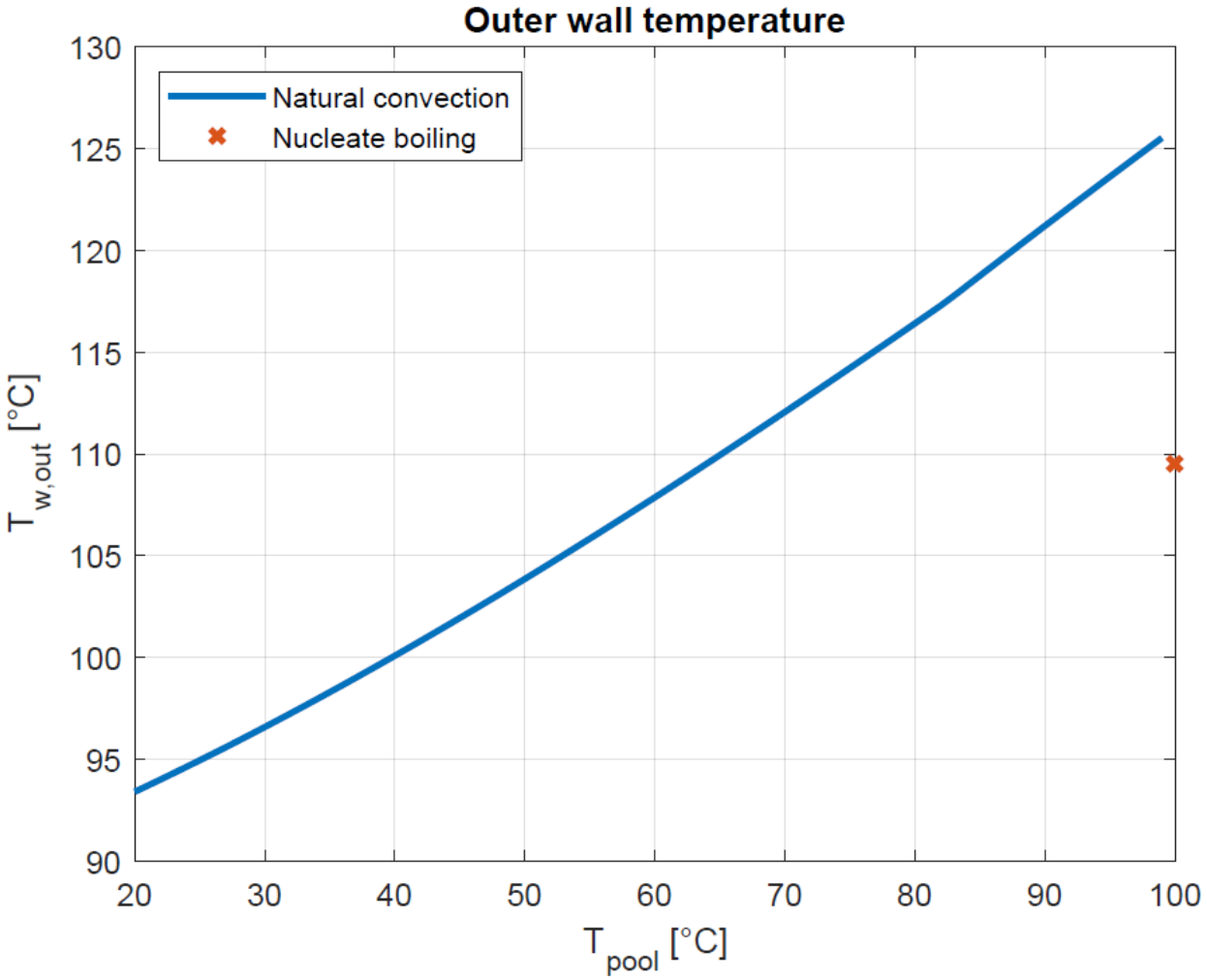

Fig. 3.6. Outer wall temperature as a function of the imposed pool temperature

The reason of the outer wall temperature behavior is that, during the steady state free convection, the heat flux decreases mainly because of the reduction of the temperature difference between the inner surface of the tube (constant) and the pool (imposed from 20 to 99 °C). As a matter of fact total thermal resistance doesn't significantly change, as shown in Fig. 3.7. Total thermal resistance depends only on the outer heat transfer coefficient (which depends on the imposed pool temperature). Total thermal resistance varies from 0.0171[K/W] and 0.0161[K/W], which corresponds a percentage maximum variation obtained by equation 3.27

$$\frac{R_{tot}(max) - R_{tot}(min)}{R_{tot}(min)} * 100 = 6.21\% \qquad (eq.\,3.27)$$

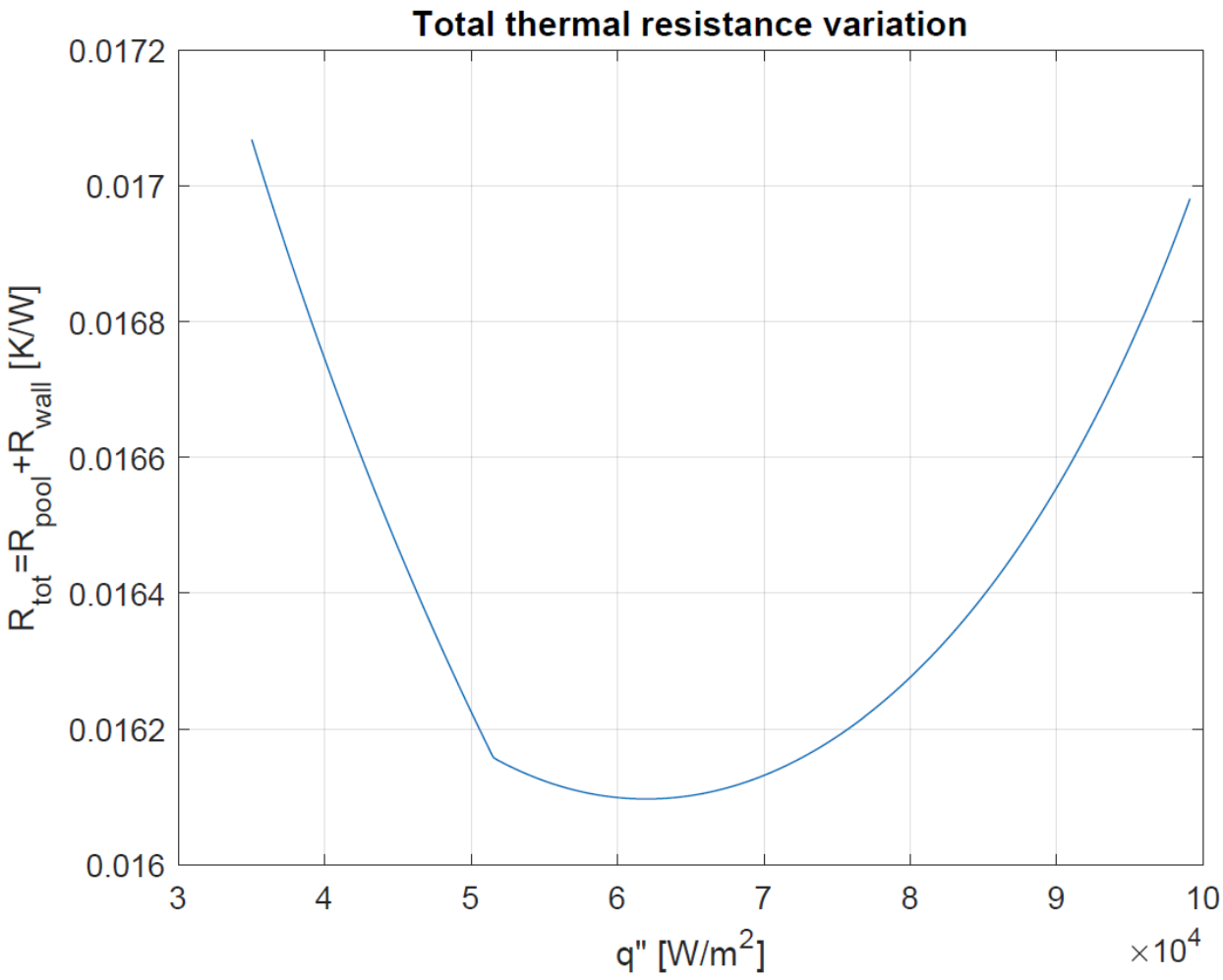

Fig. 3.7. Total thermal resistance variation as a function of the average heat flux

Since the conductive heat flux exchanged through the pipe is the same exchanged by natural convection between the pipe and the wall's outer surface, the increase of the outer wall temperature is expected for increasing values of pool temperature. As a matter of fact, outer wall temperature as a function of the exchanged heat flux is shown in Fig. 3.8. Each point of the diagram corresponds to a different pool temperature. When the exchanged heat flux decreases, reminding eq. 3.9, the outer wall temperature increases since inner wall temperature is fixed and wall thermal resistance is assumed constant (geometry is fixed and material properties are assumed spatially constant and temperature independent).

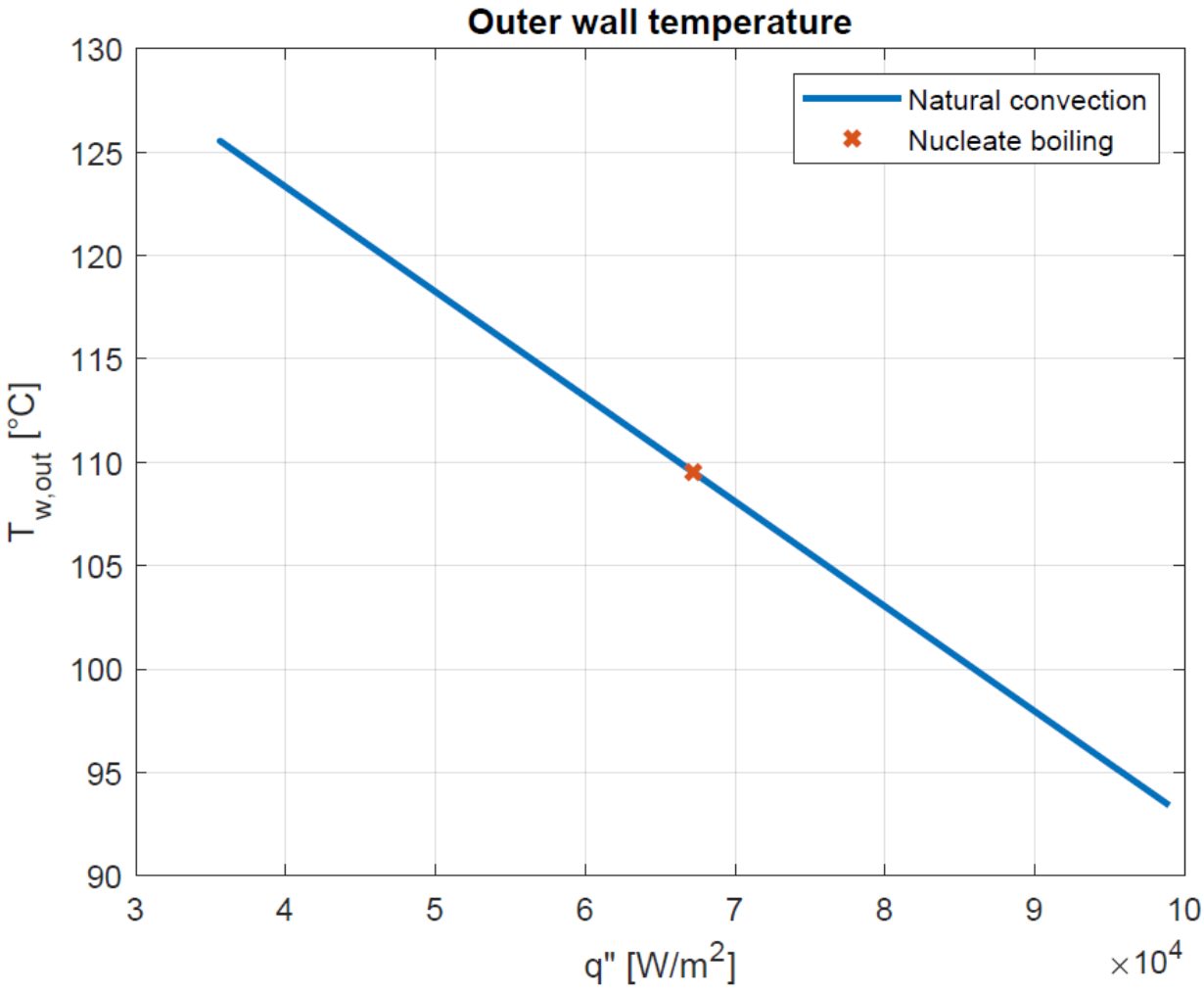

Fig. 3.8. Outer wall temperature as a function of the imposed heat flux.

Also the difference of temperature through the wall as a function of pool temperature and exchanged heat flux are shown in Fig. 3.9 and Fig. 3.10.

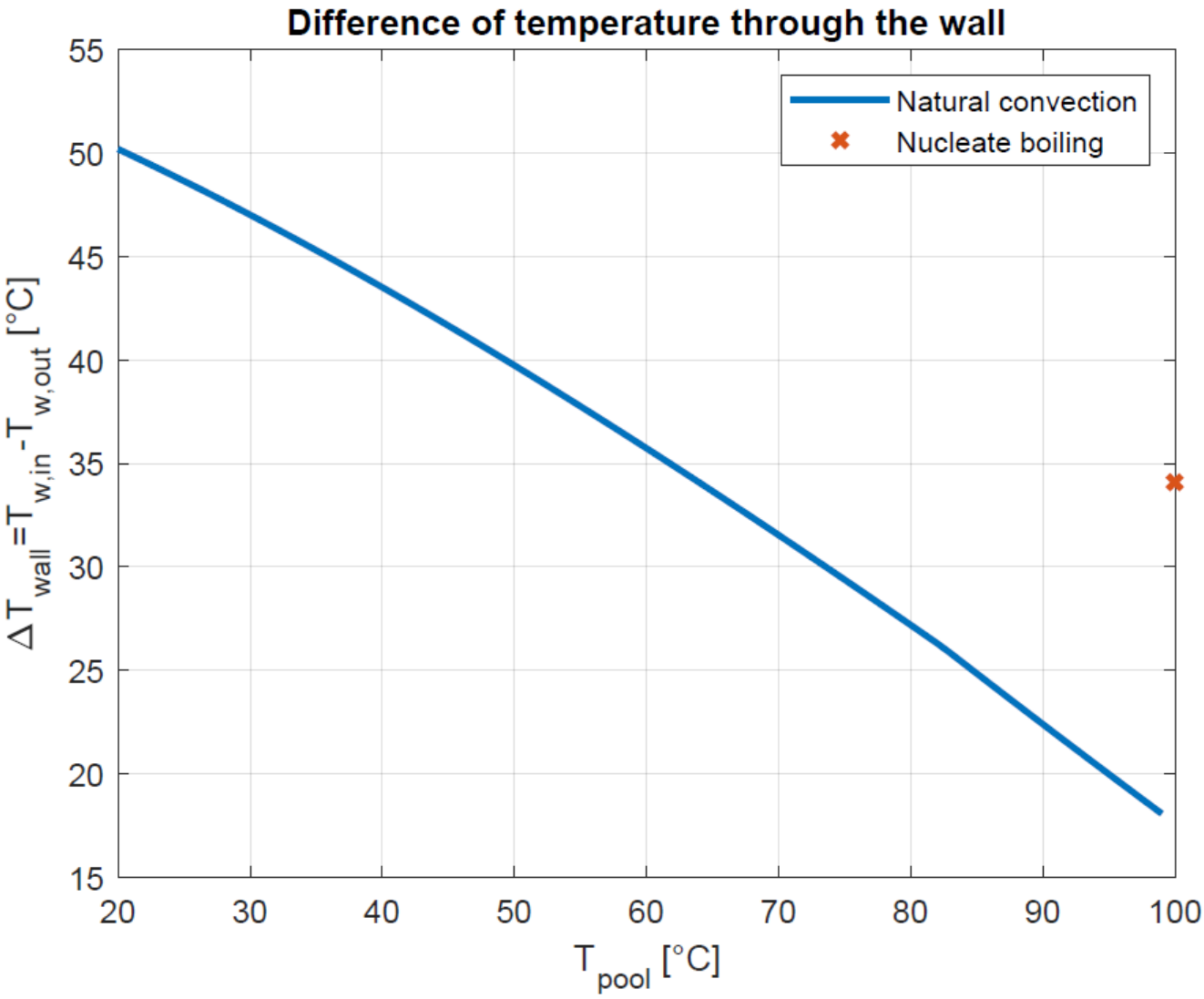

Fig. 3.9. Difference of temperature though the pipe wall as a function of the pool temperature

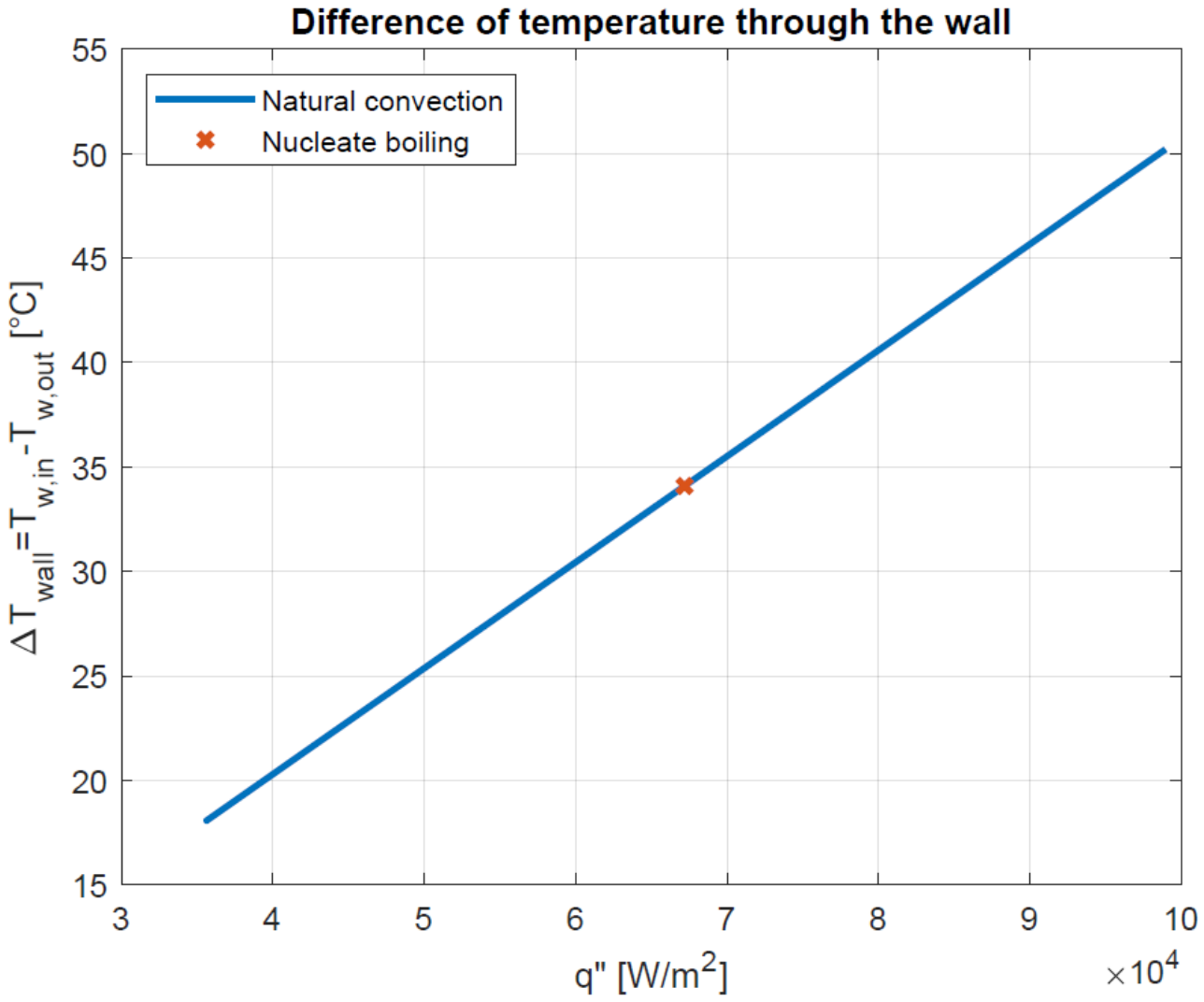

Fig. 3.10. Difference of temperature though the pipe wall as a function of the exchanged average heat flux

3.4.2 *Dimensionless parameters and heat transfer coefficient*

Churchill and Chu natural convection correlation (eq. 3.6) depends on two dimensionless parameters: *Ra* and *Pr*. In turn *Ra* depends on *Gr* and *Pr* (eq. 3.13).

Fig. 3.11 and 3.12 show the variation of *Gr* and *Pr* respect to T_{pool} and *q"*(each value of the average heat flux corresponds to a value of pool temperature). When saturation condition in the film is reached (corresponding to a pool temperature equal to 82 °C and a heat flux equal to 5.2×10^4 W/m^2), liquid properties are assumed to be constant and equal to the saturation value of the liquid. When the film reaches saturation conditions, Grashof number depends only on the difference of temperature between the wall and the pool, which becomes lower and lower, while Prandtl number is constant.

Actually when saturation conditions are reached in the film layer, some local boiling phenomena may occur (i.e. subcooled nucleate boiling), but in this analysis natural convection is taken into account until the average pool temperature reaches the saturation value at atmospheric pressure and the heat transfer mechanism is saturated nucleate boiling.

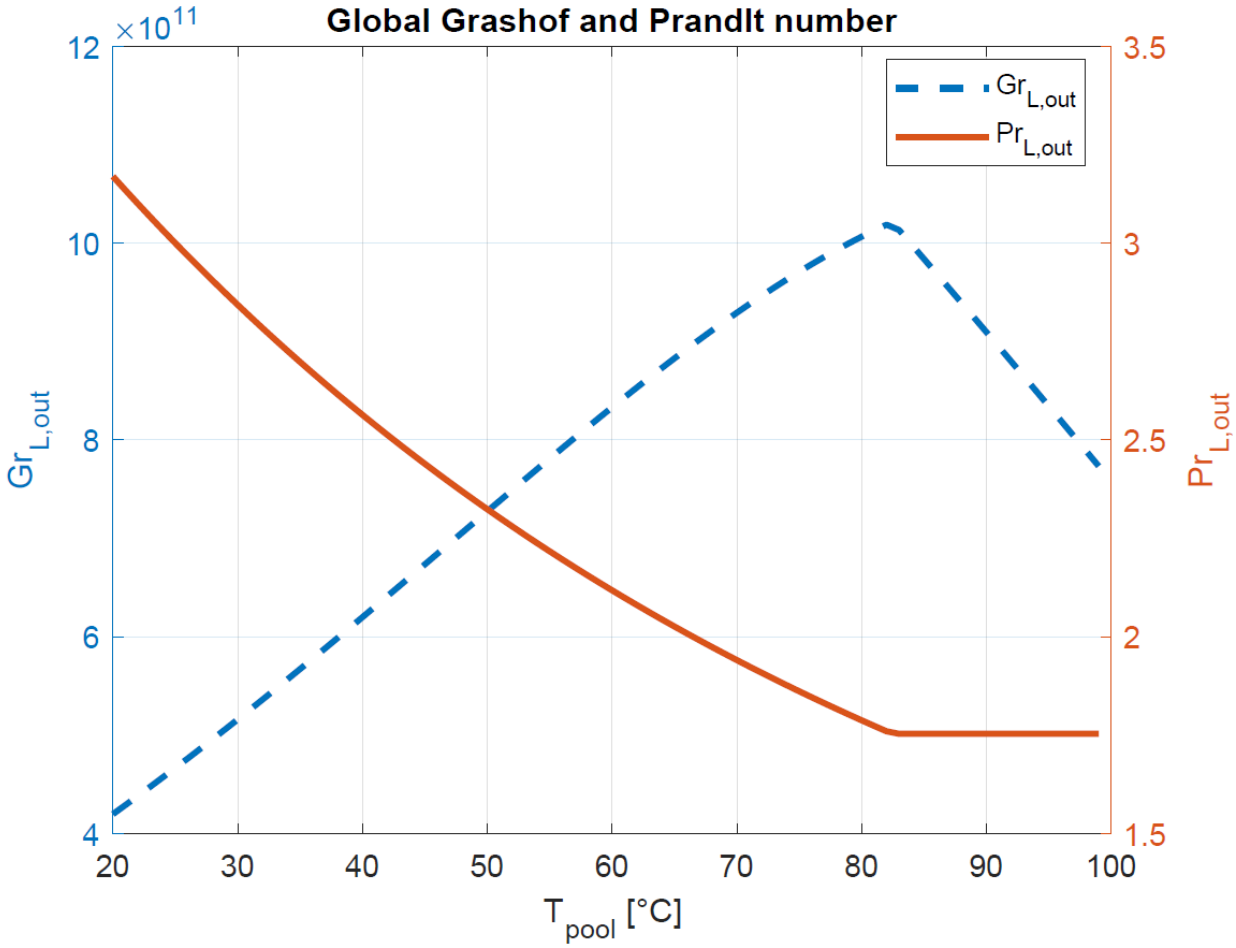

Fig. 3.11. Global Grashof and Prandtl number as functions of pool temperature

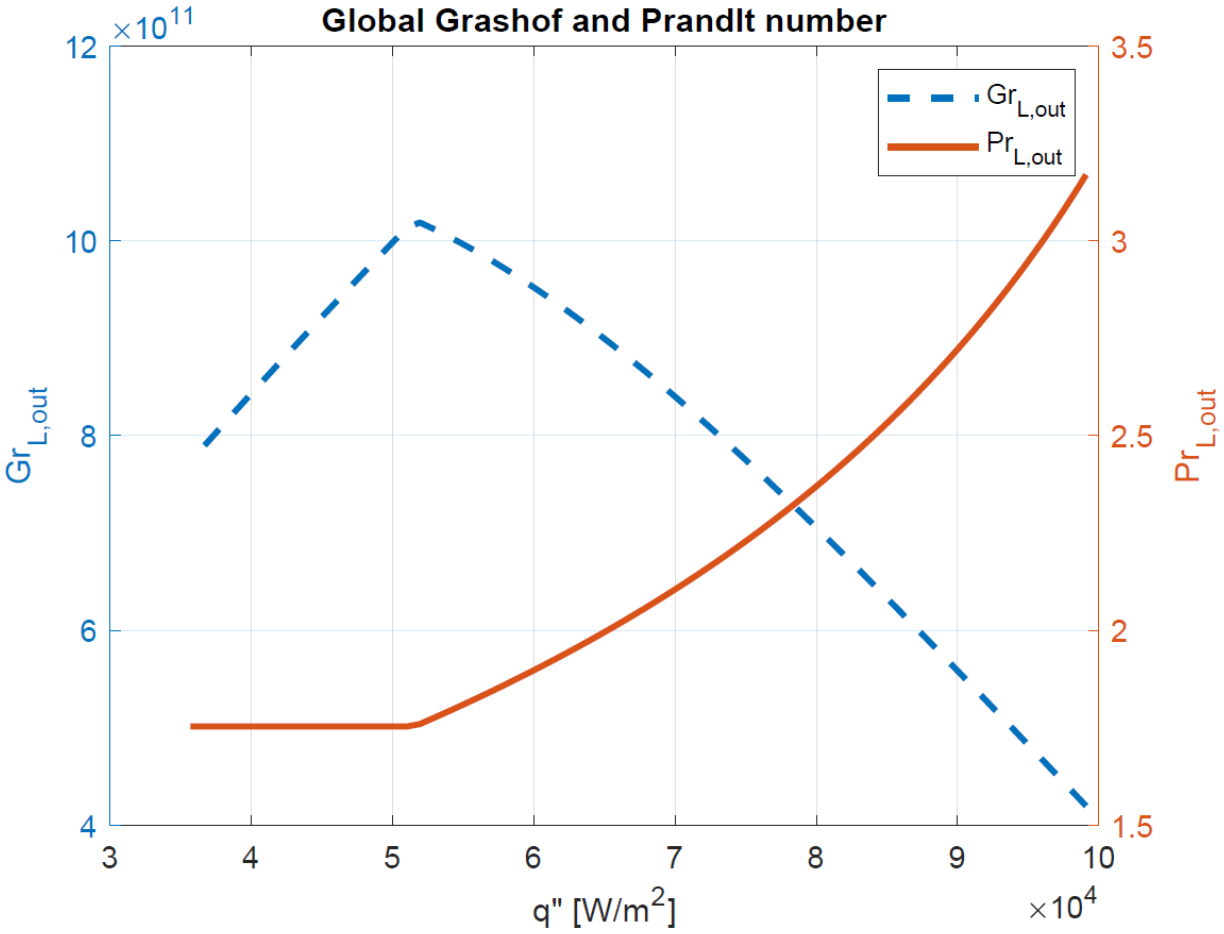

Fig. 3.12. Global Grashof and Prandtl number as functions of the heat flux

Knowing both Grashof and Prandtl numbers, the value of the Rayleigh number can be computed, thus also the Nusselt can be obtained by natural convection correlations (eq. 3.6 and eq. 3.7). *Ra* and *Nu* have almost the same behavior: when saturation conditions inside the film are reached, *Pr* is constant so they basically depends on global Grashof number. When the film is in subcooled conditions, the dependency is less obvious because *Gr* increases with the temperature, almost doubling its value between 20°C and 82°C, and *Pr* decreases, almost halving its value in the same range of temperature. By the way *Ra* and *Nu* dependency on *Gr* seems stronger that on *Pr* since also global Rayleigh and global Nusselt show a positive trend during natural convection regime.

The behavior of global Rayleigh number and global Nusselt number as functions of the heat flux and of the pool temperature are shown respectively in Fig. 3.13 and Fig. 3.14.

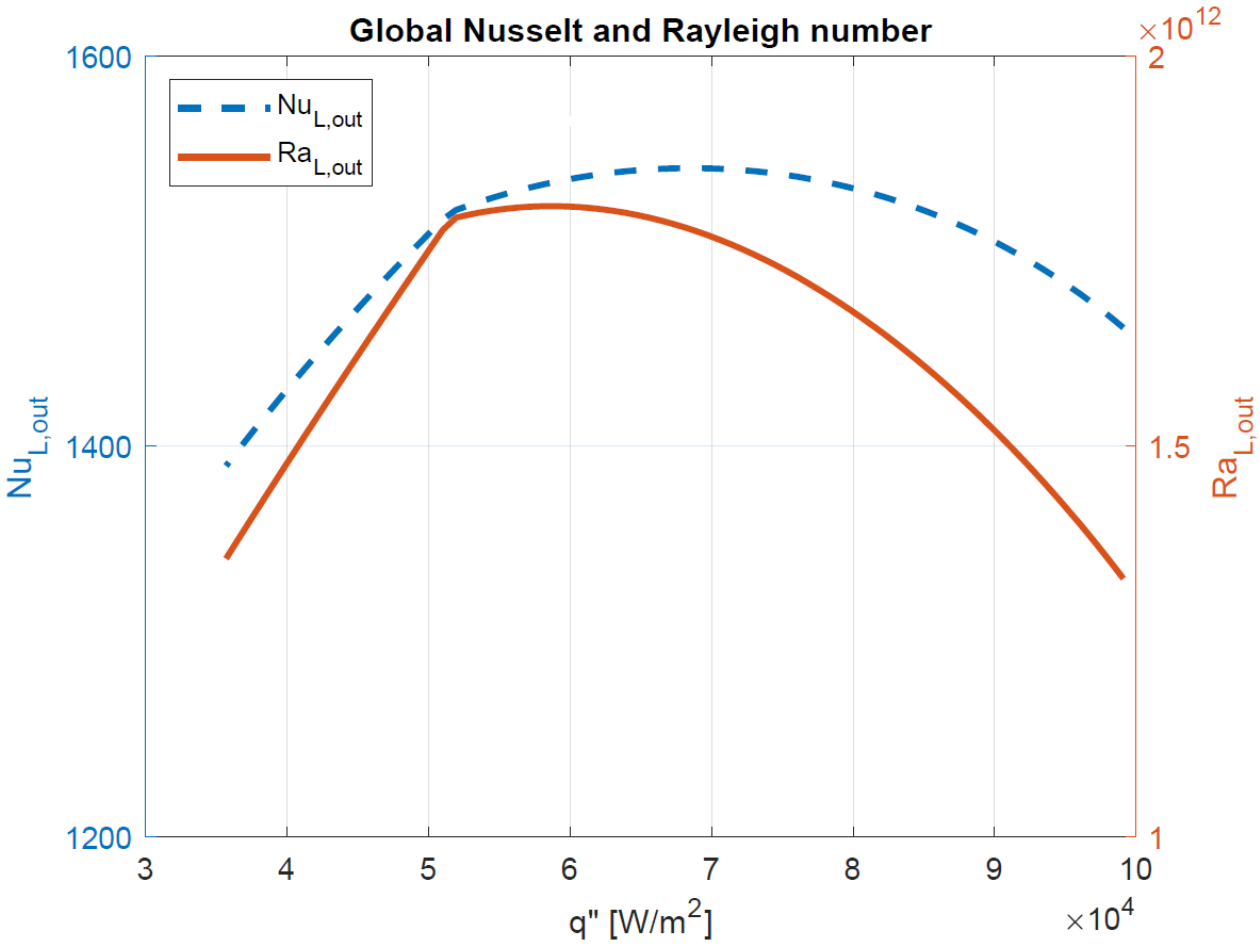

Fig. 3.13. Global Nusselt and global Rayleigh number as functions of the exchanged heat flux

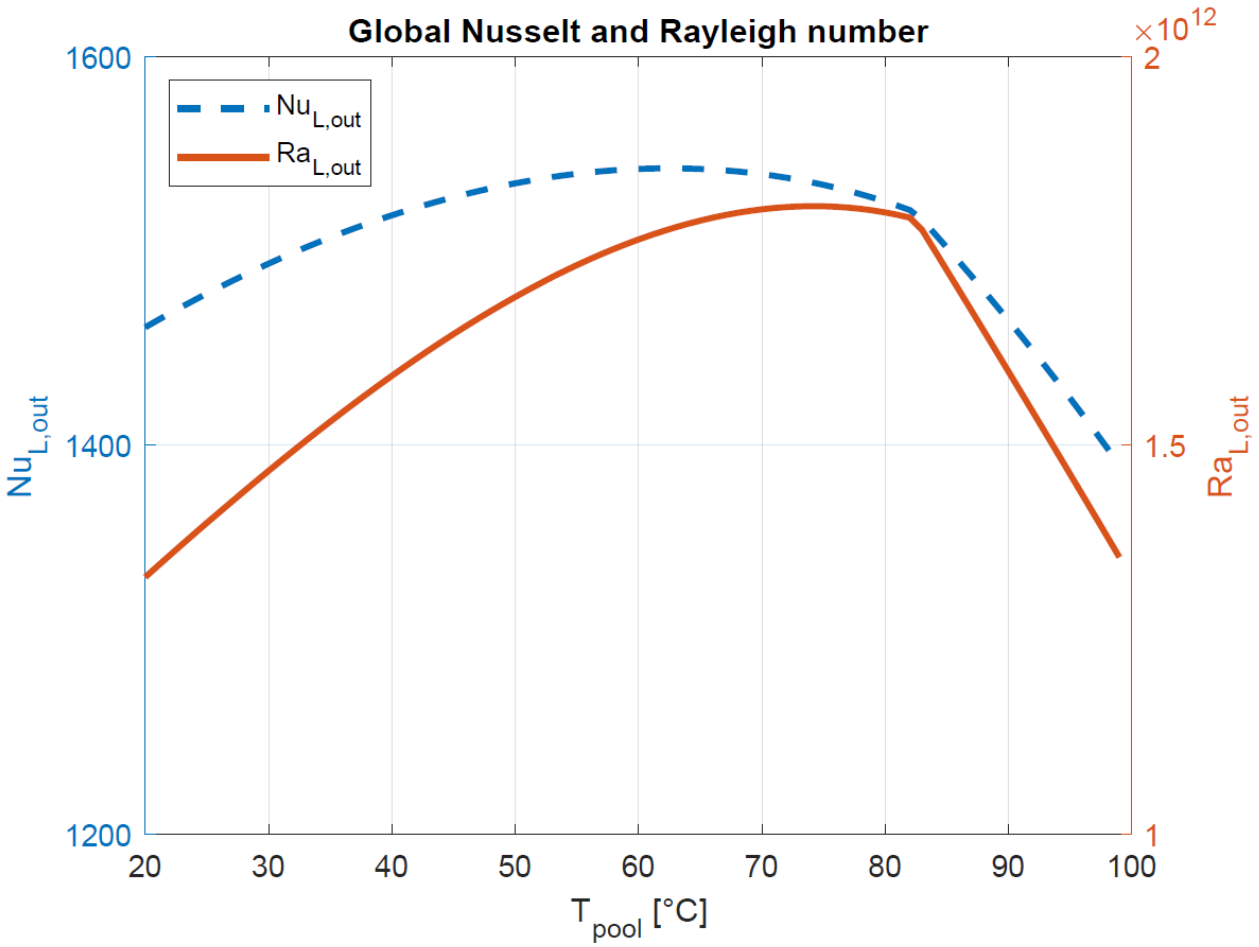

Fig. 3.14. Global Nusselt and global Rayleigh number as functions of the pool temperature

3.4.3 *Heat transfer coefficient*

Heat transfer coefficient is obtained in two different way, depending on the pool temperature: if pool temperature is lower than T_{sat} eq. 3.15 is used, otherwise the pool is in saturated conditions and Cooper correlation (eq. 3.8) is adopted. As regards the natural convection heat transfer coefficient, it shows a similar behavior to the global Nusselt number, and it varies from 1351.3 W/m^2/K (at T_{pool}=20 °C) to 1339.8 W/m^2/K (at T_{pool}=99 °C), showing a relative maximum equal to 1481.4 W/m^2/K (at T_{pool}=70 °C), while h_{out} during the nucleate saturated boiling is equal to 7039.7 W/m^2/K, which is almost five times the maximum value reached during the natural convection regime. The heat transfer coefficient as a function of the heat flux and pool temperature are shown in Fig. 3.15 and Fig. 3.16. Concerning the values of h_{out} as a function of the heat flux, pool temperature is fixed (each point corresponds to a different value of T_{pool}).

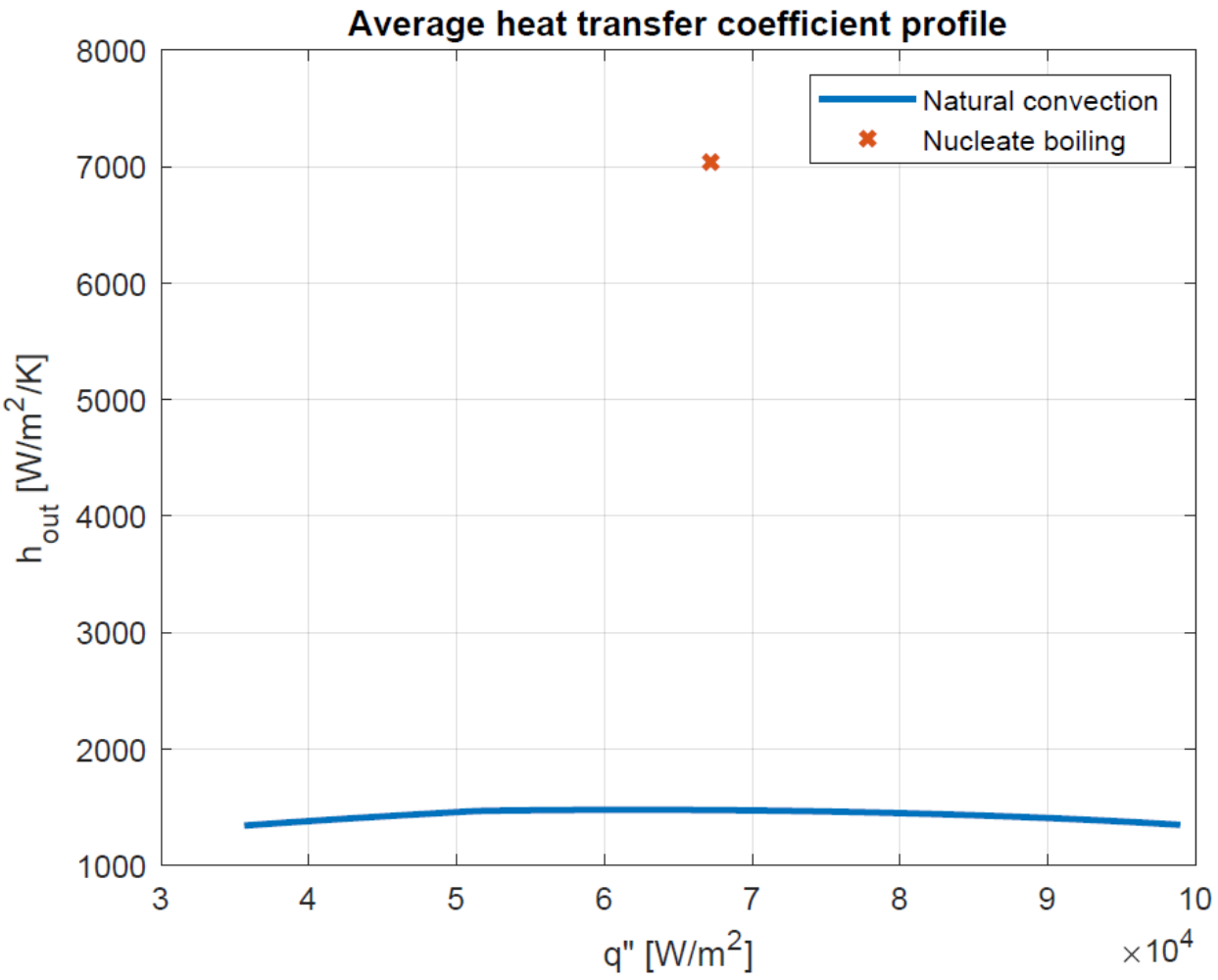

Fig. 3.15. Average heat transfer coefficient at different average heat fluxes.

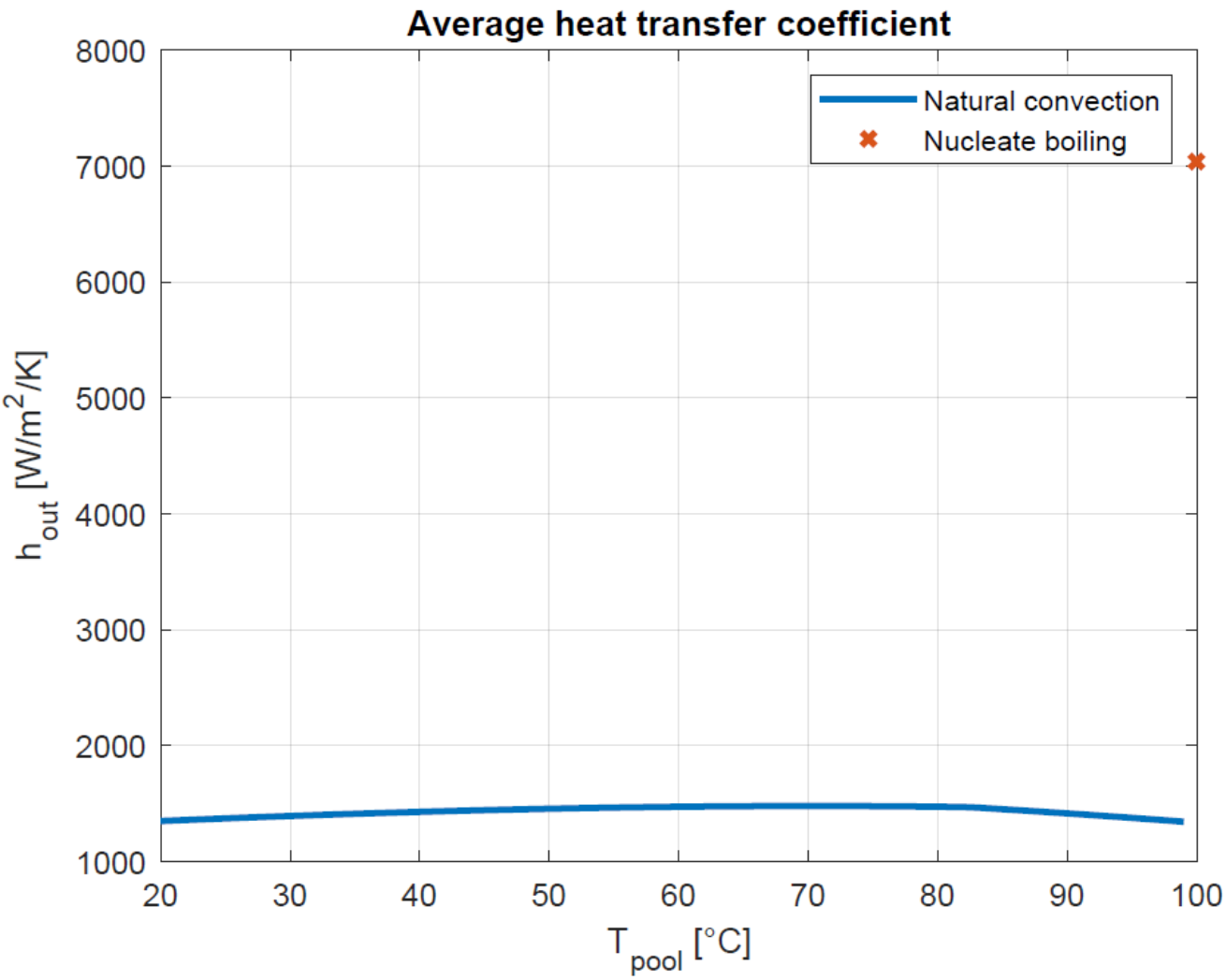

Fig. 3.16. Average heat fluxes at different pool temperatures

3.4.4 *Natural convection heat transfer validation*

In order to validate the results obtained by using natural convection correlations (eq. 3.6 and eq. 3.7 to evaluate *Nu* and then 3.15), a parametrical study is performed. Considering the same range of average heat flux (from $3.563*10^4$ to $9.898*10^4$ W/m^2) and the same range of pool temperature (from 20 to 99 °C), the heat transfer coefficient is evaluated by the definition shown in eq. 3.28:

$$h_{out,def} = \frac{q''}{(T_{w,out} - T_{pool})} \qquad (eq.\,3.28)$$

The average heat flux and pool temperature are independently imposed, and for each pool temperature, a different curve of heat transfer coefficient is obtained. Then, the heat transfer coefficient is evaluated using eq. 3.6, 3.7 and 3.15 previously discussed, in order to have a heat

transfer coefficient map. Then the two differently calculated heat transfer coefficients (using eq. 3.28 and eq. 3.15) are represented in Fig. 3.17.

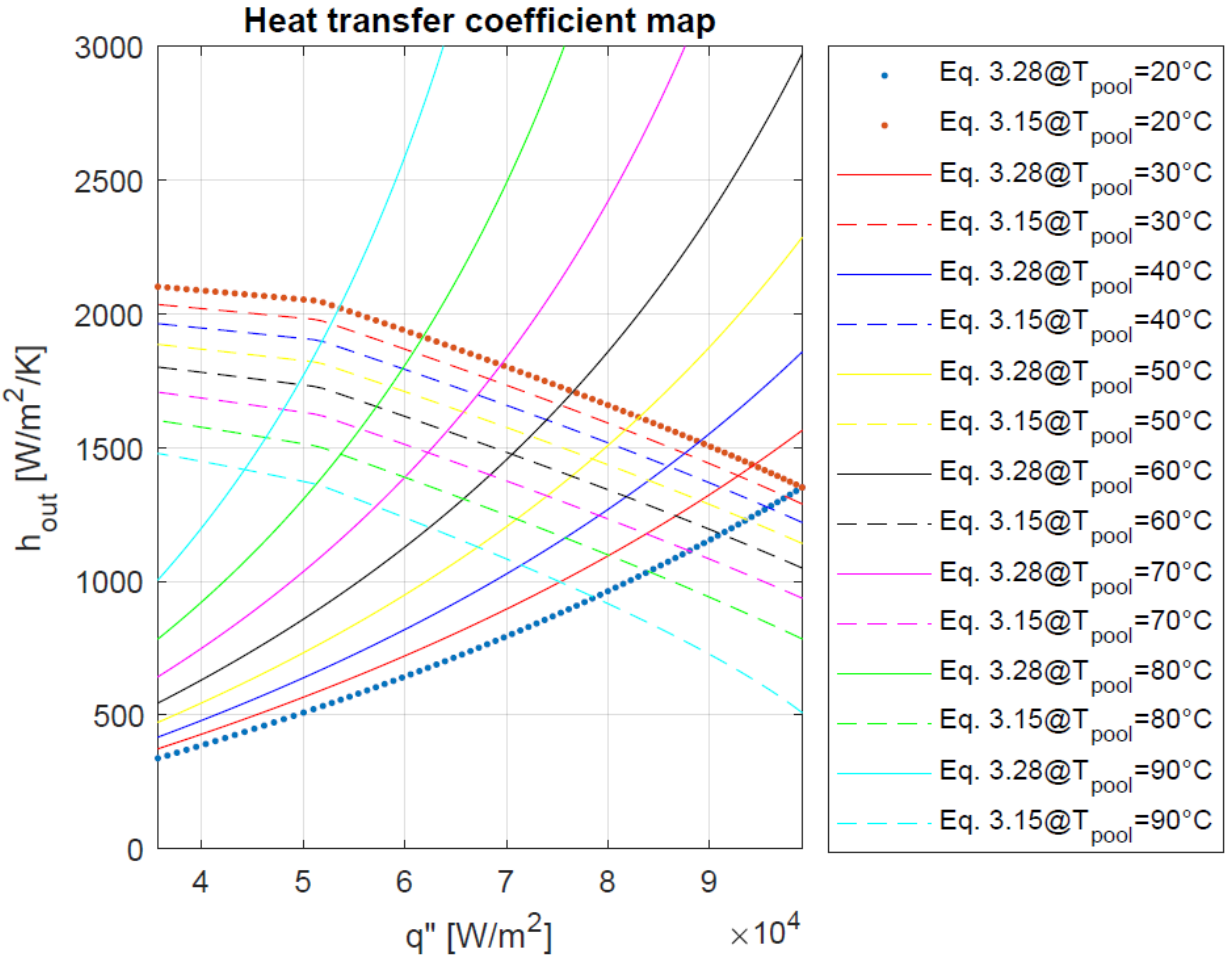

Fig. 3.17. Heat transfer coefficient map

From the heat transfer coefficient map in Fig. 3.17, the intersection between the h_{out} evaluated using the definition in eq. 3.28 (continuous and blue dotted lines) and the one obtained by using the Nusselt number (evaluated through correlations) eq. 3.15 (dashed and red dotted lines), for a given pool temperature and a given value of average heat flux, should provide the correct value h_{out}. Results are shown in Fig. 3.18 and Fig. 3.19.

Dots on the figures are the points of intersection between eq. 3.15 and 3.28 showed in the heat transfer coefficient map (Fig. 3.17). The continuous line in Fig 3.15 and Fig. 3.16 is the heat transfer coefficient computed by the script for the natural convection regime (eq. 3.15)

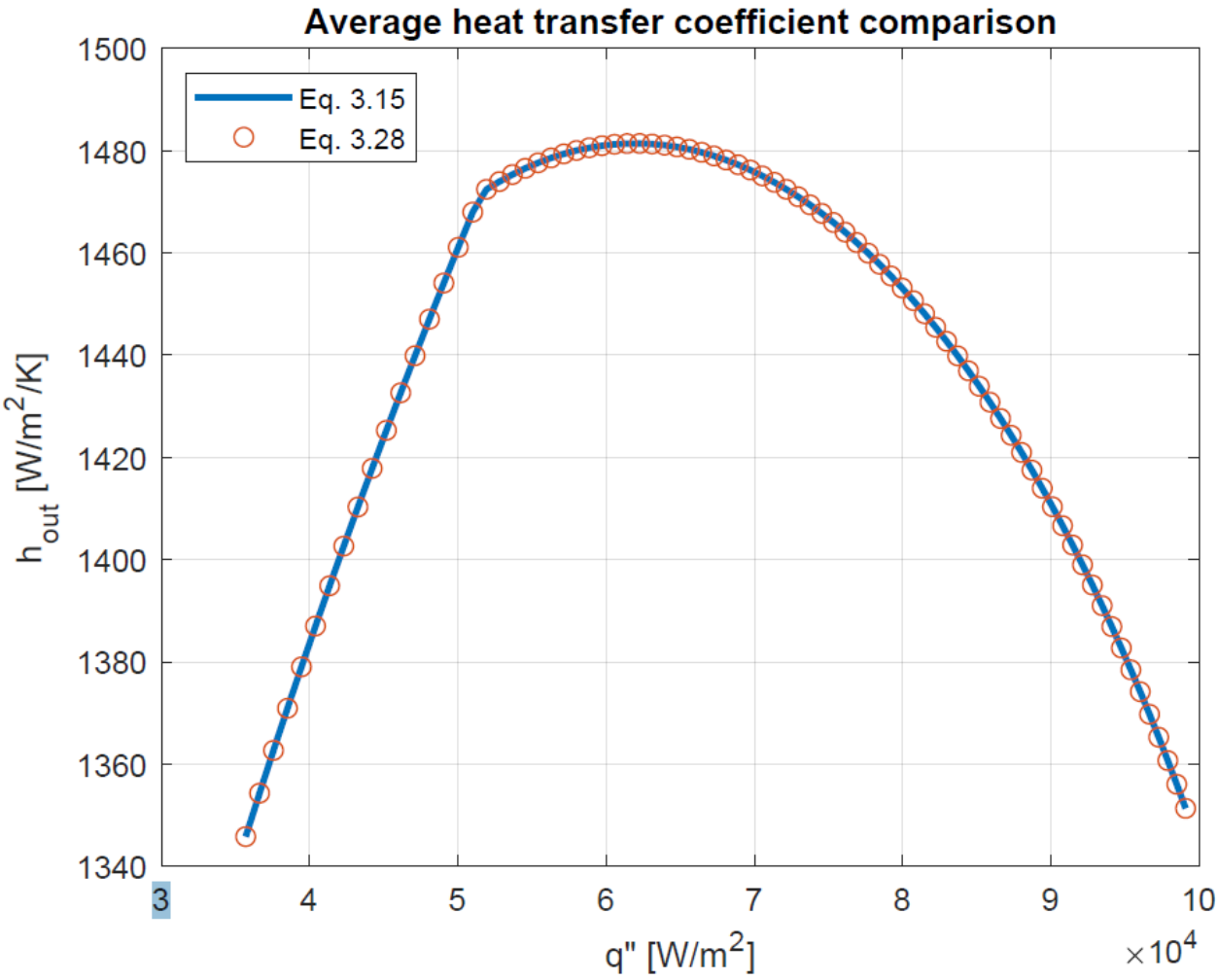

Fig. 3.18. Heat transfer coefficient comparison between the values obtained by the correlation (3.15) and the ones obtained by the heat transfer coefficient definition (3.28) as functions of the average heat flux

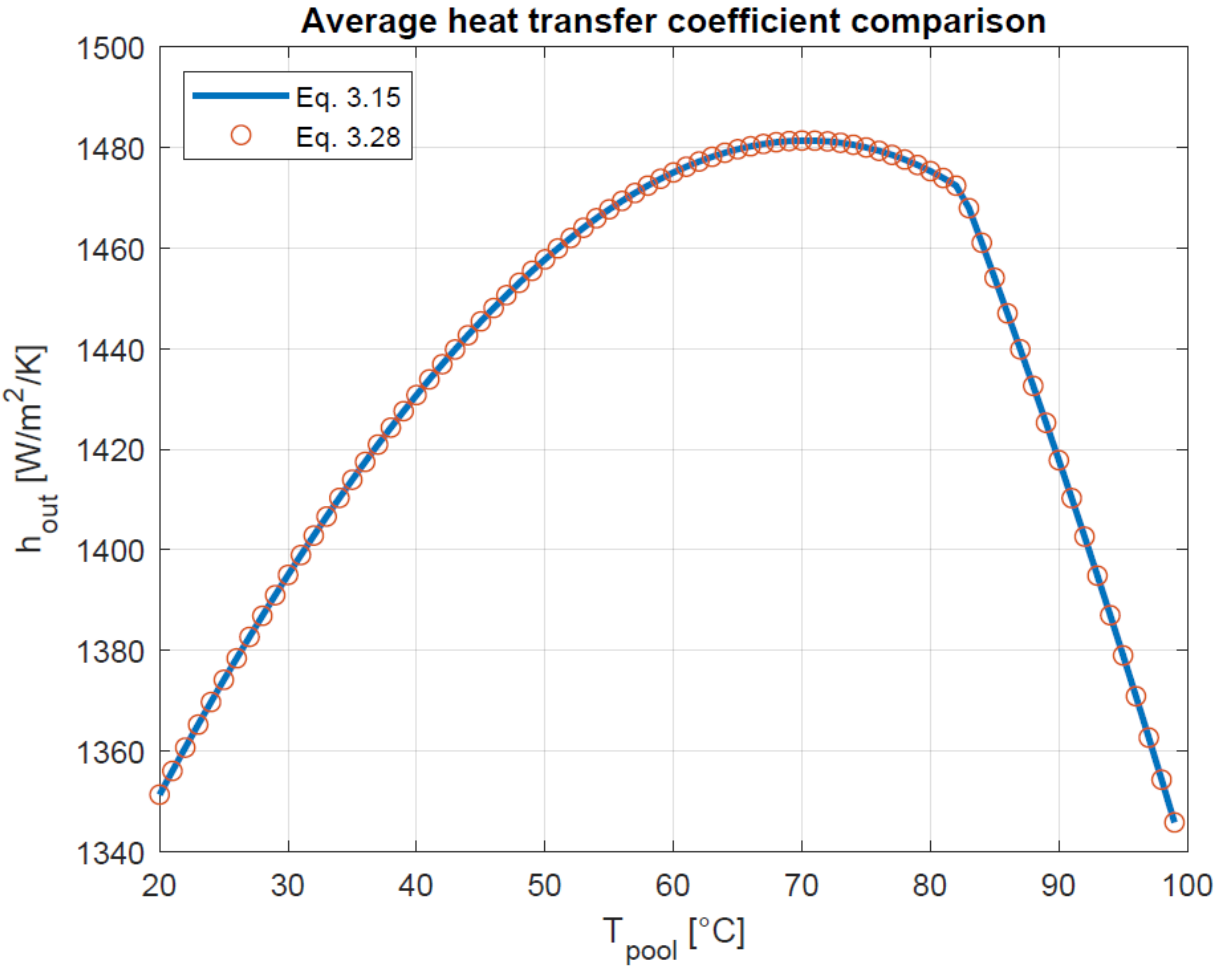

Fig. 3.19. Heat transfer coefficient comparison between the values obtained by the correlations (eq.3.15) and the ones obtained by the heat transfer coefficient (3.28) definition as functions of the pool temperature

3.4.5 *Average power and average heat flux*

From the analysis, the average heat flux and the average power decrease for increasing values of the pool temperature because of the reduction of the difference of temperature between the pool and the outer wall surface during the natural convection regime. Average thermal power exchanged through the test tube is computed using eq. 3.17 (inner wall temperature fixed, pool temperature imposed). It varies from $Q\,(T_{pool}=20°C)=7.28\ x10^3$ W to $Q\,(T_{pool}=99°C)=2.57x10^3$ W. The average heat flux (eq. 3.18) varies from $q''(T_{pool}=20°C)= 9.91x10^4$ W/m^2 to $q''(T_{pool}=99°C)=3.50x10^4$ W/m^2. On the other hand, during the nucleate boiling regime, heat flux and power increases, even though the outer difference of temperature between the pool and the outer wall surface becomes lower because of the higher efficiency of the two-phase heat transfer mechanisms. During saturated

nucleate boiling $Q\,(T_{sat})$=4.94 x10^3 W and $q''(T_{sat})$= 6.72x10^4 W/m^2 Results are shown in Fig. 3.20 and Fig. 3.21.

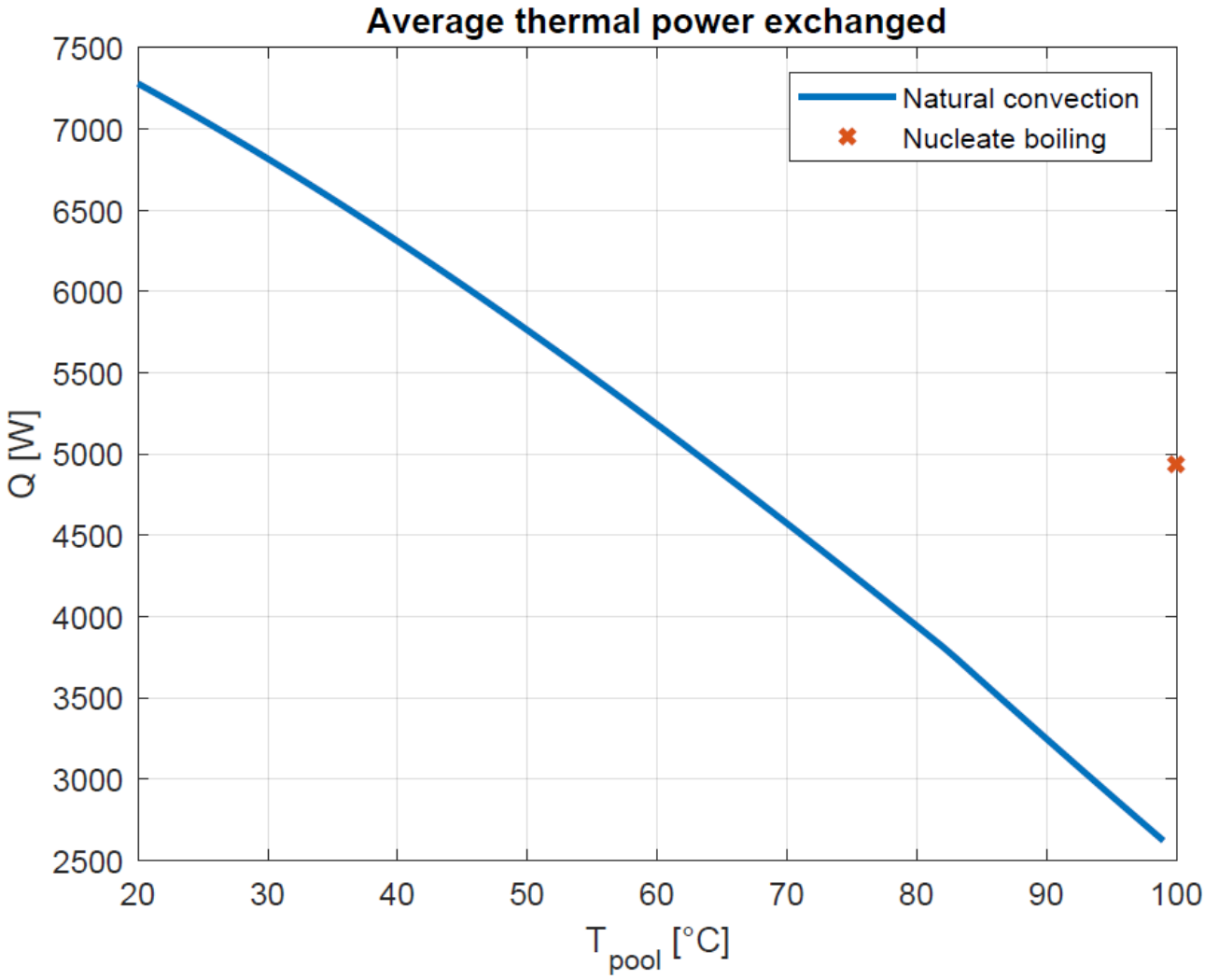

Fig. 3.20. Average thermal power as a function of pool temperature

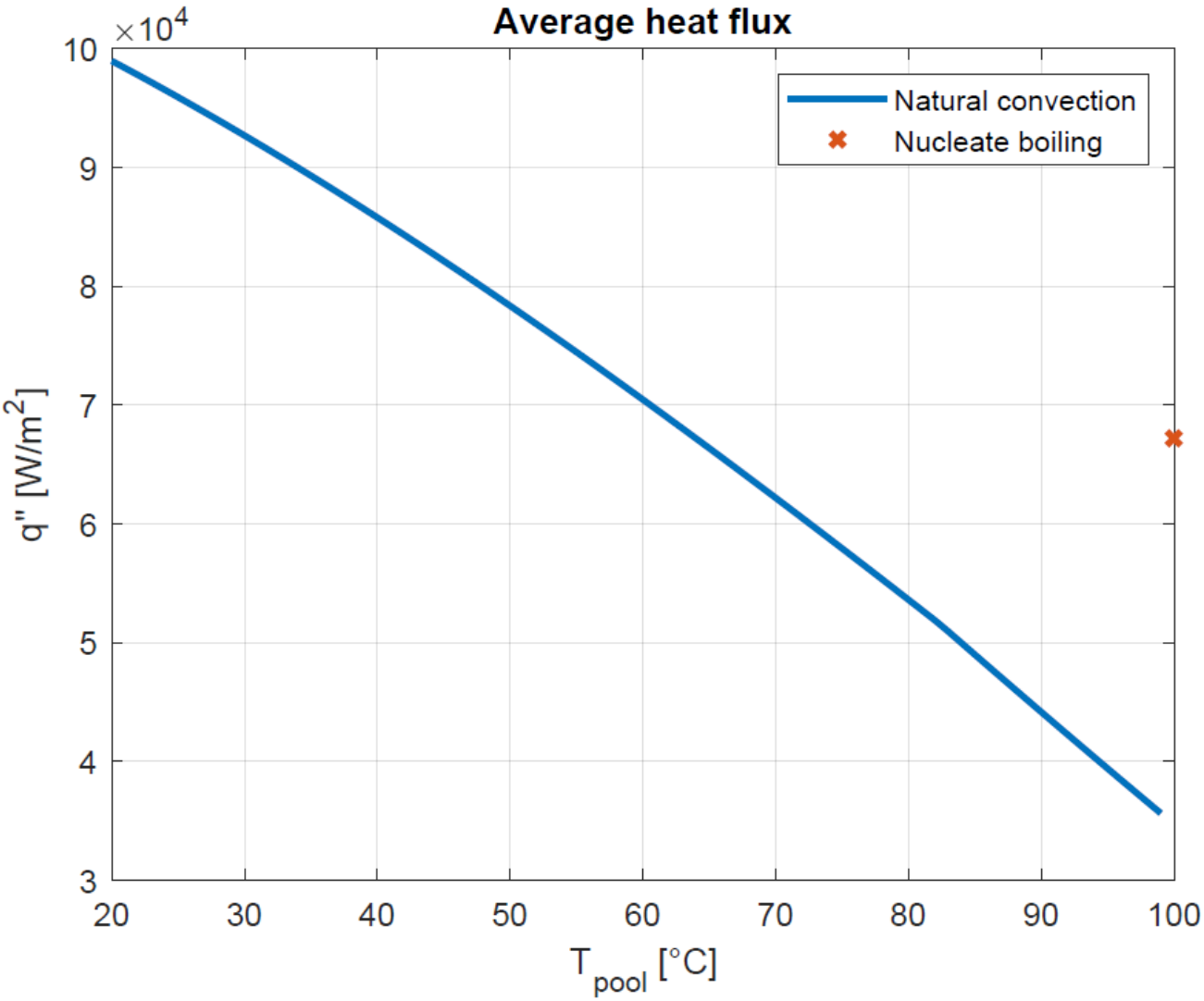

Fig. 3.21. Average heat flux as a function of pool temperature

3.4.6 *Vapor quality*

Heat flux is not directly measurable during the experimental procedure. For this reason it can be obtained implicitly measuring the condensing mass-flowrate at the outlet section of the heat transfer tube and assuming dry saturated steam at the inlet. Fig. 3.22 shows the average heat flux (eq. 3.17) as a function of the quality (eq. 3.21). It goes from 0.727 when the heat flux exchanged is equal to its maximum value $q''(T_{pool}=20°C)= 9.91\text{x}10^4$ W/m^2 and when pool temperature is equal to 99 °C (corresponding to the average heat flux's smallest value) the corresponding value of quality is equal to 0.904. During the saturated boiling regime void fraction is equal to 0.815.

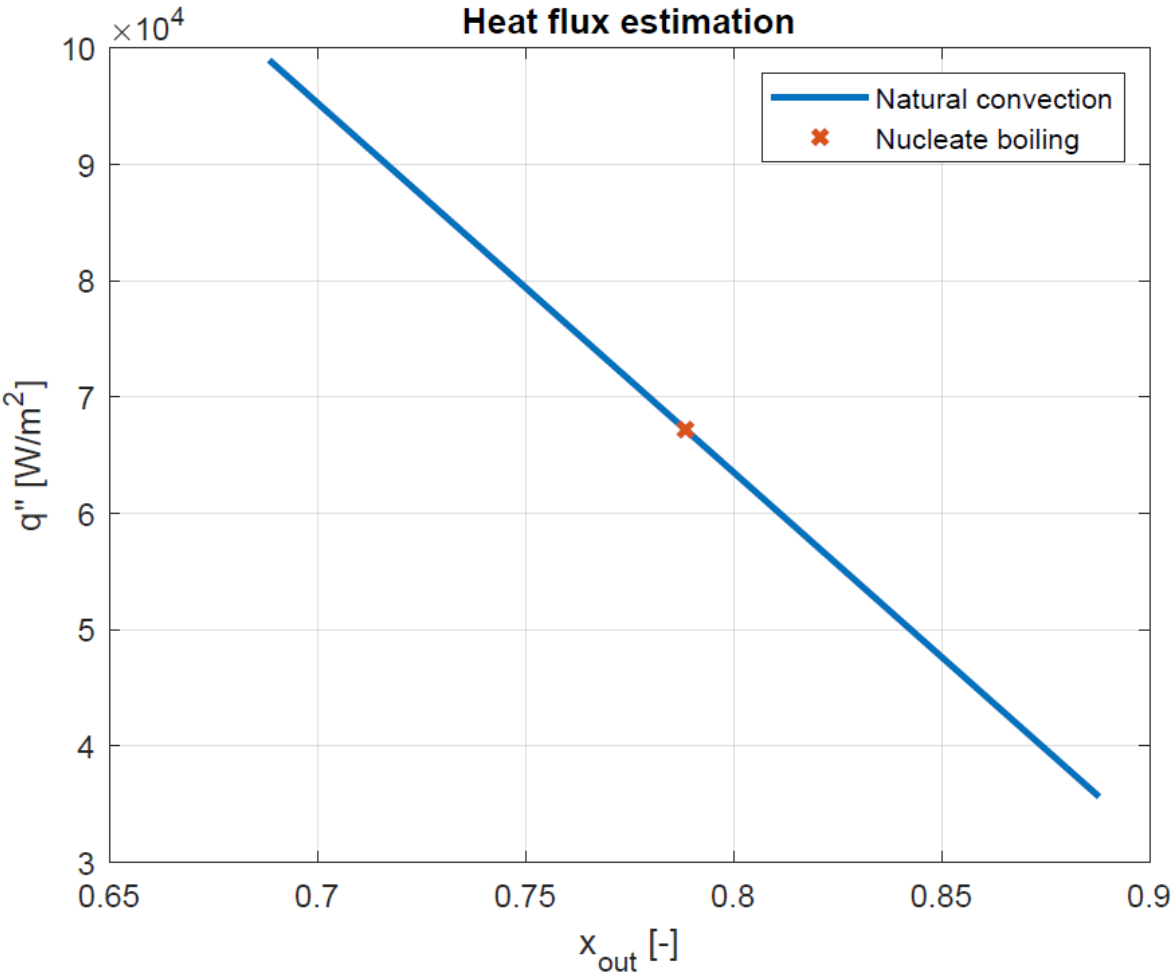

Fig. 3.22. Estimation of the heat flux looking at the outlet title

3.4.7 *Saturation time*

The time required by the pool to reach the saturation condition is evaluated considering the two different configurations of the system: imposed temperature and imposed heat flux. In the first case, as shown in section 3.4.5, average heat power exchanged by the tube depends on the imposed value of pool temperature (Fig. 3.22). In the second case heat power is constant, and equal to 3300 W. Fig. 3.23 shows the time evolution of power exchanged in the imposed temperature configuration. Q decreases with time because as the time passes, pool temperature becomes higher, reducing the temperature drop between the inner wall and the pool temperature.

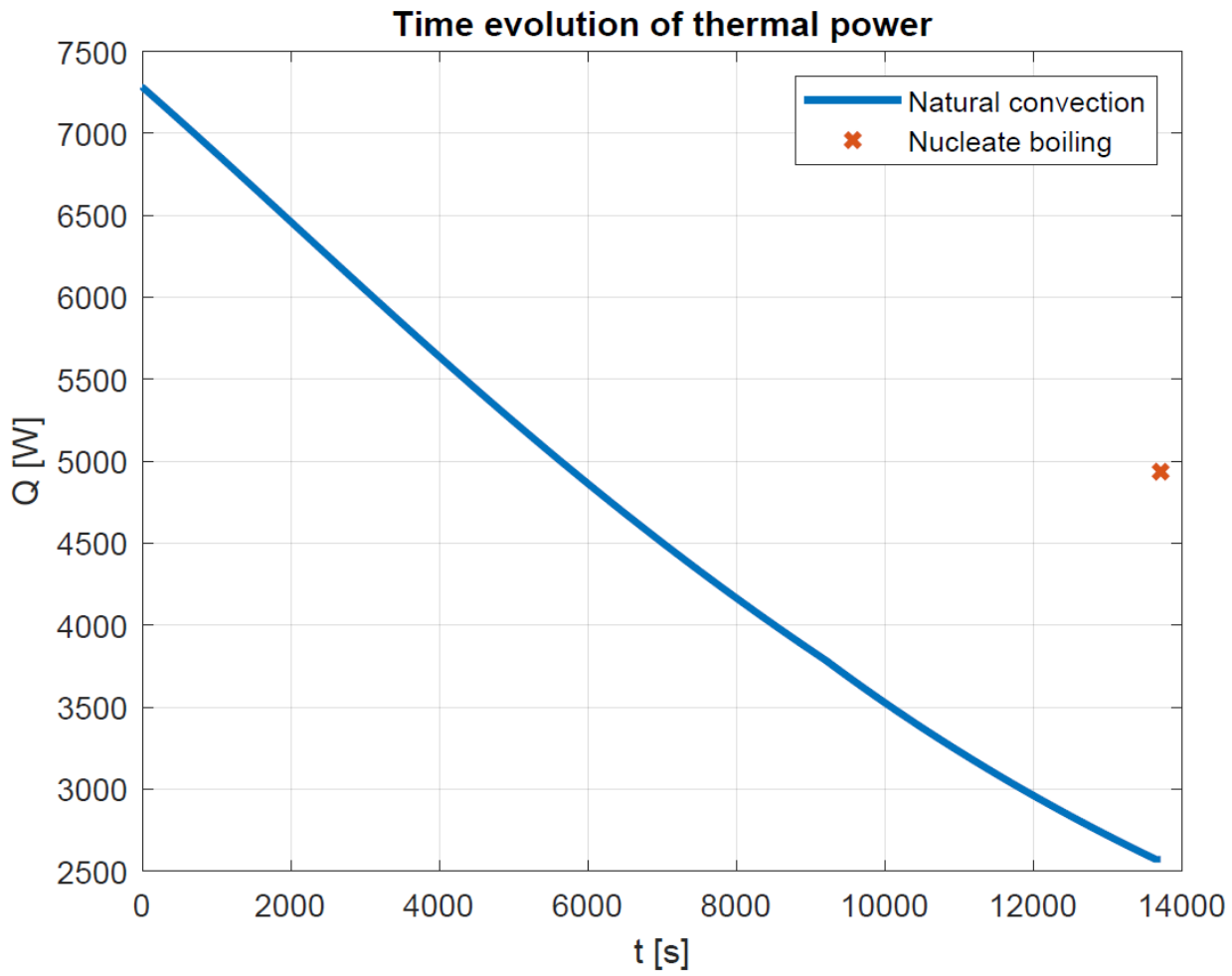

Fig. 3.23. Power evolution respect to time. Imposed temperature configuration.

The evolution of pool temperature is computed using eq. 3.25 and different results are obtained according to the considered system's configuration. Fig. 3.24 shows the time evolution of pool temperature considering an imposed temperature configuration. $T_{pool}(t)$ increases with time, but in a non linear way because of the decreasing evolution of thermal power released as the system evolves. In this case, saturation conditions are supposed to be reached after 13688 (almost 3h and 48m). As regards the imposed temperature configuration, the evolution of pool temperature is shown in Fig. 3.25. Obviously also in this case $T_{pool}(t)$ increases with time, but it shows a linear evolution because of the constant value of power released by the electrically heated rod. In this case the time required to reach saturation conditions is much higher and it is equal to 19444 s (almost 5h and 24m). The difference of time for the two configuration is equal to is equal to 5756 s (about 1h and 36m).

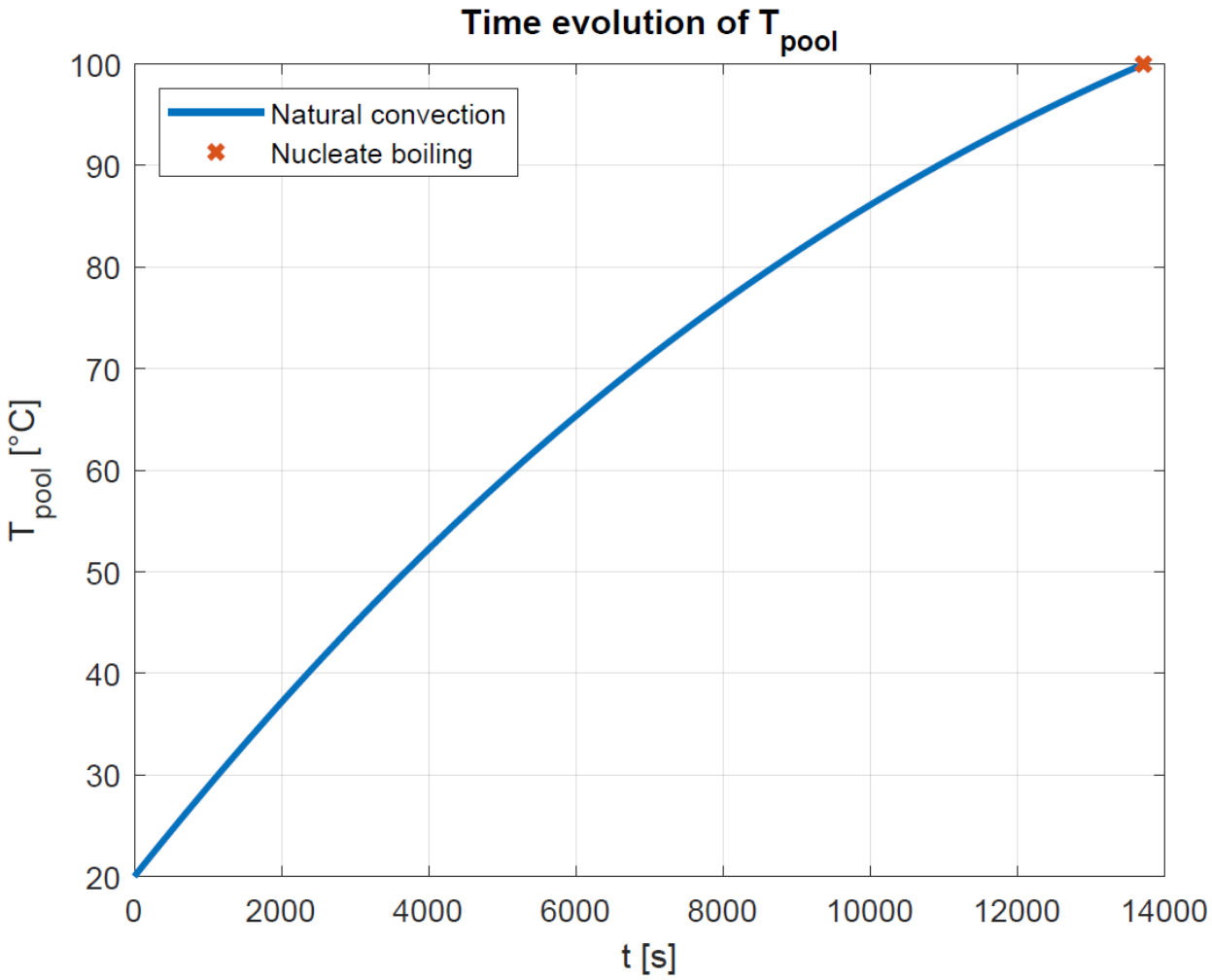

Fig. 3.24. Temperature evolution respect to time. Imposed temperature configuration.

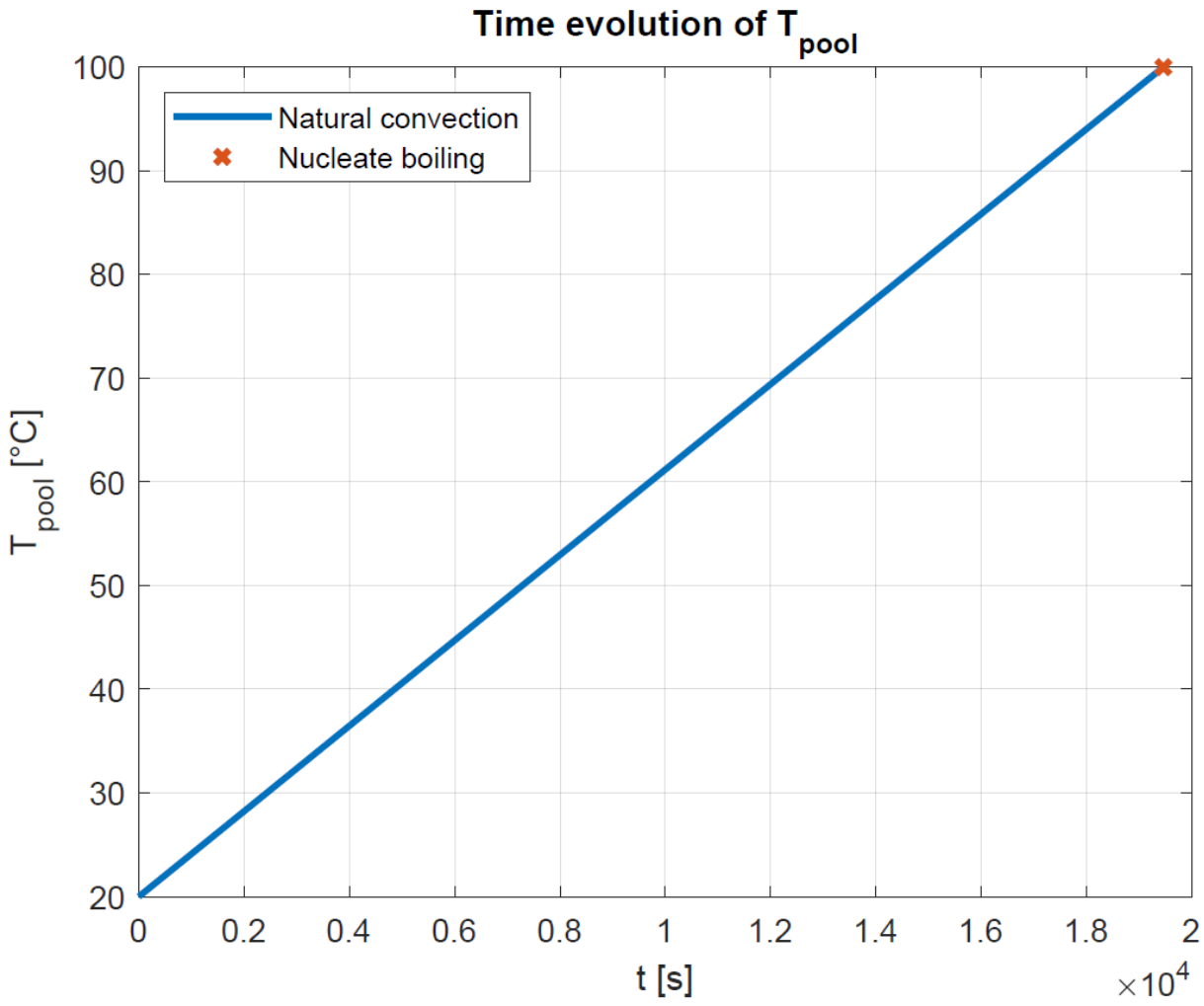

Fig. 3.25. Temperature evolution respect to time. Imposed heat flux configuration.

As a result of the above-mentioned researches, we can summarize the main phenomena that is studied, their results and the analysis performed by numerical simulations and experimental tests.

The main components of these kind of systems are: a pool, which represents the heat sink, and an heat exchanger, which is the heat source. The heat removal process occurs through a complex interaction of mass and heat transfer, which involves single and two-phase flow. The thermal energy removed from the source is redistributed inside the pool thanks to the fluid motion, driven by density gradients. The resulting transient produces, on the secondary side, a non-uniform temperature distribution until the suppression of thermal stratification, which happens when the pool temperature reaches everywhere the saturation value, inducing strong mixing phenomena. Even if the temperature is homogeneous, the transient goes on because of the evaporation of the liquid inside the pool.

For all the mentioned systems, pools show two dominant effects: thermal stratification and perfect radial mixing.

- Thermal stratification

Thermal stratification is reached because of the vertical thermal gradients. They are established by the upward movement of hotter fluid, meanwhile the colder and heavier one becomes stagnant in the bottom region. As the fluid temperature approaches to the saturation value, the lower region of the pool starts to take part in the mixing process. This is achieved thanks to the propagation of the "thermal interface", when the heat can only be transferred from the upper region by thermal conductivity, rather than through convection. As this "thermal interface" reaches the bottom of the pool, thermal stratification is suppressed.

- Perfect radial mixing

Even though vertical thermal gradients can be detected, things are different in the radial direction. Actually a perfect radial mixing is observed because hot water, reaching the pool surface at the atmospheric pressure, moves radially toward the boundary walls. Here, a weak recirculation process occurs, slightly improving thermal mixing. For this kind of phenomenon, dimensions of the systems can be relevant. As a matter of fact, the recirculation near the wall is a boundary effect, which means that in large pools the magnitude of the resulting recirculation has a different impact than the one observed for a scaled system or a small experimental tank.

In some particular cases, the suppression of thermal stratification for a rather long time can be achieved for large systems such as GDWPs. Most of the researches focused on these kind of systems were performed by numerical simulations, since experimental studies are quite difficult to be carried out, considering the large mass inventory of these pools (8000 m^3). According to the

CFD analysis and numerical simulations performed by Verma, et al., (2013) and by Kumar, et al., (2017b), the suppression of thermal stratification can be reached thanks to the introduction of "shrouds". Different configurations were simulated, taking into account the effect of many parameters on the performance (i.e. number of shrouds, height of shrouds, flow area, materials, connections between channels). The obtained results show the capability of these devices into highly extend in time the cooling of steam inside the ICs (up to almost 10 days).

Antal, S., Lahey Jr, R., & Flaherty, J. (1991). Analysis of phase distribution in fully developed laminar bubbly two-phase flow. *International Journal of Multiphase Flow*, 635-652.

Berenson, P. (1961). Film-boiling heat transfer from a horizontal surface. *Journal of Heat Transfer*, 351-356.

Bergles, A., & Rohsenow, W. (1694). The determination of foced-convection surface-boiling heat transfer. *Journal of Heat Transfer*, 365-372.

Bird, R., Stewart, W., & Lightfoot, E. (1960). *Transport Phenomena* (2 ed.). New York: Wiley Interscience.

Brackbill, J., Kothe, D., & Zemach, C. (1992). A continuum mehod for modeling surface tension. *Journal of Computational Physics*, 335-354.

Bromley, L. (1950). Heat transfer in stable film boiling. *Chemical Engineering Progress*, 221-227.

Churchill, S., & Chu, H. (1975). Correlating equation for laminar and turbolent free convection from horizontal cylinder. *International Journal of Heat and Mass Transfer*, 1049-1053.

Churchill, S., & Chu, H. (1975). Correlating equations for laminar and turbolent free convection from a vertical plate. *International Journal of Heat and Mass Transfer*, 1323-1329.

Collier, J. G., & Thome, J. R. (1994). *Convective Boilind and Condensation* (III ed.). Oxford: Claredon Press.

Corletti, M., Hochreiter, L., & Squarer, D. (1989). AP600 passive residual heat removal heat exchanger test. *Tractation of the American Nuclear Society*, 669-671.

Drew, T., & Mueller, A. (1937). Boiling. *Trans. AlChE*, 449.

Ganguli, A., Sathe, M., Pandit, A., Joshi, J., & Vijayan, P. (2010). Hydrodynamics and heat transfer characteristics of passive decay heat removal systems: CFD simulation and experimental measurements. *Chemical Engineering Science, 65*, 3457-3473.

Ge, J., Tian, W., Qiu, S., & Su, G. (2018). CFD simulation of secondary side fluid flow and heat transfer of the passive residulal heat removal heat exchanger. *Nuclear Engineering and Design*, 27-37.

Han, Y., Wang, R., & Dai, Y. (2009). Thermal tratification within the water tank. *Renewable and Sustainable Energy Reviews*, 1014-1026.

Hewitt, G. (1964). A method of representing burnout data in two-phase heat tranfer for uniformly heated round tubes. *Atomic Energy Research Establishment*, 11-15.

Hewitt, G., Kaersey, H., Lacey, P., & Pulling, D. (1965). Burnout and nucleation in climbing film flow. *International Journal of Heat and Mass Transfer, 8*(5), 793-814.

IAEA. (1991). *Safety related terms for advanced nuclear plants.* Vienna: IAEA.

IAEA. (2009). *Passive Safety Systems and Natural Circulation in Water Cooled Nuclear Power Plants.* IAEA.

Incropera, F., Dewitt, D., Bergman, T., & Lavine, A. (2011). *Heat and mass transfer* (7-th ed.). Jefferson City, Missouri, USA: Jhon Wiley & Sons.

Ishii, M., & Zuber, N. (1979). Drag coefficient and relative velocity in bubbly, droplet or particulate flows. *American Institute Chemical Engineers Journal*, 843-855.

Kandlikar, S. (1998). Heat transfer characteristics in partial boiling, fully developed boiling, and significant void flow regions of subcooled flow boiling. *Journal of Heat Transfer, 120*, 395-401.

Kang, M.-G. (1998). Experimental investigation of tube length effect on nucleate pool boiling heat transfer. *Annals of Nulcear Energy*, 295-304.

Khan, S., Tahir, F., Baloch, A., & Koç, M. (2019). Review of Micro–Nanoscale Surface Coatings Application for Sustaining Dropwise Condensation. *Coatings*, 117.

Knudsen, M. (1934). *The kinetic theory of gases, some modern aspects.* London: Methuen & Co.

Kumar (a), M., Nayak, A., Jain, V., Vijayan, P., & Vaze, K. (2013). Managing a prolonged station blackout condition in AHWR by passive means. *Nuclear Engineering and Tecnology*, 605-612.

Kumar (b), S., Vijayan, P., Kannan, U., Sharma, M., & Pilkhwal, D. (2017). Experimental and computational simulation of thermal stratification in large pool with immersed condenser. *Applied Thermal Engineering*, 345-361.

Kumar (c), S., Grover, R., Vijayan, P., & Kannan, U. (2017). Numerical investigation on the effect of shrouds around an immersed isolation condenser on the thermal stratification in large pools. *Annals of Nuclear Energy*, 109-125.

Kurul, L., & Podowski, M. (1991). Multidimensional effect in forced convection subcooled boiling. *Preceedings of the Ninth International Heat Transfer Conference, 2*, 21-26.

Kutateladze, S. S. (1963). *Foundamentals of Heat Transfer.* New York: Academic Press.

Labuntsov, D. (1957). Heat Transfer in Film Condensation of Pure Steam on Vertical Surfaces and Horizontal Tubes. *Teploenergetika*, 72.

Lahey, R., & Moody, F. (1996). *The Thermal-Hydraulics of a Boiling Water Nuclear Reactor* (2 ed.). La Grange Park, Illinois, USA: American Nuclear Society.

Lahey, R., Bertodano, M., & Jones Jr., O. (1993). Phase distribution in complex geometry conduits. *Nuclear Engineering and Desing*, 177-201.

Lienhard, J., & Eichhorn, R. (1976). Peak boiling heat flux on cylinders in a cross flow. *International Journal of Heat and Mass Transfer, 19*, 1135-1142.

Liu, Z.-H., & Qiu, Y.-H. (2002). Enhanced boiling heat transfer in restricted spaces of a compact bundle with enhanced tubes. *Applied Thermal Engineering*, 1931-1941.

Lu, D., Yuhao, Z., Fu, X., Wang, Z., Cao, Q., & Yang, Y. (2016). Experimental investigation on natural convection heat transfer characteristics of C-shape heating rods bundle used in PRHR HX. *Annals of Nuclear Energy*, 226-238.

Lucas, D., Shi, J., Krepper, E., & Prasser, H.-M. (2004). Models for the forces acting on bubbles in comparison with experimental data for vertical pipe flow. *3rd, International symposium on two-phase flow modelling and experimentation. 1*, pp. 103-110. Pisa: ETS.

Menter, F. (1994). Two-equation eddy-viscosity turbulence models for engineering applications. *American Institute of Aerospace and Aeronautical Journal, 32*(8), 1598–1605.

Mikic, B., & Rohsenow, W. (1969). A new correlation of pool-boiling data includind the fact of heating surface characteristics. *Journal of Heat Transfer*(91), 245-250.

Nukiyama, S. (1934). The maximum and minimum values of the heat Q transmitted from metal to boiling water under atmospheric pressure. *Journal Japan Soc. Mech. Eng.*, 367-374.

Oclon, P., Lopata, S., & Nowak, M. (2014). A novel 1D/2D model for simulating conjugate heat transfer applied to flow boiling in tubes with external fins. *Heat Mass Transfer* , 553-566.

Parlatan, Y., & Rohatgi, U. (1997). Simple model of boiling hat transfer on tubes in large pools. *Journal of Heat Transfer*, 379-379.

Petukhov, B. S. (2005). Heat transfer and friction in turbolent pipe flow with variable properties. *Advanced Heat Transfer, 48*, 4161-4173.

Rhosenow, W. (1956). Heat Transfer and Temperature Distribution in Laminar Film Condensation. *Heat Transfer Journal*, 1645-1648.

Rohsenow, W. (1951). *A method of correlating heat transfer data for surface boiling of liquids.* Cambridge, Massachusetts, USA: MIT Division of Industrial Cooperation.

Sadasivan, P., & Lienhard, J. (1987). Sensible heat correction in laminar film boiling and condensation. *Journal of Heat Transfer* , 543-547.

Sato, Y., Sadatomi, M., & Sekoguchi, K. (1981). Momentum and heat transfer in two-phase bubble flow—I. Theory. *International Journal of Multiphase Flow*, 167-177.

Schrage, R. W. (1953). *A theoretical study of interphase mass transfer.* New York: Columbia University Press.

Tao, J., Gu, H., Xiong, Z., Jiang, X., & Xie, Y. (2018). Parametric analysis of heat transfer rate if passive residual heat removal heat exchanger submerged in water tank. *Experimental Thermal and Fluid Science*, 317-327.

Thompson, J. (2013). *Direct measurement of boiling water heat flux for predicting and controlling near critical heat flux.* Master thesis, Virginia Polytechnic Institute and State University, Mechanical Engineering, Blacksburg.

Tian, Y., Chen, Z., Wang, N., Cui, Z., & Cheng, L. (2018). Experimental investigations on pool boiling on a vertical tube in the confined and unconfined space. *Applied Thermal Engineering*, 107-116.

Tian, Y., Zhang, K., Wang, N., Cui, Z., & Cheng, L. (2017). Numerical study of pool boiling heat transfer in a large-scale confined space. *Applied Thermal Engineering*, 188-198.

Tong, L., & Hewitt, G. (1972). Overall viewpoint of flow boiling CHF mechanisms. *ASME Paper 72-HT-54*.

van Stralen, S., & Cole, R. (1979). *Boiling phenomena.* New York: McGraw-Hill.

Van Stralen, S., Cole, R., Sluyter, W., & Sohal, M. (1975). Bubble growth rates in nucleate boiling of water at subatmosfpheric pressures. *International Journal of Heat and Mass Transfer*(18), 665-669.

Verma, P., Nayak, A., Vikas, J., & Vase, K. (2013). Suppression of thermal stratification in gravity driven water pool. *Annals of Nuclear Energy*, 221-227.

Westinghouse. (2012). *Westinghouse AP1000 Design Control Document.*

Whalley, P. (1987). *Boiling, Condensation and Gas-Liquid Flow.* Oxford: Clarendon Press.

Zeng, L., Klauser, J., & Mei, R. (1993). A unified model for the prediction of bubble detachment diameters in boiling systems - I. Pool boiling. (Elsevier, Ed.) *International Journal of Heat and Mass Transfer*, 2261-2270.

Zuber, N. (1958). On the stability of boiling heat transfer. *Transactions of the American Society of Mechanical Engineers*, 711-720.